FERMILAB-THESIS-2020-20

Search for New Bosons in Gluon-Gluon and Vector Boson Fusion Processes at the LHC and Development of Silicon Module Assembly Techniques for the CMS High Granularity Calorimeter

by

Kamal Lamichhane, B.S., M.S.

A Dissertation

In

Physics

Submitted to the Graduate Faculty
of Texas Tech University in
Partial Fulfillment of
the Requirements for
the Degree of

DOCTOR OF PHILOSOPHY

Approved

Dr. Shuichi Kunori
Chair of Committee

Dr. Andrew James Whitbeck
Co-Chair of Committee

Dr. Nural Akchurin

Dr. Sung-Won Lee

Dr. Akif Ibragimov

Dr. Mark A. Sheridan
Dean of the Graduate School

December, 2020

Acknowledgements

First of all, I would like to express my sincere gratitude to my supervisor Dr. Shuichi Kunori. I feel blessed for the opportunity to work with Dr. Kunori, a person with great idealism, knowledge, inspiration, clear-thinking, and calming influence. A big thank you for all your trust, support, and guidance which have been very encouraging to me. It was truly an honor to be a student of such a first-rate individual.

I would like to express my kudos to Dr. Andrew Whitbeck for helping me in many different aspects to get my analysis completed in a way that I become an expert of the various skills and tools. It has been a great learning experience with you and I do not think that I can ever thank you enough. I am very grateful to Dr. Nural Akchurin for his teaching, guidance, support, and encouragement. I am blessed to be your student. I am also thankful to Dr. Sung-won lee for his guidance and advice on many different occasions in regard to various subjects. A big thank you to Dr. Akif Ibraguimov for honoring me as a committee member. I am blessed to have all of you as a committee member of this dissertation.

I would also like to thank Drs. Vinay Hegde and Jordan Damgov, the entire HEP group at TTU, and Yalcin Guler from Cukurova University for their continuous help and support. I also like to thank the entire physics department at TTU and also my undergraduate students whom I had the honor to teach and help during my time as a TA. I can never thank enough to Dr. Mahdi Sanati whose teachings, guidance, and support were crucial for me to survive in the graduate program and eventually passing the Ph.D. prelim exam. Thank you Debra, Joyce, and Melanie for helping me with all the administrative stuff throughout my graduate school time. Also thank you Kim, Phil, and Chris for all your support and help. A big thanks to Drs. Joel Walker (SHSU) and David Toback (TAMU); without you, I don't think I would be in the field of particle physics. Thank you for all the support you have been providing.

I would also like to acknowledge our colleagues from the CMS experiment who has helped in many different ways i.e., operations related to collect the data, analysis group in analyzing the data, conveners for reviewing my work again, and again. I

would like to mention Dr. Frank Chlebana from Fermilab for his continued guidance and support. I would also like to mention Drs. James Hirschauer, Zoltan Gecse, Harry Cheung, and Maral Alyari, and many colleagues at the LPC Fermilab for supporting me.

Finally, a big thank you to my family for helping me to be who I am with all your love and care. A special mention to my mother, thank you for bringing me to this world and all the struggles and pains that you have gone through to help me reach this level. Many thanks to my wife Usha for everything. Although my work could not claim a discovery of new physics currently; however, I and my wife Usha have discovered the new line of enthusiasm for the rest of our life i.e. [redacted]. You have arrived in a difficult time i.e., right after the pandemic of COVID-19 started and God has chosen your mom to provide care to the needy with her nursing skills. This has been a very tough situation for us and at the same time, I have to finish my thesis. I am thankful to your grandparents to provide you and us the support that we desperately needed. Perhaps the drops rolling from my eyes and heart while typing these lines poses more words than I can write.

Table of Contents

Abstract

A search for heavy resonances decaying to a pair of vectors bosons is presented which utilizes events in which a hadronically decaying Z or W boson is identified using jet substructure techniques and large missing transverse momentum is found. Data analyzed were recorded by the Compact Muon Solenoid experiment at the CERN Large Hadron Collider in 2016, 2017, and 2018, and correspond to 137 fb^{-1}. The events are categorized as having arisen from Vector Boson Fusion process or not, and are characterized by their transverse mass distribution. The standard model backgrounds are estimated based on observed yields in control regions. No excess of events above the expected SM background are observed and limits are placed on the production cross section of Radion (spin-0), Wprime (spin-1) and Bulk graviton (spin-2) particles. In adiditon, the high luminosity LHC and the CMS HGCAL upgrade are also presented. The assembly techniques and various tests for the Silicon module and the cassette are discussed.

List of Tables

List of Figures

Chapter 1

Introduction

The underlying goal of particle physics is to understand the composition of the universe and the various interactions (forces) associated at the microscopic scale in the form of particles and the fields. In terms of the energy density; universe is comprised of the dark energy ($\sim$ 68%), dark matter ($\sim$ 27%), and ordinary matter ($\sim$ 5%) [6, 7, 40, 72]. The most successful explanation of particle physics so far is the 'Standard Model (SM)' which explains everyday matter in the form of fermions and the interactions with bosons. However, the SM fails to address the gravity, dark matter candidate, matter-antimatter asymmetry, neutrino mass. The Large Hadron Collider facility (LHC) has been operating since 2009 to find the answer to these questions. The LHC and the CMS experiment are discussed in Chapter 3. The most significant result from the LHC from its run 1 (2009-2012) operation was the discovery of the Higgs boson [56, 64] announced by ATLAS and CMS experiment at the LHC [31, 46]. This discovery gave the SM it's complete form; however, all the shortcomings of the SM remain the same as they were in the pre-LHC era. To answer these questions, beyond the standard model (BSM) physics is inevitable.

Many BSM theories such as extra dimensions, heavy-vector triplet predict new resonance (heavy) production of dibosons through gluon fusion and quark-antiquark annihilation, or weak vector boson fusion (VBF). The SM, extra dimension, and the heavy vector triplet method are discussed in Chapter 2. This analysis analyzes the Run2 (2016-2018) data from the LHC recorded by the CMS detector which is $\sim 5\times$ more data than Run1. This analysis targets the final states in which a pair of weak vector bosons are produced, one decaying to a pair of neutrinos, then the other decaying to a pair of quarks. To apply to a broad class of signal models, events will be categorized in terms of events that have been tagged as originating from the VBF process and events that have not been tagged. The VBF production mode offers distinct challenges to signatures that include neutrinos due to the nature of spin correlations that exist in these models. These features will be further described in Section 5.3.

As the resonances considered are heavy, the hadronically decaying boson (V) will have high momentum hence their decay products will be boosted such that their characteristic angular separation is $2m_{\mathrm{Z}}/p_{\mathrm{T,V}} \sim 100/500 \leq 0.4$. As a result, jet substructure techniques will be needed to identify such Z-bosons and to measure their mass. Selections and techniques employed to reconstruct the final state particles of these events and to suppress standard model backgrounds are discussed in Sections 4 & 5.4. Furthermore, the production of neutrinos, which produce missing transverse momentum (p_T^{miss}) in the detector, offers a convenient tool to trigger such signal events. For resonance masses greater than roughly 1 TeV, the typical p_T^{miss} expected is roughly $>$ 500 GeV, where the efficiency of trigger paths based solely on p_T^{miss} are expected to be fully efficient. Details of the triggers used and estimates of their efficiency based on data are presented in Section 4.1. Production of diboson pairs through the VBF mechanism can be distinguished by identifying pairs of high energy jets with large separation in pseudo-rapidity and large invariant mass. This analysis employs two categories of events, one in which additional jets are present and pass the selections discussed in Section 4.3.3 (VBF-tagged events), and events which fail this selection (ggF or VBFfail events).

This analysis uses the transverse mass ($\mathrm{m_T}$) between the reconstructed Z-boson and p_T^{miss} as a discriminating variable to constrain the background and extract the signal yields. These variables are discussed in Section 4.6. In general, the signal shapes are expected to have the Jacobian shape peaking near the resonance mass. This is largely true for ggF production mode; however, for VBF produced resonances of spin 1 or 2, due to the bimodal or trimodal distribution in the pseudorapidity, the $\mathrm{m_T}$ shapes are dramatically different. This is due to the dominance of the polarization effect in VBF production mode which is driven by the coupling of the resonance to the SM particles. This study is discussed in Section 5.3. This feature is also only present in the partially reconstructed final states hence, any model with non-standard decays, e.g. Z(qq)Z'($\chi\chi$) could have very different phenomenology, depending on the details of the model, and as such this analysis highlights a unique aspect of semi-visible resonance searches, which, to the best of our knowledge, has yet to be fully appreciated. This analysis utilizes the data-driven technique with minimal input from the simulation to predict the SM backgrounds. The procedures used to predict the

expected rate of SM backgrounds and the validation of such methods are described in Section 5.5. Results and interpretations are presented in Sections 5.8.

This dissertation also covers the hardware project carried out in the context of the high granularity calorimeter (HGCAL) for the high luminosity LHC upgrade plan of the CMS. The foreseen high luminosity LHC run is expected to deliver $\sim 10\times$ more data which is huge optimism for the physics analysis to explore the answers to the aforementioned shortcomings of the SM; however, this possesses a lot of challenges to the detectors mostly in the forward region. The current CMS endcap calorimeters cannot cope with such level of radiations hence CMS plans to replace its current endcap detectors with HGCAL which has Silicon and Scintillator as the active materials. The Silicon region will be covered with ~ 27000 modules built with Silicons cut from 8" wafers. The techniques to build/assemble the modules and cassettes based on the experience from the mockup program carried out at Texas Tech University (shares the responsibility of making 5000 of such modules which is half of the total US contribution for the standard 8" modules) and the Silicon detector facility at the Fermilab are discussed in Chapter 6. The conclusions and the perspective for future studies are presented in chapter 7.

Chapter 2

Theoretical Overview

The most successful theory of particle physics is the Standard Model (SM). Similar to the periodic table in chemistry, the SM categorizes the particles based on their characteristics.

2.1 The Standard Model

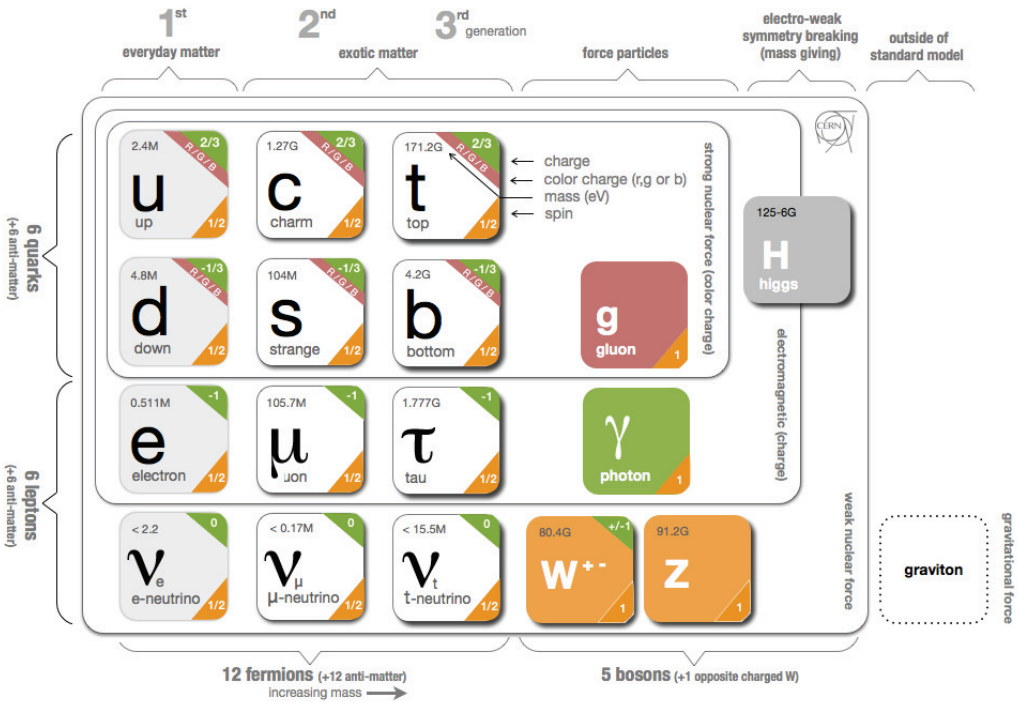

Figure 2.1. The Standard Model of the particle physics.

The standard model [62, 77, 78, 92, 95] is comprised of the elementary particles which are categorized as fermions and bosons as seen in figure 2.1 [20]. The fermions have spin 1/2 and follow the Fermi-Dirac statistics whereas bosons are integer spin

particles that follow the Bose-Einstein statistics. The fermions are further categorized into three generations with the same properties but different mass. The fermions are of two varieties i.e. quarks and leptons each of 6 types. The six quarks consist of three 'up-type' i.e. up, charm, and top quarks each has an electric charge of +2/3 and three 'down-type' i.e. down, strange, and bottom each having an electric charge of -1/3. The six leptons consist of electrons, muons, taus each having an electric charge of -1, and the three neutrinos (electron neutrinos, muon neutrinos, and tau neutrinos) which are all electrically neutral. Everyday matter is made up of the first generation of the fermions i.e. the combination of up-up-down quarks makes a proton while up-down-down quarks combination makes a neutron. The protons, neutrons, and electron(s) make atoms. For anything to happen in nature, force must act and the forces are carried by the gauge bosons seen in figure 2.1. The strong nuclear force is mediated by 'gluons', weak force such as radioactivity is mediated by the weak bosons '$W^{\pm}$, Z', and the electromagnetic force by the photon. The fourth force in nature i.e. gravity is not addressed by the SM and is mediated by a hypothesized boson, the graviton. The Higgs boson [56, 64] is responsible for giving mass to weak bosons via electroweak symmetry breaking and the fermions via Yukawa interaction in the Higgs condensate.

The SM is a mathematical construction of the particles and their interactions in terms of symmetry group; SU(3)×SU(2)×U(1), where 'SU(3)' is the special Lie group matrix of degree 3 with the determinant value of 1 and U(1) is the unitary matrix. SU(3) is the symmetry representation for the quantum chromodynamics (QCD) interaction which is the study of the color charge particles i.e. gluons and quarks. In general, the degree 'n' of the group matrix represents the number of the particles addressed by the respective symmetry such as SU(3) represents the three-color charge gluons (red, green, and blue), SU(2) represents the two weak bosons (W, Z), and the U(1) represents the photon which is just one type. The generators for the SU(n) symmetry group are given by $n^2 - 1$ hence giving 8 possible combinations for gluons which are represented by the 8 Gell-Mann matrices (3x3 matrices with the determinant of 1).

The unified electromagnetism and the weak forces also known as electroweak interactions are represented by SU(2)×U(1) group [59, 83, 94]. The interaction me-

diated by the photon is represented by the U(1) group and the weak bosons by the SU(2). The gauge invariance requires the particle to have no mass which is the case for the gluons and photons; however, the $W^{\pm}$, and Z are massive. The answer to the mass of these bosons is provided by the Higgs mechanism with spontaneously broken symmetry [56, 64] which proposes a scalar boson Higgs responsible for giving mass to these bosons and also to the fermions which have mass. The amount of mass that a particle gains depend on its interaction with the Higgs field i.e. more interaction gives more mass.

2.2 Beyond the Standard Model

The physics beyond the standard model (BSM) is inevitable to address the questions left unanswered by the SM as mentioned in Chapter 1. The BSM theories (models) considered in this dissertations are extra dimension and the heavy vector triplet method of the extension of the standard model which are discussed below.

2.2.1 Extra dimensions

The Randall-Sundrum (RS) model is the most popular and attractive setup of the warped extra dimensions as this model can potentially explain the large hierarchy between electroweak energy scale and the energy scale of gravity i.e., the weak nature of the gravity. The RS model proposes one extra dimension i.e. a fifth dimension which extends between the Planck energy scale and the TeV or weak energy scale (SM) in the form of a warped geometry [32, 75, 77, 79] as seen in figure 2.2. The extra-dimensional coordinate y=0 is at gravity brane and y=πR is at the weak brane. Here 'brane' refers to the 3D spatial plane for the respective scale. The 'y'-dependent 4D metric from solving the Einstein's equations is as follows:

$$ds^2 = e^{-2ky} dx^{\mu} dx^{\nu} \eta_{\mu\nu} + dy^2 \tag{2.1}$$

The metric in Eq. 2.1 corresponds to a 5D AdS space. The factor e^{-2ky} is called the "warp" factor and determines how 4D scales change as a function of the position in the extra dimension i.e. how the strength of the gravity varies with the

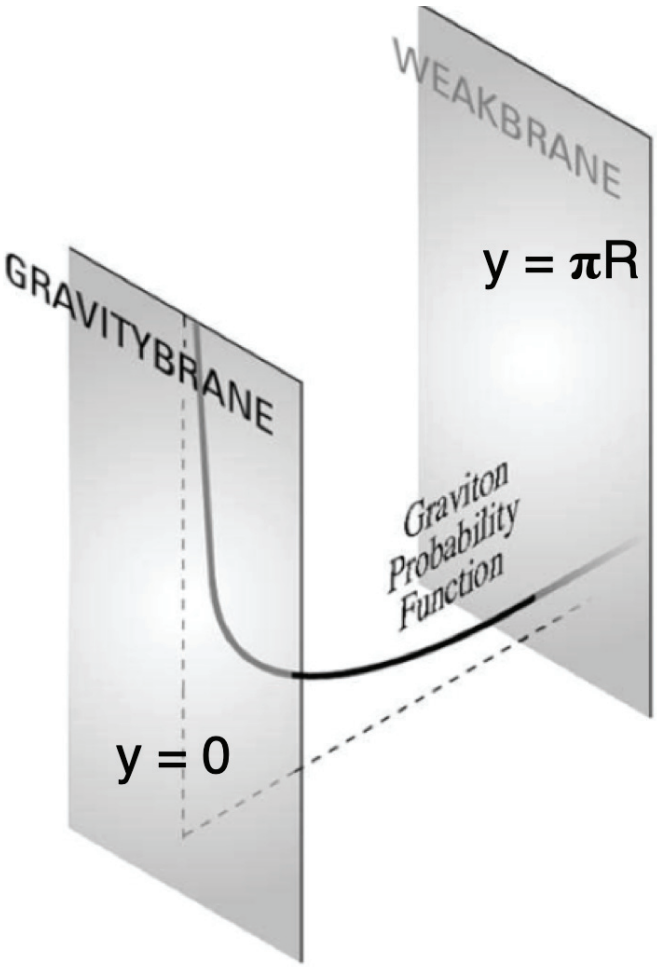

Figure 2.2. Schematics of the setup of the Randall-Sundrum model.

y. This indicates that the energy scales for 4D fields localized at the boundary at y = πR are red-shifted by a factor $e^{-k\pi R}$ with respect to those localized at y = 0. hence, the boundaries at y = 0 and y = πR are usually referred to as the ultraviolet (UV) and infrared (IR) boundaries, respectively [77]. In terms of the resonances, this analysis is targeting the Kaluza-Klein modes of the graviton. The massless mode is localized at the weak brane; however, the massive excitation modes of O(TeV) lives in the extra dimension near to the weak brane and these are deemed to be accessible at the collider experiment such as the LHC. The new scalar particle, the Radion is also a prediction of this model which is conceived as a necessity of a field to neutralize the tension between the weak brane and the gravity brane [60, 75].

The RS model describes the two scenarios which are the RS1 and the Bulk. In the RS1 scenario, only the graviton propagates through the bulk space or in the extra dimension while the SM particles are fixed in the weak brane whereas in the bulk scenario the SM particles in addition to the graviton propagate in the extra dimension. The analysis presented in this dissertation is in the context of the bulk scenario.

2.2.2 Heavy Vector Triplet

The many varieties of the extension of the standard model theories such as Composite Higgs [37, 61], Little Higgs [35, 84], and Sequential Standard Model (SSM) [33] predict heavy spin-1 resonances. The spin-1 resonance explored in this dissertation is based on a model-independent strategy called the heavy vector triplet (HVT) method [76]. The aim of the HVT method is to bridge between the experimental data and many theoretical models.

The heavy vector triplet (HVT) method proposes the heavy resonances in the form of a vector triplet, $V_\mu{}^a$, a = 1,2,3 representing three spin-1 vector bosons among which one is neutral and two are charged. The charge eigenstate of the field in this model are defined by:

$$V_\mu^\pm = \frac{V_\mu^1 \mp i V_\mu^2}{\sqrt{2}}; \quad V_\mu^0 = V_\mu^3 \tag{2.2}$$

Here, the neutral resonance corresponds to Z and the charged one to $W^\pm$; hence, these are often called the Z' or W' depending on the charge.

Chapter 3

Experimental Apparatus

An accelerator is one of the primary instruments used in particle physics experiments. Particles in the accelerator are provided by some source which varies among experiments. The length scale that we are trying to probe is very small and as suggested by the de Broglie equation i.e., $p = h/\lambda$, hence we need a very high energy beam of particles. The role of the accelerator is to speed up and increase the energy of a beam of particles by generating electric fields that accelerate the particles, and magnetic fields that steer and focus them [14, 15]. The world's largest accelerator is the large hadron collider (LHC) facility at the European Council for Nuclear Research (CERN). In this dissertation, the data collected by the Compact Muon Solenoid (CMS) detector for the years 2016-2018 is analyzed. The CMS detector is one of the four detectors in the LHC ring as seen in figure 3.1.

3.1 Large Hardron Collider (LHC)

The Large Hadron Collider is a two-ring accelerator which is 27 km in circumference and is 100 m underground at the border between France and Switzerland near Geneva. The LHC ring itself is a part of the CERN accelerator complex [74] as seen in 3.1. LHC is designed to collide proton beams with a centre-of-mass energy ($\sqrt{s}$) of 14 TeV and an unprecedented luminosity of 10^{34} cm^{-2} s^{-1} . It can also collide heavy (Pb) ions with an energy of 2.8 TeV per nucleon and a peak luminosity of 10^{27} cm^{-2} s^{-1} [38, 57].

A cylinder with highly compressed hydrogen is the source of the proton beams at the LHC. These hydrogen atoms are injected in a precisely controlled rate to the source chamber of the linear accelerator (LINAC2) where electrons are stripped off from the hydrogen leaving proton only. These protons are now accelerated with the electric field and are traveling with the speed of one-third of the speed of light (c) when leaving LINAC2. From LINAC2, protons go to the booster, and to maximize the intensity of the beam, protons are split into 4 booster rings. They are accelerated

in a booster by repeatedly circulating in the presence of the magnetic field (from powerful electromagnet to keep them in circular track) and pulsating electric field at a certain point (to accelerate). In booster, protons are accelerated up to 91.6% of c, and squeezes them closer together. After recombining the packet together they are now sent to the proton synchrotron (PS). Let's consider just two of such proton packets, they are circulated at PS for 1.2 seconds and gain the speed $\approx$ 99.9% of c. This speed is very close to the ultimate speed i.e. 'c' so they reached the point of transition, and the energy added from the pulsating electric field now can not raise the speed. Instead, the increased energy contributes to an increase in the mass of protons ($E = mc^2$). Here, protons reach the energy of 25 GeV i.e. protons are now 25 times heavier than they are at rest. They are now sent to Super Proton Synchrotron (SPS) ring where protons are more energized to 450 GeV and finally launched to the orbit (ring) of LHC. At the LHC ring, two vacuums (similar to the interplanetary space) pipes containing protons are traveling in the opposite direction and the pressure in these beam pipes is very low (about 10 times that on the moon). This is to ensure that the protons can travel around without hitting other gas particles or the wall of the pipes. The incoming protons are synchronized with those already circulating by the kickers' magnet near the injection point at the ring. So, one vacuum pipe has clockwise circulating protons, and another has anti-clockwise circulating protons. These counter rotating-beam cross over in four places at detector caverns (ATLAS, CMS, ALICE, LHCb), where they can be made to collide, and debris are tracked in the detector. SPS injects protons for about half an hour and finally, we will have 2808 packets of protons. At the LHC ring, some extra energy is added to each proton, whose speed is now so close to c, that it goes around the 27 Km ring over 11,000 times each second, getting a boost of energy from the pulsating electric field. Finally, each proton has an energy of 6.5 TeV (although the designed one is 7 TeV). Magnets are used to keep the protons in a circular ring of LHC for which the magnets need to be superconducting. This is achieved by operating magnets at 1.9 K which is 0.8 K colder than outer space [29, 82]. The steady magnet finally brings to the collision mode giving the center of mass energy ($\sqrt{s}$) of 13 TeV [73].

The main purpose of the LHC is to get the physics events from the collisions

of the particles at high energy. The number of events (N_e) per second generated in the LHC collisions is given by accelerator by [57]:

$$N_{event} = L\sigma_{event} \tag{3.1}$$

where σ_{event} is the cross section for the event under study and L the machine luminosity. The machine luminosity depends only on the beam parameters and can be written for a Gaussian beam distribution as:

$$L = \frac{N_b^2 n_b f_{rev} \gamma_r}{4\pi\epsilon_n \beta^*} F \tag{3.2}$$

where N_b is the number of particles per bunch, n_b the number of bunches per beam, f_{rev} the revolution frequency, γ_r the relativistic gamma factor, ϵ_n the normalized transverse beam emittance, β^* the beta function characterizing the beam size at the collision point, and F the geometric luminosity reduction factor due to the crossing angle at the interaction point (IP). The other factors which impact the luminosity are [38]:

- the beam emittance: needs to be confined within the small aperture of the LHC magnets.
- the thermal energy due to the synchrotron radiation must be absorbed by the cryogenic system as it limits the total intensity.
- the spreading of the beam (beam-beam effect) has to be minimized i.e. keeping below a certain limit.
- the space-charge limit (scales with N_b/ϵ_n) in the injectors.

This dissertation analyzes the collisions data at $\sqrt{s}$ = 13 TeV from Run2 corresponding to the years 2016-2018. The peak instantaneous luminosity achieved

were 1.53, 2.066, and 2.140 $\times 10^{34}$ cm^{-2}s^{-1} for the years 2016, 2017, and 2018 respectively [16]. The total integrated luminosity for those years are shown in figure 3.2 . The designed luminosity for the LHC is 1×10^{34} cm^{-2}s^{-1}, but recently LHC has exceeded it's design luminosity.

3.2 The Compact Muon Solenoid (CMS) Detector

The CMS detector [25, 44, 58] is one of the four detector in the LHC ring (see figure 3.1) located near Cessy in France. The CMS detector (also the ATLAS detector) is a general-purpose detector with the scope of diverse physics programs (Higgs, extra dimensions, dark matter, supersymmetry, etc.).

The CMS detector as seen in figure 3.3 [3] is 21 meters long, 15 meters wide and 15 meters high. One of the key features of the CMS detector is that it is built around a huge cylindrical coil (solenoidal structure) of the superconducting cable of 6 m internal diameter which provides a magnetic field of 3.8 T, about 100,000 times the magnetic field of the Earth. The field is confined by a steel "yoke" that forms the bulk of the detector's 14,000-tonne weight [2]. The CMS detector has various sub-detectors: silicon pixel and strip tracker, electromagnetic calorimeter made up of lead tungstate crystal, and a hadron calorimeter made up of brass and scintillator within the solenoid. Also, CMS has gas-ionization detectors to identify the muons in the steel flux-return yoke outside the solenoid. The hermetic structure of the CMS detector facilitates the precise measurement of p_T^{miss}. A brief description of these individual components of the CMS detector is presented below and a more detailed description can be found in Ref. [44].

3.2.1 The Coordinate System

CMS uses the right-handed coordinate system with origin centered at the nominal collision point inside the detector. As seen in figure 3.4 [18], the x-axis points radially inward towards the center of the LHC ring, the y-axis points vertically upward, and the z-axis points along the beam direction [44]. In terms of spherical coordinates, the polar angle (θ) is measured from the z-axis, the azimuthal angle (ϕ) is measured from the x-axis in the x-y plane, and the radial coordinate (r) is measured

from the origin in the x-y plane. However, one of the most commonly used coordinate is pseudorapidity (η) which is related to θ as:

$$\eta = -ln(tan(\theta)) \tag{3.3}$$

3.2.2 Tracking System

The type of particles produced from the collision at the center of the CMS detector is quite varied. Due to the presence of the magnetic field, charged particles travel in a curved trajectory and the bending of the trajectory depends on the momentum of the particles. The particle with less momentum has a high curved path and vice-versa. Tracking the path of the particle is crucial to accurately identify the particle and its properties. The precise position of the charged particle passing through the tracker is recorded by the tracker which is used to reconstruct the track of the particles [21]. Since the tracker is the inner most layer of the CMS detector residing i.e. closest to the collision point, it receives the highest amount of particles and hence the radiation. Therefore, the tracker detector materials are carefully chosen to cope with such radiations.

The CMS tracker [44, 65] system is comprised of two pixels at the core and strips surrounding the pixel, both with an active material of silicon. The schematic cross-section of the tracker is shown in figure 3.5. The tracker is cylindrical with a dimension of 2.5 meters in diameter and 5.8 meters in length and covers the $|\eta| < 2.5$.

The pixel detector comprises three cylindrical layers (barrel) of modules around the interaction point at the radii of 4.4,7.3 and 10.2cm and two disks of modules on each side. The pixel detector covers an area of $\sim 1m^2$ and has 66 million pixels. The strip detector covers the radial distance between 20cm and 116cm and has three subsystems i.e. the Tracker Inner Barrel and Disks (TIB/TID), Tracker Outer Barrel (TOB), and Tracker EndCaps (TEC+ and TEC-). TIB/TID consists of four-barrel layers and three disks at each end and extends in radius up to 55 cm. TOB consists of six-barrel layers, has an outer radius of 116 cm, and extends in z between $\pm$118 cm. TEC which closes off the tracker covers the region 124 cm $<$ |z| $<$ 282 cm and 22.5 cm $<$ |r| $<$ 113.5 cm and is composed of 9 disks [19]. The strip detector has 198

m2 of active silicon area and 9.3 million strips.

3.2.3 Electromagnetic Calorimeter

The purpose of the electromagnetic calorimeter (ECAL) is to measure electromagnetic particles like electrons, photons. The CMS ECAL as seen in figure 3.6 [36] consists two parts; barrel ($|eta| < 1.479$) and two endcaps ($1.479 < |eta| < 3.0$) and sits between the tracker and the hadronic calorimeter. ECAL is made up of lead tungstate material with 61,200 crystals in the barrel and 15,000 crystals in the endcap. Besides, ECAL also has a Pre-shower detector that sits in front of the endcaps and contributes to extra spatial precision.

3.2.4 Hadronic Calorimeter

The purpose of the hadronic calorimeter (HCAL) [12, 27, 36] is to detect the hadrons (things made up of quarks and gluons). It also gives information about the missing transverse energy (E_T^{miss}). As seen in figure 3.7 [44], HCAL consists of four components : barrel (HB) at $|\eta| = 1.3$, endcap (HE) at $1.3 < |\eta| < 3$, forward (HF) at $3 < |\eta| < 5.2$, and outer (HO). The HO also is known as a tail catcher that sits outside the magnet with the purpose of catching the leftover shower that escapes out of HB. HB and HE are the sampling calorimeters (i.e. finds the energy, position, and arrival time of particle using alternative layers of absorber and scintillator material which produce the light pulse as the particle hits and pass through it) made up of brass absorber plates and scintillator sheets as the active medium. Hybrid photodiodes (HPD) is used as the readout instrument to read signal (light) from the scintillator. HF has a high radiation damage risk as it receives the most particle flux close to the beamline, so it uses steel as an absorber and quartz fiber as an active material benefitting from their radiation hardness. HCAL has granularity of $\Delta\eta \times \Delta\phi = 0.087 \times 0.087$ for $|\eta| < 1.6$, and $\Delta\eta \times \Delta\phi = 0.17 \times 0.17$ for $|\eta| \geq 1.6$ [69].

3.2.5 Muon System

The purpose of the muon system is to precisely measure the muons. Since muons can penetrate several meters of materials without interacting hence, the muon systems are placed furthest out where they are the only particle likely to produce the signal [8]. As seen in figure 3.8, the muons system consist of three components (drift tube (DT), cathode strip chamber (CSC), and resistive plate chamber (RPC)) and all of them sit outside of the magnet [36, 44, 45]. The DT is located in barrel region up to $|\eta| = 1.3$, and has 4 stations (MB1-MB4). CSC is located in endcap region up to $|\eta| = 2.4$, and has 4 stations (ME1-ME4). RPC is located in both barrel and endcap regions. RPCs are gaseous plate chambers that give good spatial and time resolution in addition to faster timing for a signal.

3.2.6 Trigger System and Data Acquisition

Collisions at the center of the CMS detector happen every 25 ns. This produces huge amounts of data which is impossible to store all. Hence, events of interest are selected using a two-tiered trigger system [68]. The first level (L1) as seen in figure 3.9, composed of custom hardware processors, uses information from the calorimeters and muon detectors to select events at a rate of around 100 kHz within a time interval of less than 4 μs. The second level, known as the high-level trigger, consists of a farm of processors running a version of the full event reconstruction software optimized for fast processing and reduces the event rate to around 1 kHz before data storage. The triggers used to record the data used in this dissertation are discussed in Section 4.1.

The Data Acquisition system (DAQ) manages the overall flow of data. As seen in figure 3.10 [44], it comprises of detector frontend, readout modules, event builder, and monitoring systems. It assembles the data fragments from the detector fragments with the trigger information and ultimately sends it to the data storage center such as tier-0 site at CERN [69].

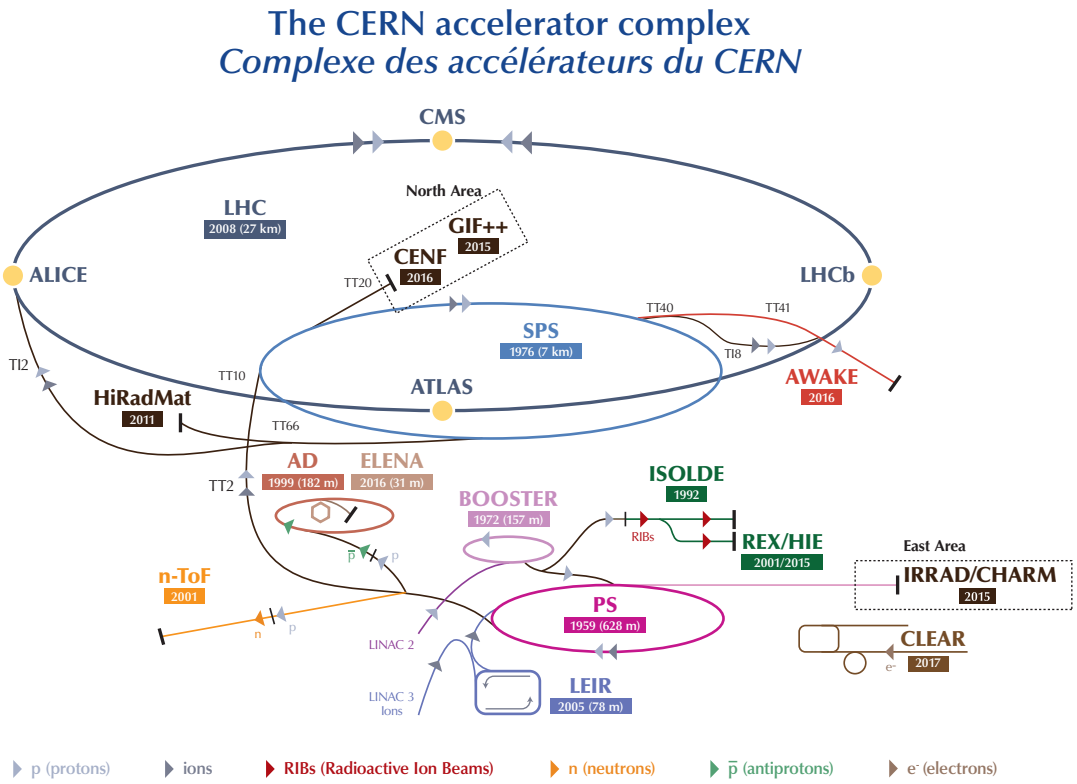

Figure 3.1. CERN Accelerator Complex.

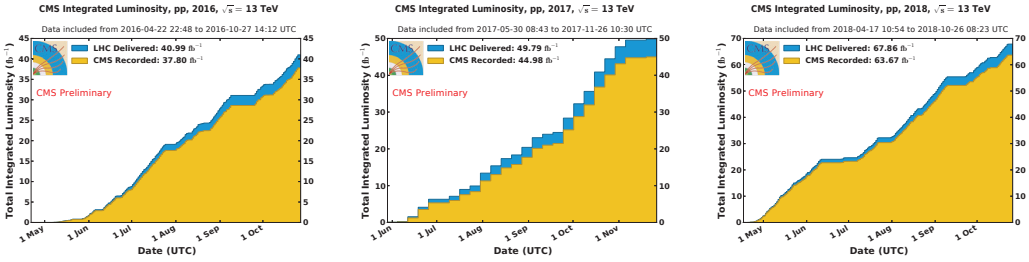

Figure 3.2. The integrated luminosity delivered by the LHC and recorded by the CMS detector during the proton-proton collisions runs at $\sqrt{s} = 13$ TeV in the years 2016-2018 (from left to right).

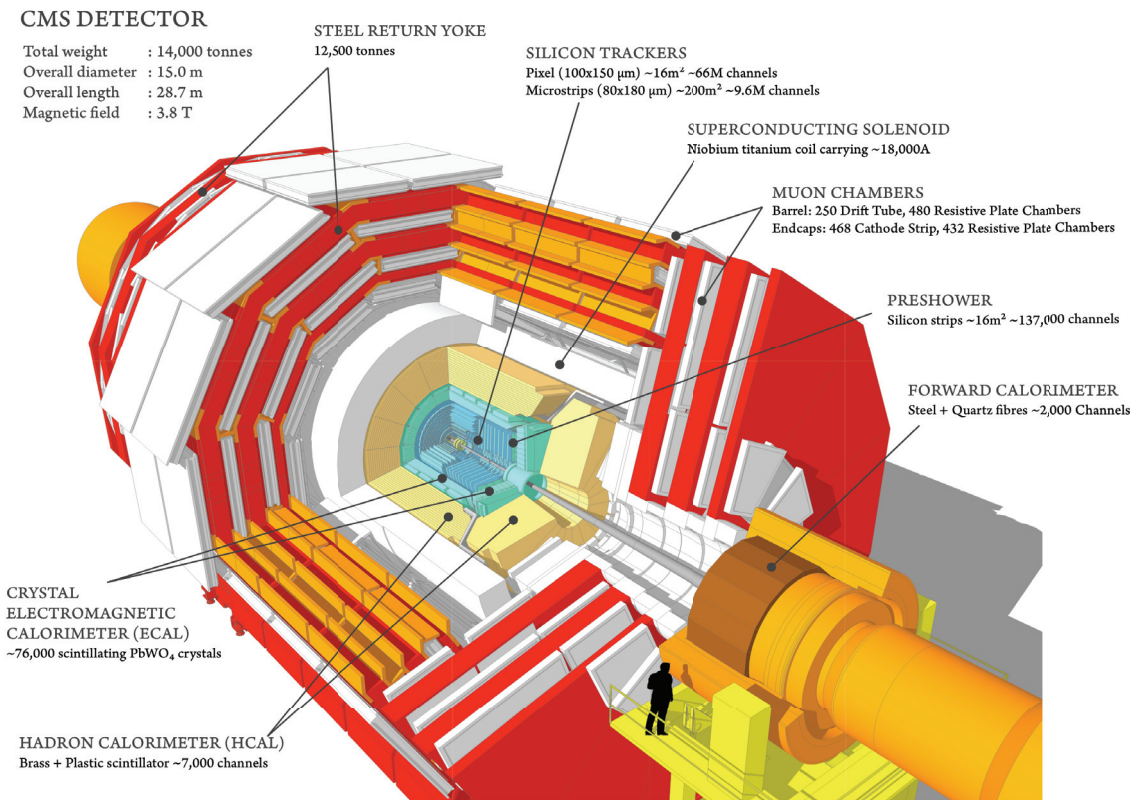

Figure 3.3. Sectional view of the CMS detector.

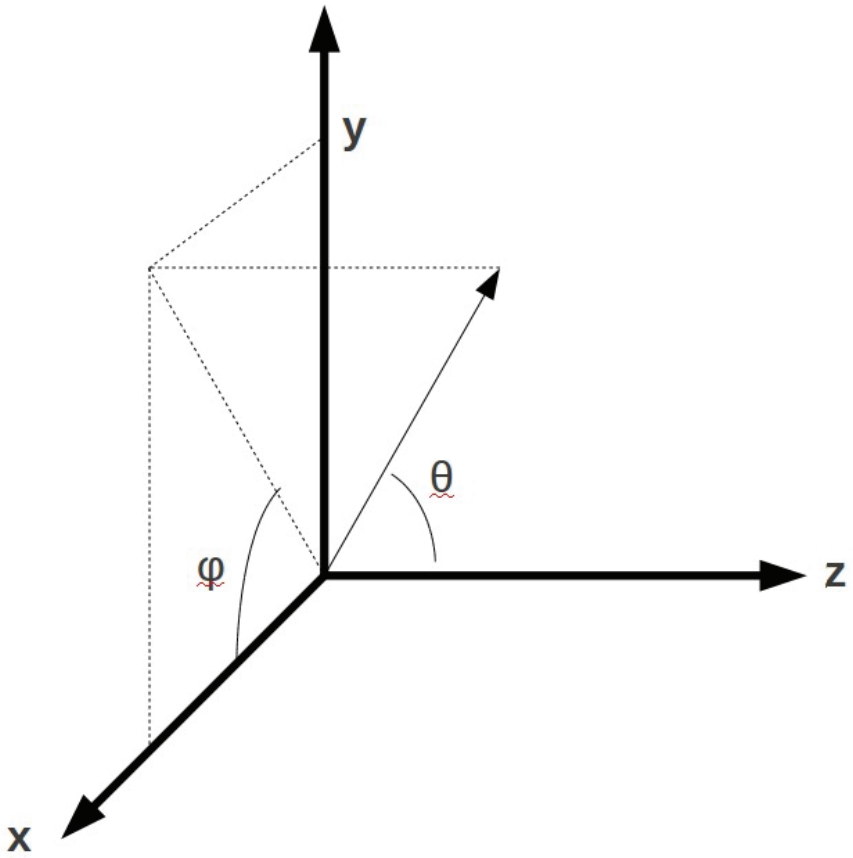

Figure 3.4. CMS coordinate system.

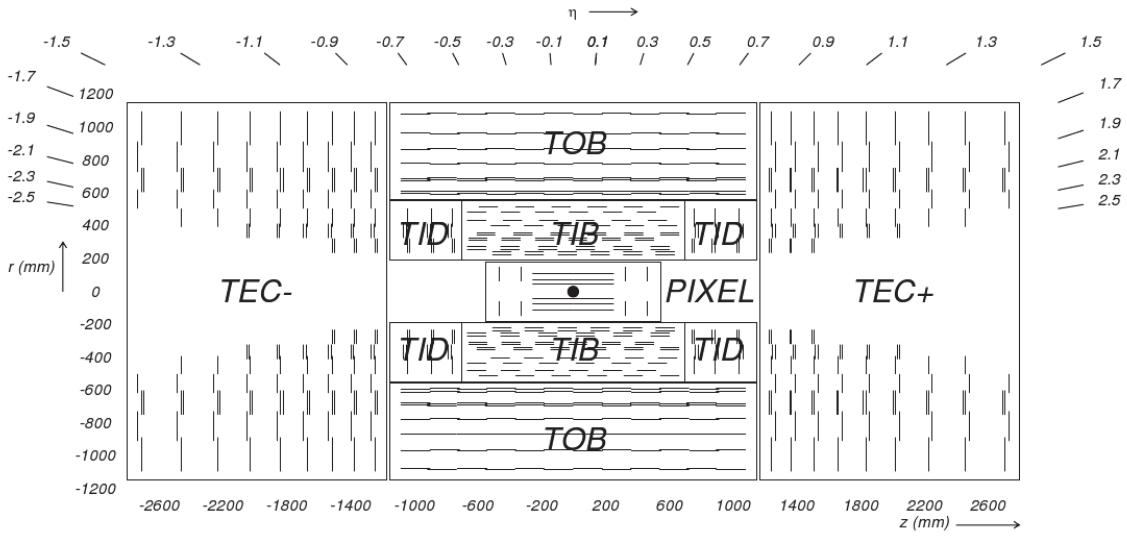

Figure 3.5. Schematic cross section through the CMS tracker.

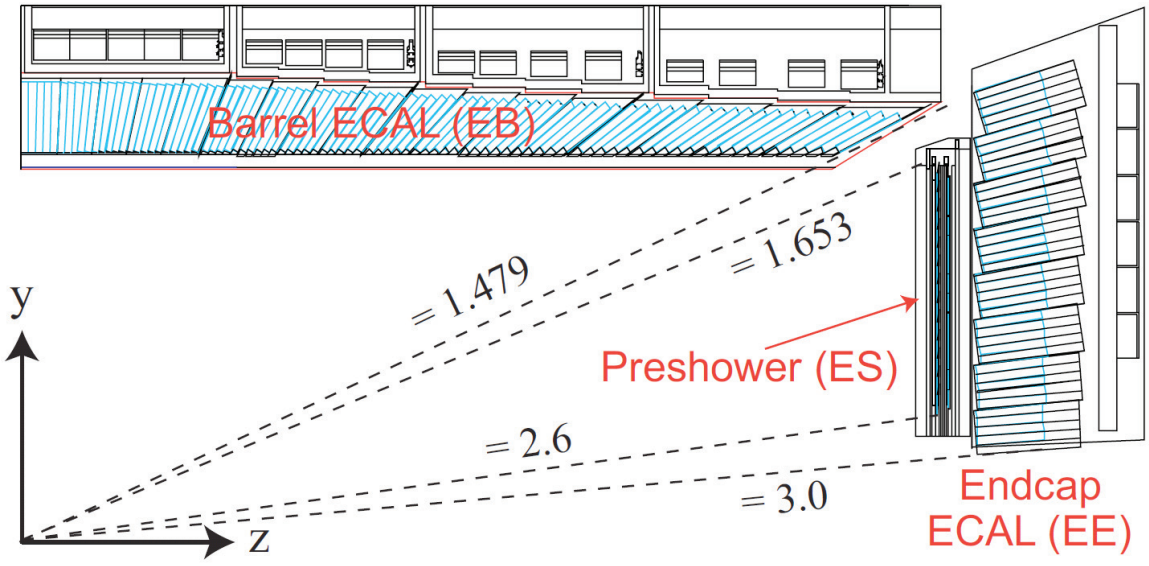

Figure 3.6. Transverse section through CMS ECAL, showing geometrical configuration.

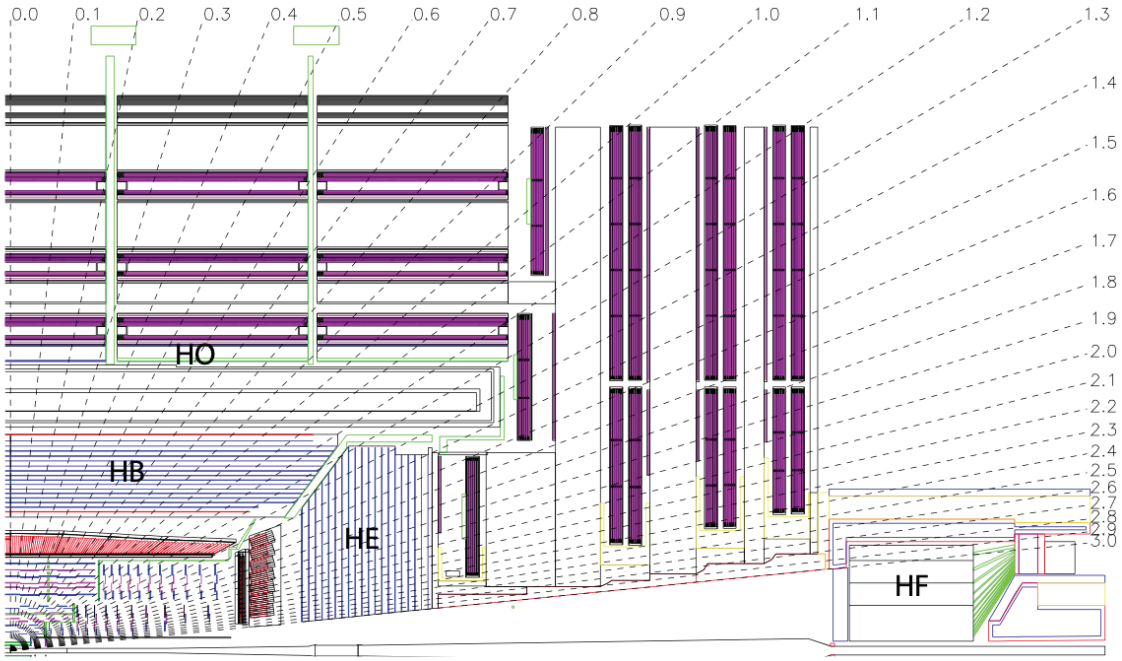

Figure 3.7. Longitudional view of one quadrant of the CMS detector showing the HCAL components.

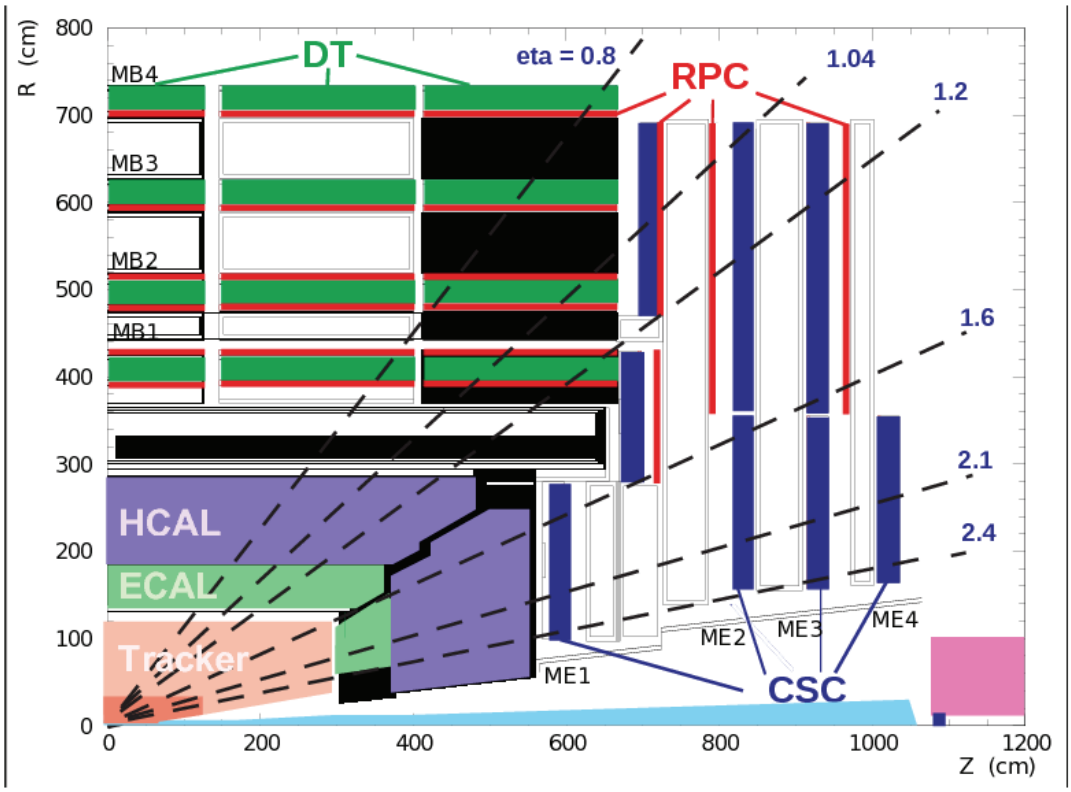

Figure 3.8. Longitudional view of one quadrant of the CMS detector showing the Muon system components.

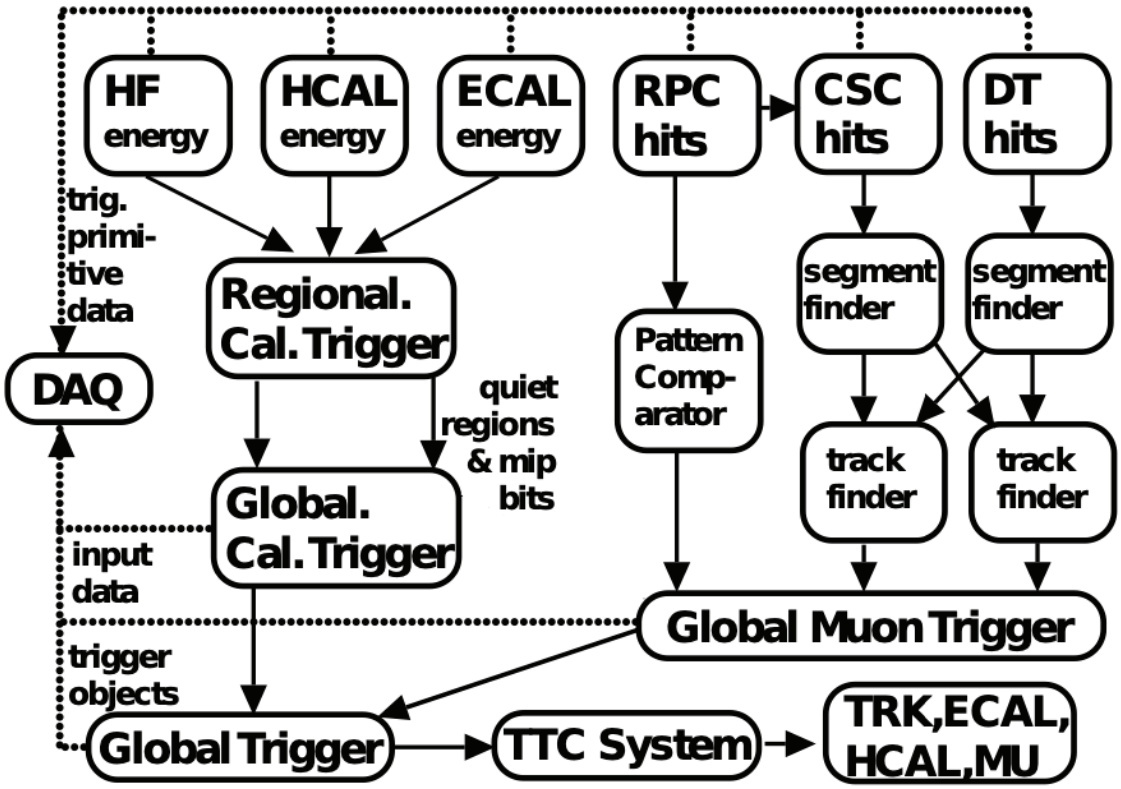

Figure 3.9. Overview of the CMS L1 trigger system.

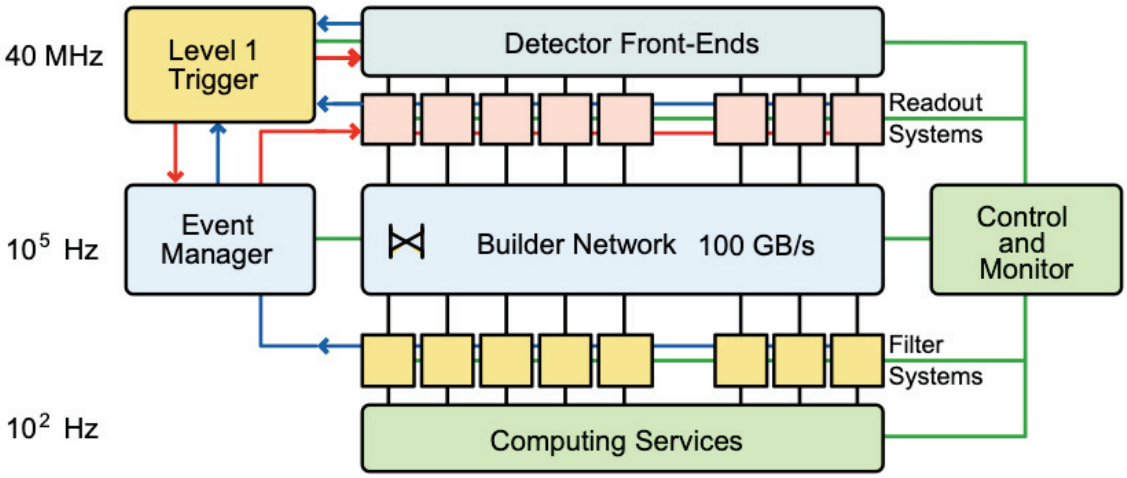

Figure 3.10. Architecture of the CMS DAQ system.

Chapter 4

Physics Objects and Event Selections

4.1 Triggers

The data used in this analysis were recorded by the CMS experiment in the years 2016, 2017, and 2018 using a set of p_T^{miss}-H_T^{miss}-based triggers, denoted by the logical OR of all of the HLT paths listed below:

- `HLT_PFMETX_PFMHTX_IDTight (X=90,100,110,120,130,140)`

Here, `X` corresponds to the threshold applied to the online p_T^{miss} and H_T^{miss} ($H_T^{\text{miss}} = \left|\sum_{\text{jets}} \vec{p}_T\right|$), as calculated by the particle flow (PF) algorithm.

As the single electron and single muon datasets have the events with the real p_T^{miss} from neutrinos, this is a relevant phase space to study our trigger performance. Also, the performance of the aforementioned triggers in the signal region of this analysis is measured using the single electron and single muon datasets requiring events to pass the following reference triggers:
`HLT_EleX_WPTight_Gsf(X=27,32)` for events from single-electron dataset, and
`HLT_IsoMu24 OR HLT_IsoTkMu24` for events from the single-muon dataset.

As seen in figure 4.1, the triggers almost fully efficient (plateaus around 98%) for $p_T^{\text{miss}} > 250$ GeV and greater than 75% at p_T^{miss} of 200 GeV. The measured trigger efficiencies are applied to MC to model the effect of p_T^{miss}-dependent trigger inefficiency. The efficiency derived from the single-electron dataset is used as weights applied to simulated events. The efficiencies derived from single-muon events are used to estimate uncertainty, taken to be the ratio of the efficiencies (as shown in figure 4.1) calculated with single-electron and single-muon datasets. These uncertainties will be applied to final yield estimates of the signal and resonant backgrounds, which are derived from simulation directly.

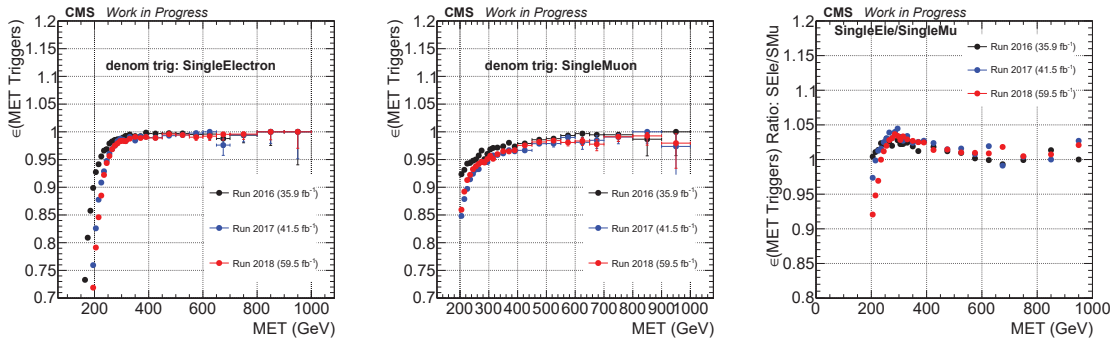

Figure 4.1. Measured trigger efficiency using single electron (left), single muon (middle) dataset and the ratio of th two (right).

4.2 Event reconstruction

In CMS data events are reconstructed using the particle-flow (PF) algorithm [47, 85], which uses information from all detectors i.e., tracker, ECAL, HCAL, and muon systems to identify and reconstruct the particles such as electrons, muons, charged or neutral hadrons, or photons. The physics objects used in this calculation are the jets, leptons, missing transverse energy (MET), and the transverse mass (m_T). Various physics objects groups (POGs) provides recommendations for the specific objects regarding filters, corrections, scale factors, etc. to improve the data quality when needed.

4.3 Jets

Jets used in this analysis are reconstructed from particle-flow (PF) candidates using the anti-k_T algorithm [43] with the size parameter 0.4 (AK4; to require the presence of the forward jets and to veto the presence of b-tagged jets in the event) and 0.8 (AK8; to select boosted V boson candidates decaying to jets (see Section 4.3.1)).

AK4 jets used in this analysis are clustered with charged hadron subtraction (CHS) technique i.e., charged particles that emerge from vertices other than the primary vertex are removed from the list of physics objects used for jet clustering to reduce the impact of pileup collisions. No explicit subtraction of leptons from jet clustering is performed. The jet 4-momenta are corrected for residual pileup

contributions, arising mainly from neutral particles, and for detector response effects using the standard level-1, 2, and 3 corrections [50]. To account for the run-period conditions for the jet energy measurements, separate corrections are applied for each run period as recommended by the JetMET POG. Also, jets used in the analysis are required to have $p_T > 30$ GeV and satisfy the jet ID criteria [63].

4.3.1 V-tagging

To identify the hadronic decay of boosted W and Z bosons, we used the highest p_T AK8 jet clustered with pileup per particle identification (PUPPI) algorithm [39]. PUPPI mitigates the effect of pileup on jet observables. PUPPI uses local shape information, event pileup properties and tracking information together to compute a weight describing the degree to which a particle is pileup-like. A local variable α is computed which contrasts the collinear structure of QCD with the soft diffuse radiation coming from pileup. The distribution of α for charged pileup, assumed as a proxy for all pileup, is then used to calculate a weight for each particle on an event-by-event basis.

In identifying jets from hadronic decays of boosted W or Z bosons we make use of two variables based on the jet grooming and substructure. Firstly, we use the soft drop mass (m_J) [70] of the AK8 jet to obtain the W or Z boson peak then we use the N-subjettiness ratio ($\tau_{21} = \tau_2/\tau_1$) to separate the two-prong hadronic decays of the W and Z bosons from QCD jets [90]. N-subjettiness is not an algorithm but an observable, and the value of the observable are obtained from the four-vector. τ_N is expressed as:

$$\tau_N = \frac{1}{d_0} \sum_i p_{ti}\ min\{\Delta R_{i,1}, \Delta R_{i,2}, \cdots, \Delta R_{i,N}\} \tag{4.1}$$

where N is the number of prongs, d_0 is the normalization factor which makes τ_N dimensionless, i represents all constituents of the jet, and $\Delta R_{i,N}$ is the distance of the particle from the subjet (N) axis. This is simply taking all the particles in a jet with their p_t, and weighting their p_t by the distance to a subjet axis. As seen in figure 4.2, the value of the observable falls between 0 to 1 with the higher the value representing more QCD like jets and smaller the value more heavy object (Z,

W, H, top) like. These two variables (m_{J} and τ_{21}) are used for event categorization (see Section **??**). The correction for soft-drop mass is applied as recommended by JMAR [52] The performance of the correction in the soft-drop mass in a signal sample with baseline selection (before applying mass cut for categorization) is shown in figure 4.3. Currently, the correction from 2016 is applied to all years as suggested by JMAR. In addition, the *stochastic smearing* is applied as suggested [51].

AK8 jet is required to have $\mathrm{p_T} > 200$ GeV, $|\eta| < 2.5$, charged hadron fraction (CHF) > 0.05, and neutral electromagnetic fraction (NEMF) < 0.9.

4.3.2 b-jets

The number of selected jets satisfying the deep secondary vertex b-tagging algorithm [86] at the medium working point is used as a discriminating variable to tag a b-jet. In order to suppress the top background, b-jets are vetoed in this analysis.

4.3.3 VBF jets

Resonance produced via VBF production mode has two jets in the forward region. The requirement for tagging such forward jets are

- There should be at least 2 AK4 jets with $\mathrm{p_T} > 30$GeV.
- Those jets should not overlap with AK8 jet or coming from Z boson decay.
- They are required to appear in the opposite hemisphere of the detector by requiring, $\eta_{j1} \times \eta_{j2} < 0$.
- Require $\Delta\eta_{\mathrm{jj}}^{\mathrm{VBF}} > 4.0$ and forward dijet invariant mass $m_{\mathrm{jj}}^{\mathrm{VBF}} > 500$ GeV. to have more signal like events.
- If there were more than one candidate pair of such jets then the one with the larger m_{jj} was considered.

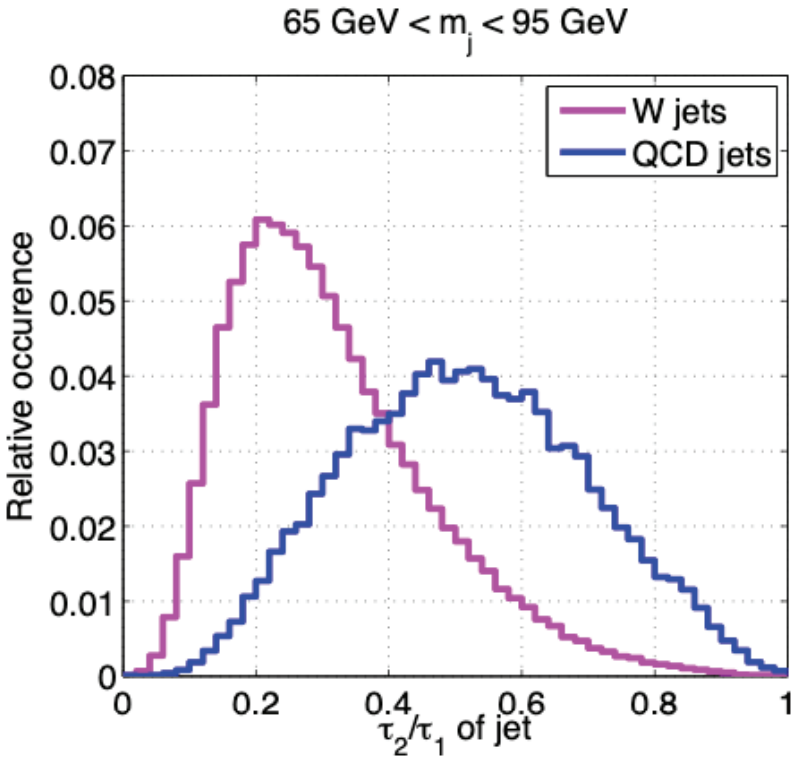

Figure 4.2. τ_{21} distribution for the boosted W and QCD jets.

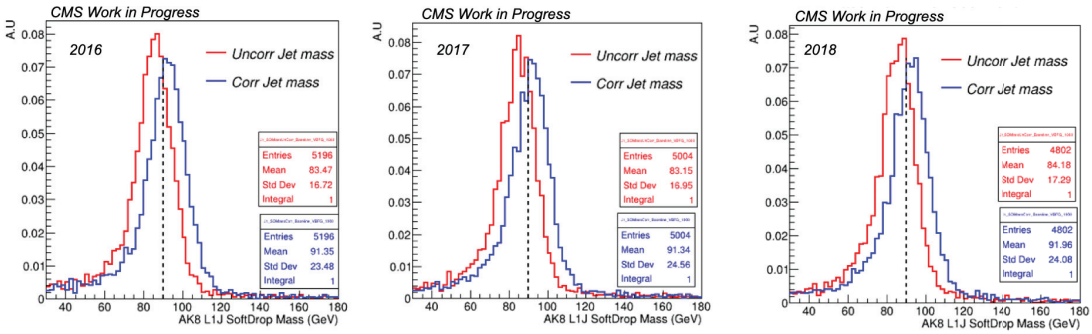

Figure 4.3. Distribution of the AK8 leading jet soft-drop mass before (red) and after (blue) correction. From left to right: signal sample (1 TeV VBF Gravtion) for 2016, 2017, and 2018.

4.4 Leptons

In this dissertation, the final state considered is with jets and the missing transverse energy only. Hence, the leptons and photons are vetoed as described below:

4.4.1 Electrons

Electrons are identified by a track and an ECAL cluster, with a momentum-to-energy ratio compatible with unity, and not connected to an HCAL cluster [85]. Furthermore, Electron candidates are selected using the POG-recommended "Cut Based VETO" selection. The electrons are required to have $p_T > 10$ GeV and appear in $|\eta| < 2.5$. Electron candidates are required to satisfy an isolation requirement of $I_{\text{mini}} < 0.1$, where I_{mini} is the mini-isolation variable described in Ref. [80]. Electron events satisfying these criteria are vetoed.

4.4.2 Muons

Muons are identified by connecting a track in the inner tracker to a track in the muon detectors [85]. Muon candidates are selected using the POG-recommended "Medium Muon" selection which require muons to have $p_T > 10$ GeV and appear in $|\eta| < 2.4$. Muons are required to satisfy an isolation requirement of $I_{\text{mini}} < 0.2$

to differentiate between prompt and the one coming from b-hadron. Muon events satisfying these criteria are vetoed.

4.4.3 Taus

In the top, W+jets background events, the hadronic τ (coming from W boson) decay along with other leptons which were not identified or doesn't meet the criteria for the electron or muon candidates contributes to the signal region phase space of this analysis. Hence, a veto based on isolated charged tracks was used to suppress such events.

Leptonic tracks are required to have $\mathrm{p_T} > 5$ GeV and $I_{\mathrm{tk}} < 0.2$, where I_{tk} is the scalar $\mathrm{p_T}$ sum of other charged tracks within $\Delta R \equiv \sqrt{(\Delta\phi)^2 + (\Delta\eta)^2} < 0.3$ of the primary track, divided by the $\mathrm{p_T}$ value of the primary track whereas the hadronic tracks are required to have $\mathrm{p_T} > 10$ GeV and $I_{\mathrm{tk}} < 0.1$ to reduce hadronic (non-τ) signal loss.

4.5 Photons

Photon candidates are required to have $\mathrm{p_T} > 100$ GeV, $|\eta| < 2.4$, and isolated from neutral hadrons, charged hadrons, and electromagnetic particles, excluding the photon candidate itself [67]. The isolation requirements are on the energy within a cone of $\Delta R < 0.3$ around the photon momentum direction, corrected for pileup with the per-event average pileup energy density and per-photon η-dependent effective areas. Photon candidates are further required to have no associated pixel seed. Events with a photon satisfying these criteria are rejected.

4.6 Missing transverse energy (p_T^{miss}) and transverse mass ($\mathrm{m_T}$)

The missing transverse momentum, p_T^{miss}, is defined as the negative vector sum of the transverse momenta of all PF candidates and is calibrated taking into account the jet energy corrections. Dedicated event filters designed to reject instrumental noise are applied to further improve the correspondence between the reconstructed and the genuine p_T^{miss} [88]. To suppress backgrounds characterized by the presence

of a single W boson decaying leptonically, and without any other significant source of p_T^{miss} apart from the neutrino from this process, we use the quantity $\mathrm{m_T}$, defined as the transverse mass of the system consisting of the highest $\mathrm{p_T}$ $AK8$ jet and the missing transverse momentum vector,

$$\mathrm{m_T} = \sqrt{2\mathrm{p_T^J p_T^{miss}}[1 - \cos\Delta\phi]}, \tag{4.2}$$

where $\Delta\phi$ is the difference between the azimuthal angle of the $AK8$ jet's momentum and $\vec{p_T^{\text{miss}}}$.

In order to select the invisibly decaying Z boson events, we require $p_T^{\text{miss}} > 200$ GeV and all p_T^{miss} event filters. In addition, to protect against particle flow failures, events are rejected if PFMET/CaloMET > 5.

4.7 Angular cut

The majority of QCD multijet events in our high-p_T^{miss} search region have jets with under measured momenta and thus a spurious momentum imbalance. A signature of such an event is a jet closely aligned in direction with the p_T^{miss} vector. To suppress this background, we reject all events in which the four highest-$\mathrm{p_T}$ jets lie within 0.5 radians of the p_T^{miss} vector in the azimuthal coordinate.

Chapter 5

Search for New Bosons in Gluon-Gluon and Vector Boson Fusion Processes at the LHC

5.1 Overview

This analysis searches for resonances in E_T^{miss} + boosted jet in the final state for ggF production mode and an additional two forward jets in the VBF production mode. The samples (data, background, signal) samples are chosen based on this phase space. Samples, signal characterization, various analysis strategies including the validation, and the results are presented in this chapter.

5.2 Data and simulated samples

The analysis presented in this dissertation used the MET primary datasets collected during the proton-proton collisions in the years 2016, 2017, and 2018 by the CMS detector $\sqrt{s}$ =13 TeV. The total dataset corresponds to the integrated luminosity of 137 fb^{-1} [42].

5.2.1 Standard model MC samples

The SM background samples used in this analysis are Z($\nu\nu$)+jets, W(lν)+jets which have a significant contribution to the p_T^{miss} and are irreducible and dominant background. The other sets of background are the top events where the semi-leptonic top decay contributes to this phase space. Lastly, the diboson and the other rare processes contributing to this phase space (one hadronic and other leptonic/invisible decay of the bosons) are also considered. These SM samples are listed in tables 5.1-5.2 with the cross-sections corresponding to next-to-next-to-leading-order (NNLO) calculations unless otherwise noted and obtained from the link [1]. In the case of $t\bar{t}$ MC samples, for the non-HT binned sample, we apply the cut of 600 GeV on HT calculated by MadGraph allowing this sample to be summed with the HT-binned

[1] https://twiki.cern.ch/twiki/bin/viewauth/CMS/SummaryTable1G25ns

samples and fill in the missing phase space of the HT-binned samples.

Table 5.1. SM $Z \to \nu\nu$+jets & $W \to l\nu$+jets i.e. V+jets MC samples used in the analysis. The cross sections are calculated to NNLO.

Dataset	σ (pb)
ZJetsToNuNu_HT-100To200_13TeV-madgraph	344.83
ZJetsToNuNu_HT-200To400_13TeV-madgraph	95.53
ZJetsToNuNu_HT-400To600_13TeV-madgraph	13.20
ZJetsToNuNu_HT-600To800_13TeV-madgraph	3.148
ZJetsToNuNu_HT-800To1200_13TeV-madgraph	1.451
ZJetsToNuNu_HT-1200To2500_13TeV-madgraph	0.355
ZJetsToNuNu_HT-2500ToInf_13TeV-madgraph	0.009
WJetsToLNu_HT-100To200_TuneCP5_13TeV-madgraphMLM-pythia8	1627.45
WJetsToLNu_HT-200To400_TuneCP5_13TeV-madgraphMLM-pythia8	435.24
WJetsToLNu_HT-400To600_TuneCP5_13TeV-madgraphMLM-pythia8	59.18
WJetsToLNu_HT-600To800_TuneCP5_13TeV-madgraphMLM-pythia8	14.58
WJetsToLNu_HT-800To1200_TuneCP5_13TeV-madgraphMLM-pythia8	6.660
WJetsToLNu_HT-1200To2500_TuneCP5_13TeV-madgraphMLM-pythia8	1.608
WJetsToLNu_HT-2500ToInf_TuneCP5_13TeV-madgraphMLM-pythia8	0.039

5.2.2 Higher-order corrections

The Z+jets and W+jets samples used in this analysis are the LO HT binned samples and are reweighted using the higher-order corrections separately corresponding to NLO Quantum Chromodynamics (QCD) and NLO Electroweak (EWK) terms. Scale factors corresponding to the NLO EWK corrections are obtained from [71] and applied as a function of the generator-level boson p_T. The NLO QCD scale factors are taken directly from the Monojet group as mentioned here [91] and the EWK NLO scale factors are shown in Figure 5.1.

5.2.3 Signal Samples

Three benchmark models are considered: $X \to ZZ \to q\bar{q}\nu\bar{\nu}$, where X is either a bulk graviton or a radion, and $W' \to WZ \to q\bar{q}\nu\bar{\nu}$. Signal samples were generated using MadGraph5_aMCNLO [34] for generation, pythia [89] for hadronization, and

Table 5.2. SM single-top, $t\bar{t}$, diboson, and other rare processes MC samples used in the analysis. The cross sections are calculated to NLO.

Dataset	σ (pb)
ST_s-channel_4f_leptonDecays_13TeV-amcatnlo-pythia8_TuneCUETP8M1	3.340
ST_t-channel_top_4f_inclusiveDecays_13TeV-powhegV2-madspin-pythia8_TuneCUETP8M1	136.02
ST_t-channel_antitop_4f_inclusiveDecays_13TeV-powhegV2-madspin-pythia8_TuneCUETP8M1	80.95
ST_tW_antitop_5f_NoFullyHadronicDecays_13TeV-powheg_TuneCUETP8M1	19.47
ST_tW_top_5f_NoFullyHadronicDecays_13TeV-powheg_TuneCUETP8M1	19.47
TTJets_SingleLeptFromT_TuneCP5_13TeV-madgraphMLM-pythia8	182.72
TTJets_SingleLeptFromTbar_TuneCP5_13TeV-madgraphMLM-pythia8	182.72
TTJets_DiLept_TuneCP5_13TeV-madgraphMLM-pythia8	88.34
TTJets_HT-600to800_TuneCP5_13TeV-madgraphMLM-pythia8	2.685
TTJets_HT-800to1200_TuneCP5_13TeV-madgraphMLM-pythia8	1.096
TTJets_HT-1200to2500_TuneCP5_13TeV-madgraphMLM-pythia8	0.194
TTJets_HT-2500toInf_TuneCP5_13TeV-madgraphMLM-pythia8	0.002
WWTo1L1Nu2Q_13TeV_amcatnloFXFX_madspin_pythia8	50.00
WZ_13TeV_amcatnloFXFX_madspin_pythia8	47.13
ZZTo2Q2Nu_13TeV_amcatnloFXFX_madspin_pythia8	4.040
ZZTo2L2Q_13TeV_amcatnloFXFX_madspin_pythia8	3.220
WWZ_TuneCUETP8M1_13TeV-amcatnlo-pythia8	0.165
WZZ_TuneCUETP8M1_13TeV-amcatnlo-pythia8	0.056
ZZZ_TuneCUETP8M1_13TeV-amcatnlo-pythia8	0.014
TTZToLLNuNu_M-10_TuneCUETP8M1_13TeV-amcatnlo-pythia8	0.253
TTZToQQ_TuneCUETP8M1_13TeV-amcatnlo-pythia8	0.530
TTWJetsToLNu_TuneCUETP8M1_13TeV-amcatnloFXFX-madspin-pythia8	0.204
TTWJetsToQQ_TuneCUETP8M1_13TeV-amcatnloFXFX-madspin-pythia8	0.403
TTGJets_TuneCUETP8M1_13TeV-amcatnloFXFX-madspin-pythia8	3.697
TTTT_TuneCUETP8M2T4_13TeV-amcatnlo-pythia8	0.009

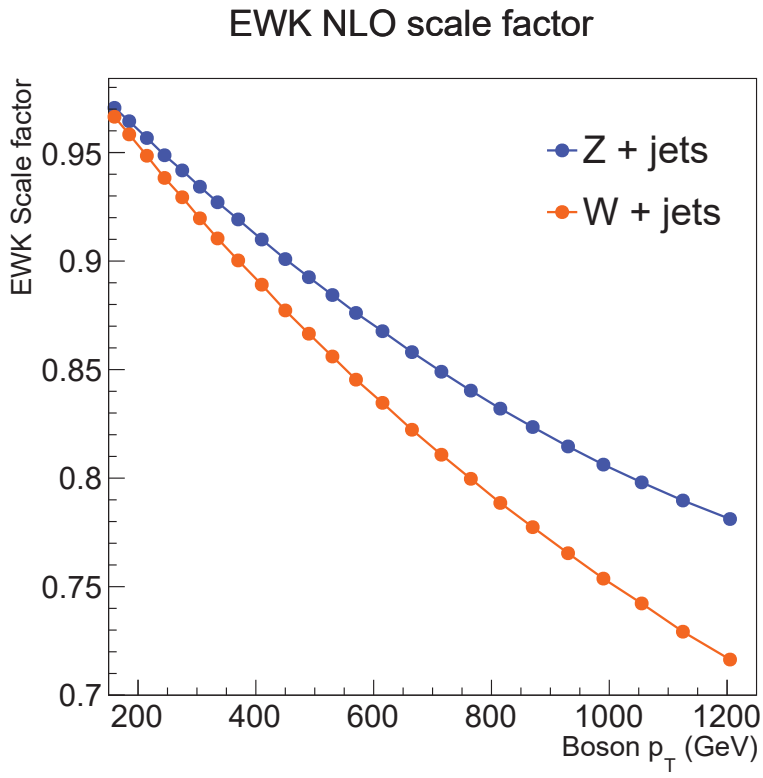

Figure 5.1. EWK NLO scale factors as a function of boson p_T.

were reconstructed making consistent with the data taking conditions for each year.

The list of signal samples used in the analysis can be found in Table 5.3. The NLO QCD predicted cross section of G_{Bulk} with $\tilde{k} = 0.1$ is listed at the link [2], while the LO Cross Section of HVT signal can be found with the link [3]. Both sets of samples are produced with the narrow width assumption (resonance width much smaller than resolution). For the Bulk Gravtion case, the cross section for $\tilde{k} = 0.5$ is calculated using $\sigma_{0.5} = (0.5/0.1)^2 * \sigma_{0.1}$ [75]. The resonance mass considered in this analysis ranges from 1 TeV to 4.5 TeV.

[2]https://github.com/CrossSectionsLHC/WED/blob/master/KKGraviton_Bulk
[3]https://github.com/jngadiub/Cross_Sections_HVT/blob/master/13TeV.txt

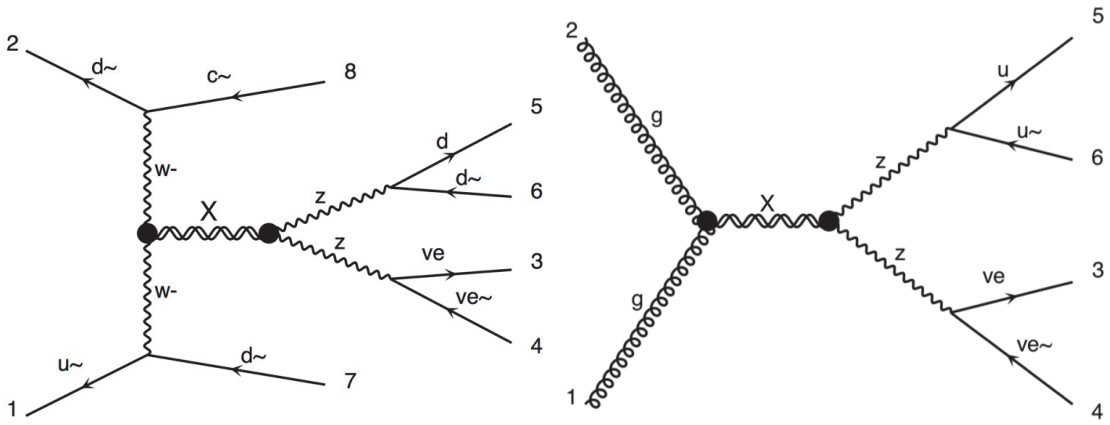

Figure 5.2. Feynman diagrams for the production of resonance (X) through the vector boson fusion (left) and gluon-gluon fusion (right) processes.

Table 5.3. Signal samples list

Year	Sample
VBF	VBF_RadionToZZ_narrow_M-*_13TeV-madgraph
	VBF_WprimeToWZinclusive_narrow_M-*_13TeV-madgraph-pythia8
	VBF_BulkGravToZZinclusive_narrow_M-*_13TeV-madgraph-pythia8
ggF	RadionToZZ_narrow_M-*_13TeV-madgraph
	WprimeToWZToWhadZinv_narrow_M-*_13TeV-madgraph
	BulkGravToZZToZhadZinv_narrow_M-*_13TeV-madgraph

5.3 Signal characteristics

In this dissertation, we are searching signatures of resonances with various spins (spin 0: Radion, spin 1: W', and spin 2: Bulk Graviton). We consider two different production modes, i.e., gluon-gluon-fusion (ggF) and Weak vector-boson-fusion (VBF) as seen in figure 5.2. Regardless of spin, the resonance decays to a pair of SM bosons, i.e., WZ or ZZ where one Z decays to a pair of neutrinos and the other Z or the W decays hadronically. Hadronic decaying bosons are reconstructed as AK8 jets (see Section 4.3, 4.3.1). The neutrinos are identified by p_T^{miss}.

Traditionally resonance searches that employ only the "bump-hunt" method are not very sensitive to the Lorentz structure of the production or decay of a resonance. However, this search, and other partially reconstructed final states, stands

out as an exception to this rule of thumb. In this section, we will focus on the phenomenological consequences of spin correlations on mass reconstruction for the various signal models we are considering. The spin of a resonance is encoded in the angular distribution of its final-state products. For example, for spin-zero particles or unpolarized particles, the polar angle between the production axis (the direction of the initial-state quarks or gluons) and the direct decay products of the resonant particle (in this case weak vector bosons) will be a uniform distribution. In contrast, polarized spin-1, spin-2, etc. particles will produce non-trivial distributions, as demonstrate for ggF production of various resonances in [41] whose definitions we will make slight use of here. While the polar production angle's, $\cos\theta^*$, distribution can be calculated from first principles for a given resonance hypothesis, see Figure 5.3 for examples, the calculation of the observed $\cos\theta^*$ requires knowledge of the boost of VV system, which can't be calculated for partially reconstructed final-states. As a result, in this section, we will present distributions of reconstructable observables to highlight the relevant kinematic manifestations of spin correlations. Two key observables that are correlated to $\cos\theta^*$ are the pseudorapidity of the leading AK8 jet, η_1, and p_T^{miss}. The former will tend to be more central for flat $\cos\theta^*$ distributions or distributions which peak at $\cos\theta^* = 0$ and peak more towards higher η when $\cos\theta^*$ has higher probabilities at ± 1.

The distribution of η_1 is shown in the top row of figure 5.4. We see a significant difference in the distribution for the ggF vs VBF production mode. For ggF the distribution is centrally peaked regardless of the spin whereas, for VBF, we see the different features for spin 1 (double peak: slightly towards forward region) and spin 2 (three peaks: one central and two at slightly forward region). These differences are due to the different Lorentz structures involved in the production and decay of the various hypotheses. In the case of ggF, gluons tend to be more transversely polarized. For the VBF case, the massive vector bosons tend to be longitudinally [32, 75] polarized at high energies. This gives a different differential cross-section for each production and spin hypothesis.

Similar to η_1, the pseudorapidity of the invisible Z-boson, η_2, can be strongly affected by the production mechanism and the spin of the resonance. Although we don't measure η_2, the multi-mode feature of η_1 is also present in η_2 and translates to

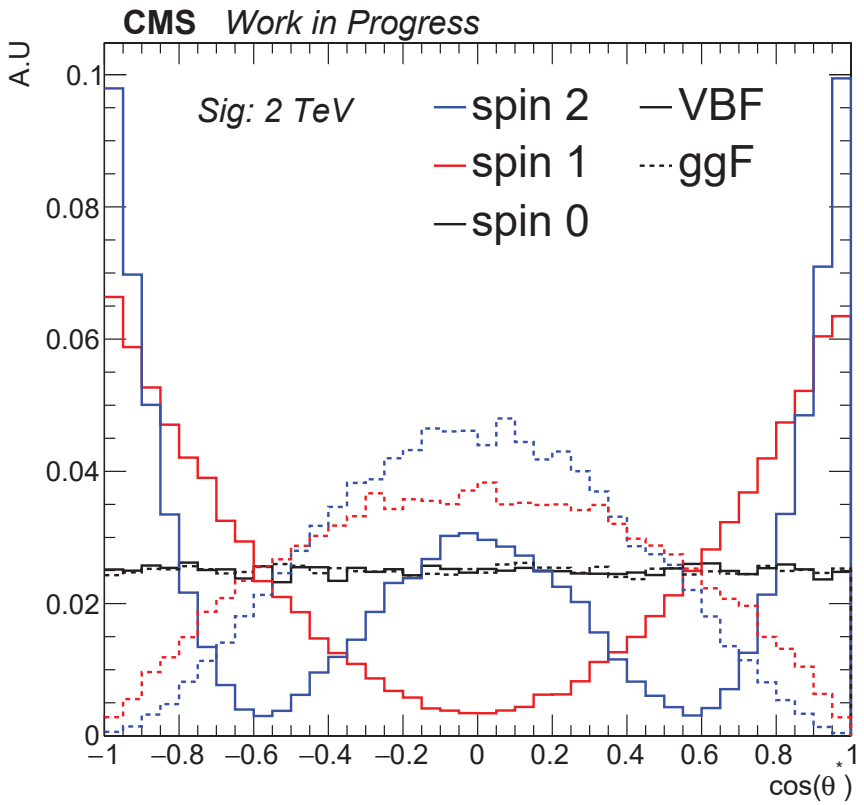

Figure 5.3. Distribution of the production polar angle for various VBF (solid line) and ggF-produced (dashed line) resonances decaying to WZ/ZZ bosons.

a lower (missing) transverse momentum. As such, the p_T^{miss} distributions in Figure 5.4 also have distinctly different shapes which can be bi-modal or just very broad bumps. This feature is also present in the leading AK8 jet p_T distribution. In turn, since we will use both p_T^{miss} and $\text{p}_{\text{T}\ J1}$ to compute the transverse mass of the resonance hypothesis, m_T, the same structures are present in m_T as well. Details of this in the context of the spin 2 case can be found with the link [4].

The shape of m_T in the case of ggF production is the expected jacobian shape, whereas, in the case of VBF, spin-2 and spin-1 have more complicated features. To strengthen this point, Figure 5.5 shows 2-dimensional distributions of m_T versus η_1.

[4] https://indico.cern.ch/event/661188/contributions/2700587/attachments/1513231/2360529/B2GDiB_VBF_Gen_Summary.pdf

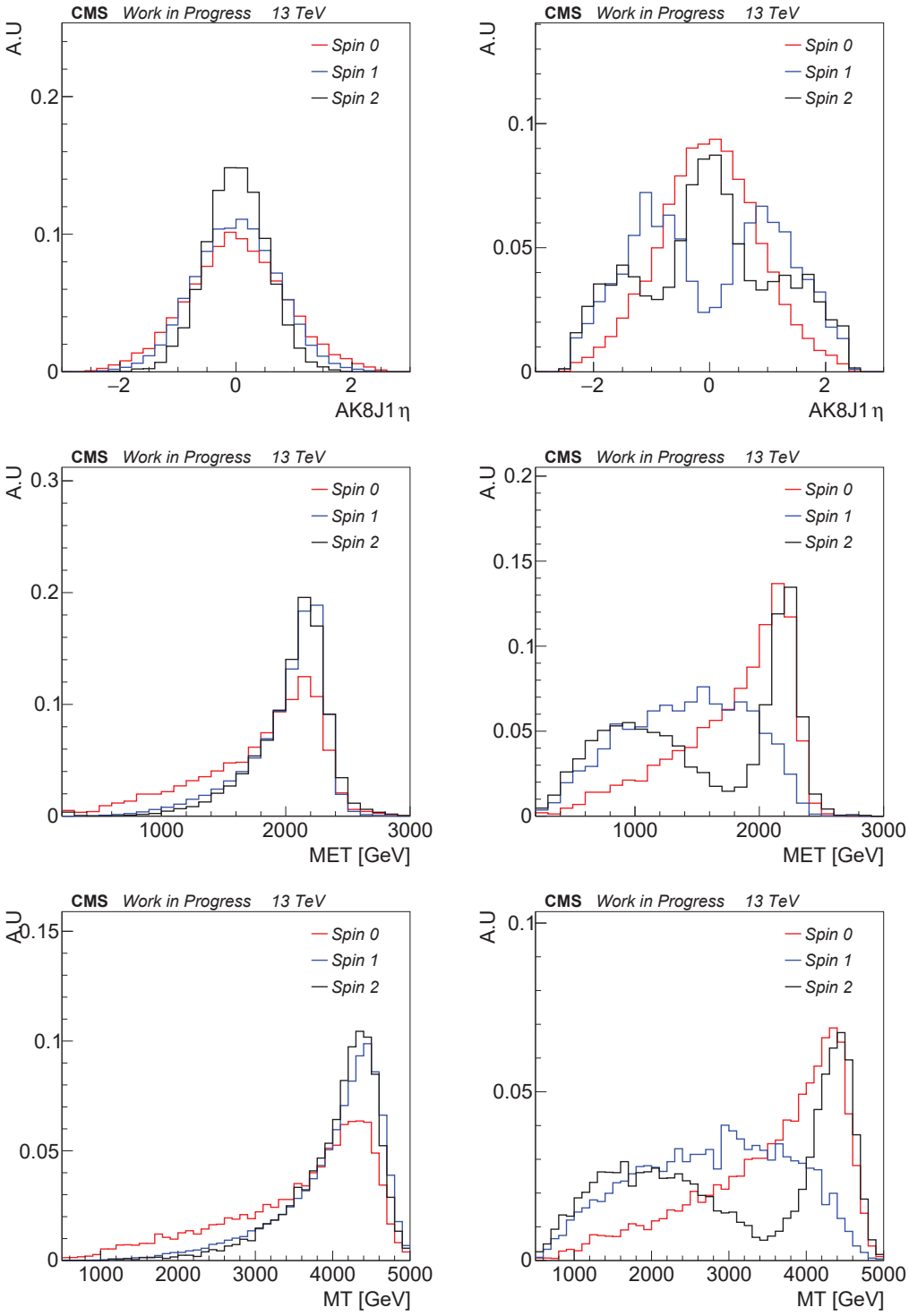

Figure 5.4. Kinematics variable for spin 0, 1, and 2 signal sample. From top to bottom: AK8 Leading jet η, missing transverse energy (p_T^{miss}), and transverse mass (m_T) Left: for ggF production mode, right: for VBF production mode. All signal models have a mass of 4.5 TeV.

For all signal models considered here, vectors bosons which are produced in the forward region typically have lower m_T.

The contrasting features in the leading AK8 jet η distribution for ggF- and VBF- produced signals is a distinct challenge for this analysis. The strong dependence of VBF-produced resonances on their spin is one of the key aspects of this analysis, i.e., to explore the new physics scenarios which manifest themselves not just a traditional bump-like feature from a jacobian peak, but with more complicated shapes that encode the polarization of the resonance itself. Ultimately, these features arise from physics objects being reconstructed in the forward region, a challenging and often overlooked area of the detector when p_T^{miss} is a key kinematic variable.

5.4 Event categorization

Through this section and future sections, plots showing stacked background distributions with signal distributions overlaid onto the plot will be shown to demonstrate the distinct kinematic features of signal, background, and data. In all plots, backgrounds are normalized to the luminosity written above the plot and signal is scaled to luminosity assuming a 1 pb cross-section.

In this analysis we categorize the events making selections (cuts) on various objects discussed in Chapter 4 as follows:

- Baseline selection:
  - Trigger selection (data only)
  - $p_T^{\text{miss}} > 200$ GeV, PFMET/CaloMET > 5.
  - AK8 leading jet $p_T > 200$ GeV, $|\eta| < 2.5$, $CHF > 0.05$ and $NEMF < 0.9$.
  - veto: μ, e, γ ($p_T > 100$ GeV), b-jet, isolated tracks
  - Angular cut: $\Delta\phi(jet, p_T^{\text{miss}}) > 0.5$

Plots for the baseline category are shown in Figure 5.6- 5.8.

- AK8 jet mass: On top of the baseline selections the samples are splitted based on the AK8 leading jet mass, shown in Figure 5.6 (right) after baseline selections:

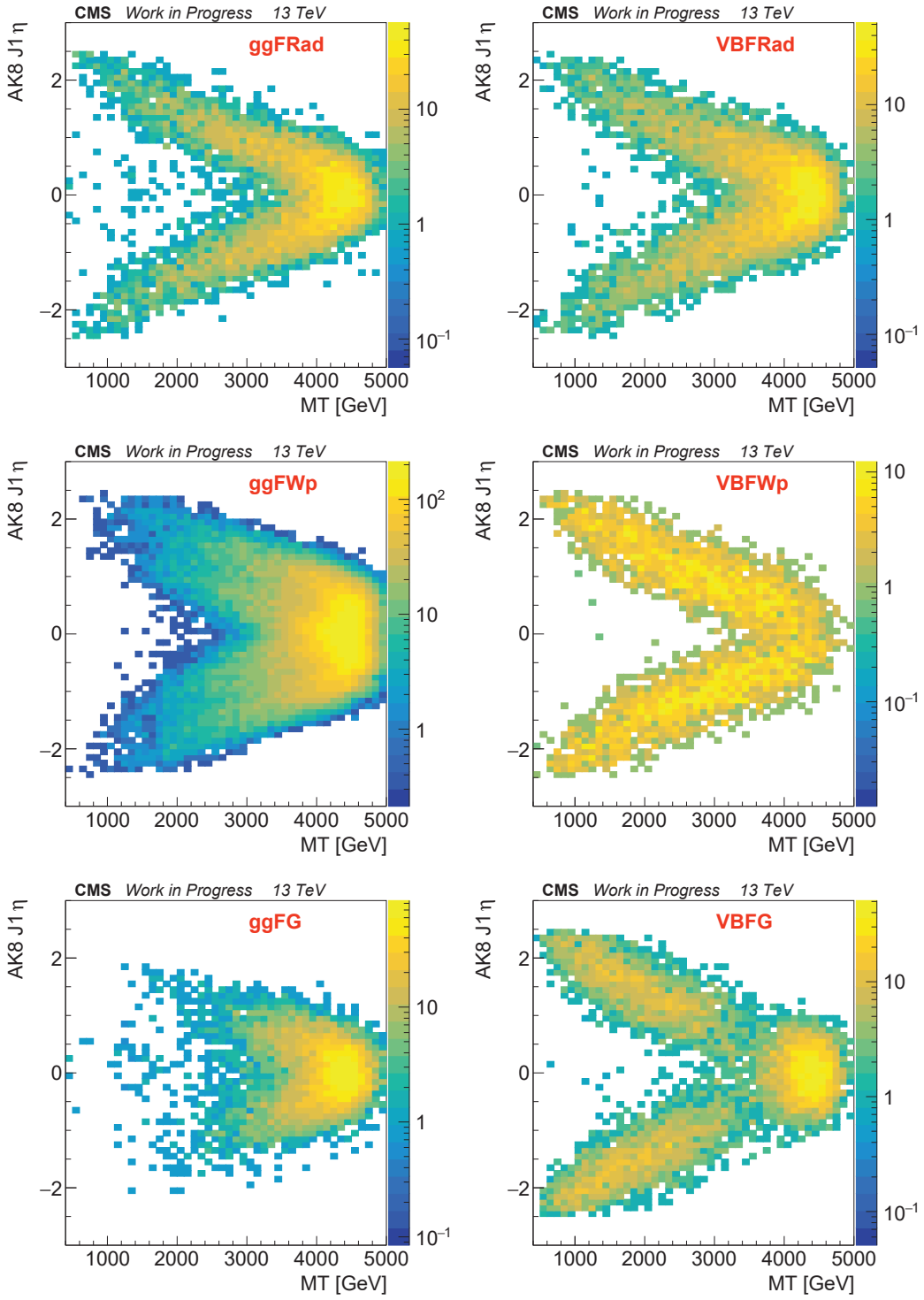

Figure 5.5. Distribution for AK8 leading jet η vs m_T. From top to bottom: spin 0, 1, and 2 sample. Left: for ggF production mode, right: for VBF production mode. All signal models have a mass of 4.5 TeV

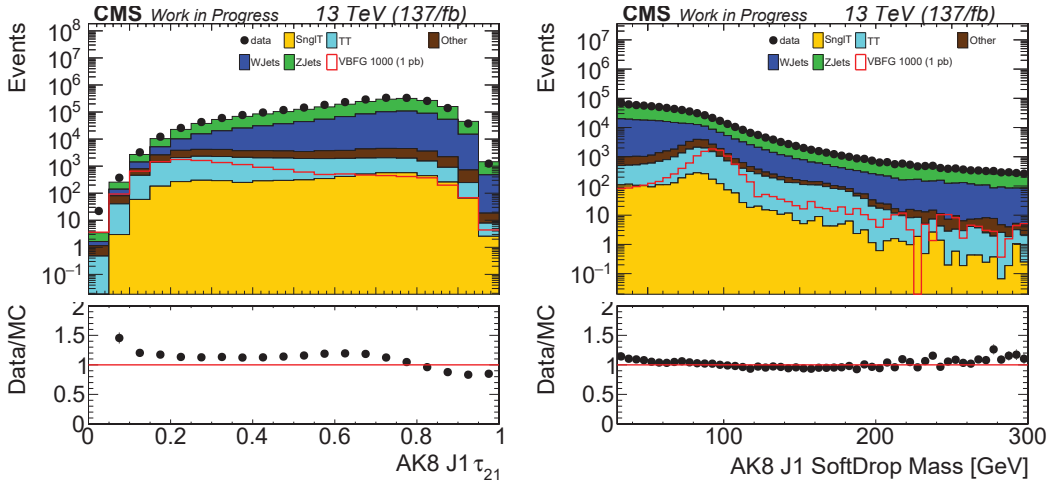

Figure 5.6. Distributions for AK8 Leading jet (Puppi) τ_{21} (left) and soft-drop mass (right) with baseline selection.

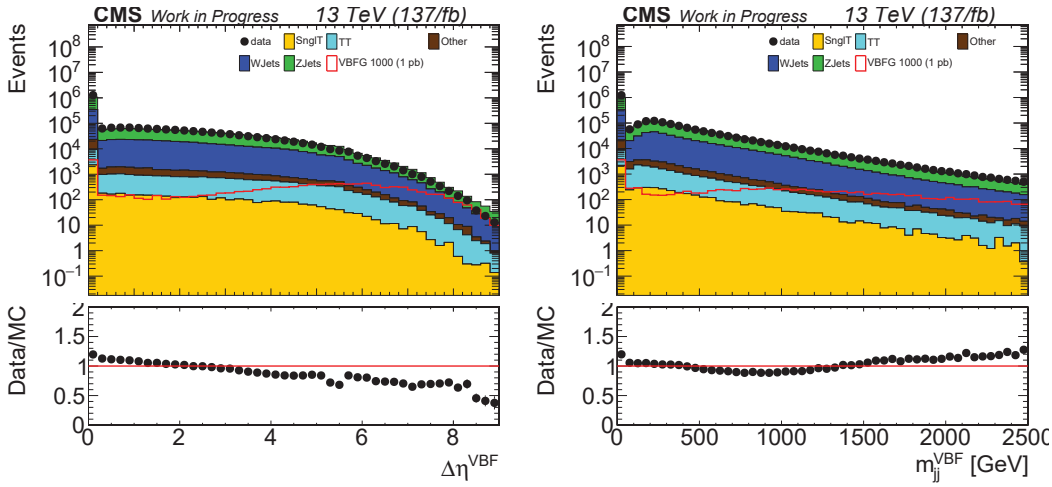

Figure 5.7. Distributions for forward jets $\Delta\eta$ (left) and the dijet mass (right) with baseline selection.

- Signal region (SR): $65 < m_J < 105$ GeV
- Sideband or control region (SB): $30 < m_J < 65$ or $135 < m_J < 300$ GeV

We used the m_J distribution to categorize the signal region and the control (sideband) region. We see that the top ($t\bar{t}$ and single top), diboson, and other rare events (diboson and other rare processes are labeled as other in all plots) peak around the W mass,

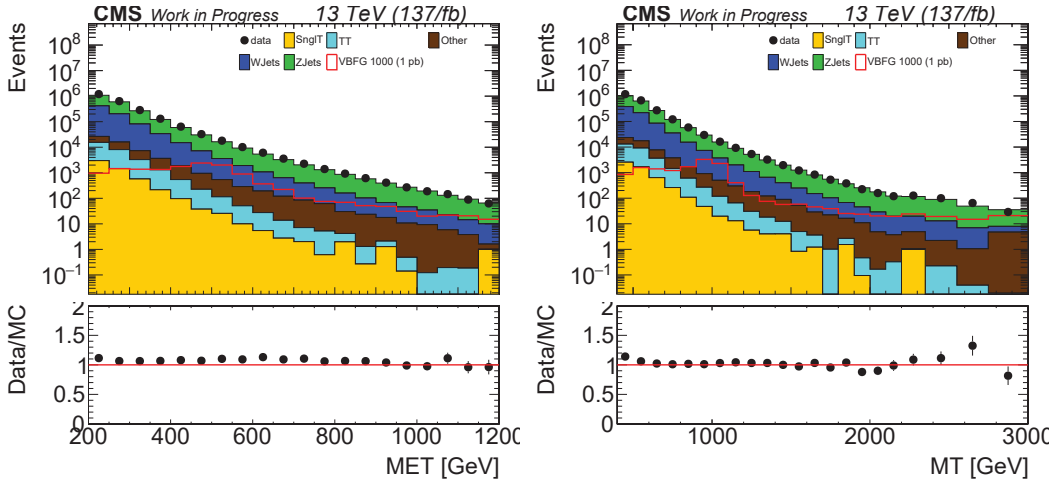

Figure 5.8. Distributions for missing energy (left) and the transverse mass (right) with baseline selection.

which we collectively call the resonant backgrounds. The Z+jets and W+jets don't show this peak feature because the W and Z bosons produced typically decay to one or more neutrinos in order to satisfy the p_T^{miss} requirement; such backgrounds are referred to as non-resonant backgrounds. In this analysis, non-resonant backgrounds are the dominant background and the resonant backgrounds are rare backgrounds. The primary handle for estimating the non-resonant background in the signal region is m_{J} (see Section 5.5). Plots for the SB and SR selection applied on top of the baseline selection are shown in Figures 5.9-5.10. Overlap with $H \to b\bar{b}$ is avoided by excluding the mass window of $105 < m_J < 135$GeV. Where SR and SB regions are referred to, they are always referring to baseline plus SR and baseline plus SB selections, respectively.

- Hadronic V-tagging: The events are splitted based on the value of the τ_{21} discriminant, shown in Figure 5.6 (left) after baseline selections:
  - High Purity (HP): $\tau_{21} < 0.35$
  - Low Purity (LP): $0.35 < \tau_{21} < 0.75$

As seen in Figure 5.6 (left), the dominant background peaks towards the higher value

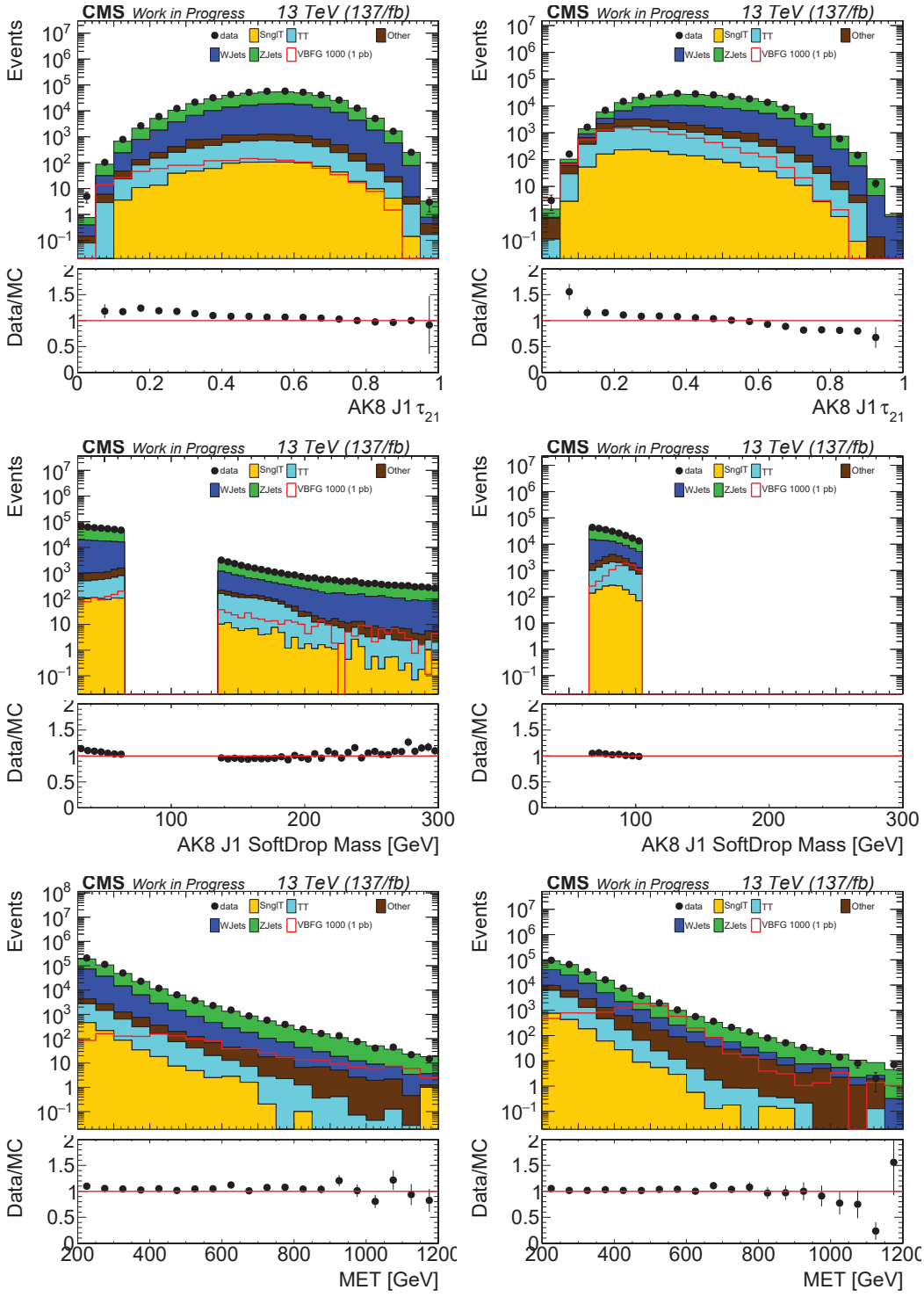

Figure 5.9. Distributions for AK8 Leading jet τ_{21} (top), mass (middle), and missing energy (bottom) with SB (left) and SR (right) selection.

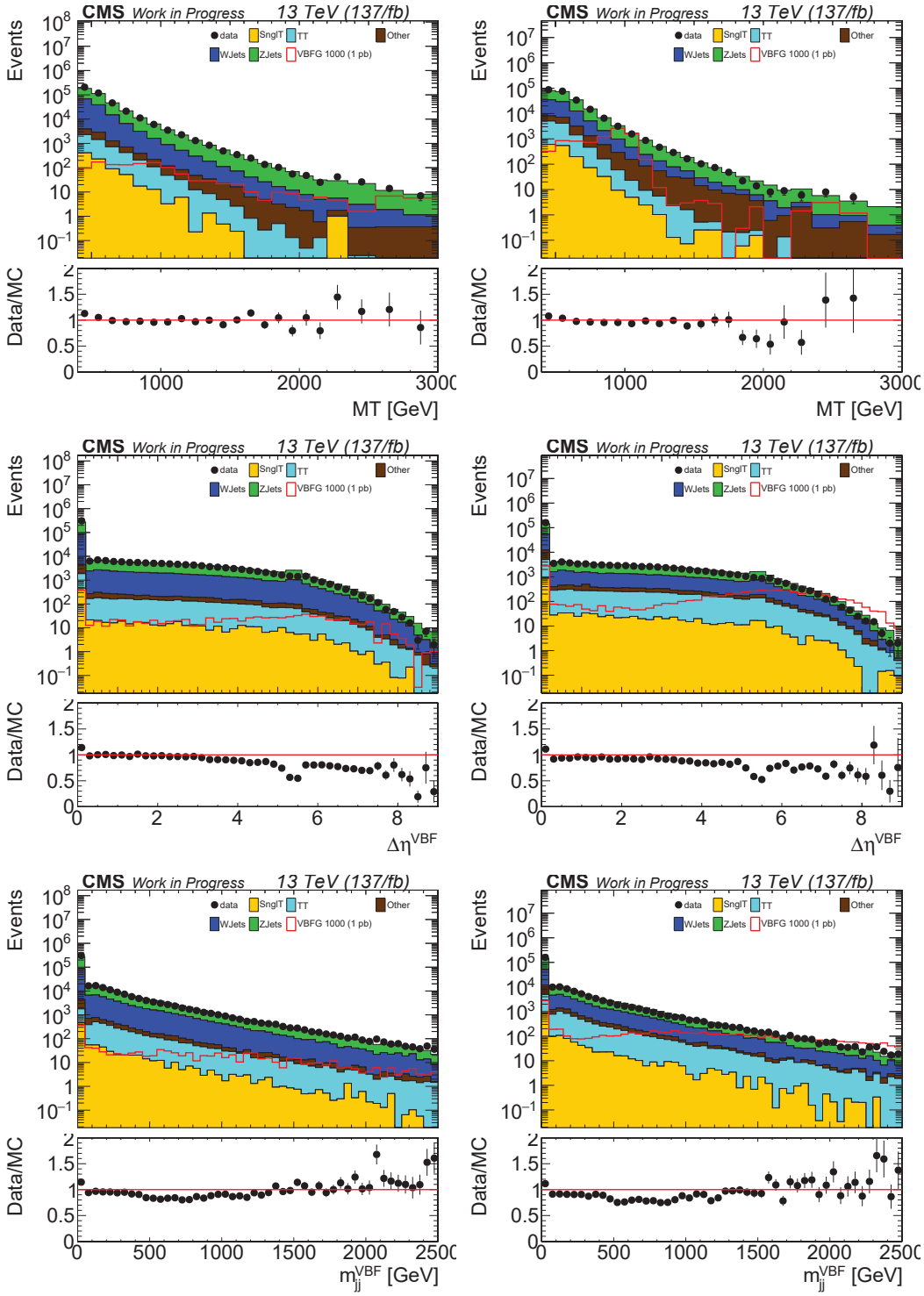

Figure 5.10. Distributions for transverse mass (top), forward jets $\Delta\eta$ (middle), and forward dijet mass (bottom) with SB (left) and SR (right) selection.

of τ_{21} discriminant whereas the signal peaks at the lower value. Hence, the HP and LP as mentioned above are defined based on the signal-dominant region.

- VBF and VBFfail selection: Lastly, we split data into two samples to isolate VBF and ggF processes and the key objects used for the selection are shown in Figure 5.7:

  - VBF: events that passed the VBF selection (see Section 4.3.3).
  - VBFfail: events failing the VBF selection.

  The VBF selections tag signal events by identifying peripheral jets in the forward region, a by-product of the VBF process.

The distributions of the main search variable i.e. transverse mass (m_T) after each selections are shown in Figures 5.11- 5.12. The distributions in the SB region for each category shows the good agreement between data and simulations.

The signal efficiency with the final selections in both high and low purity cateogory for each signal type (ggF or VBF) is shown in Figure 5.13. The various background compositions in each region/category are shown in Figure 5.14

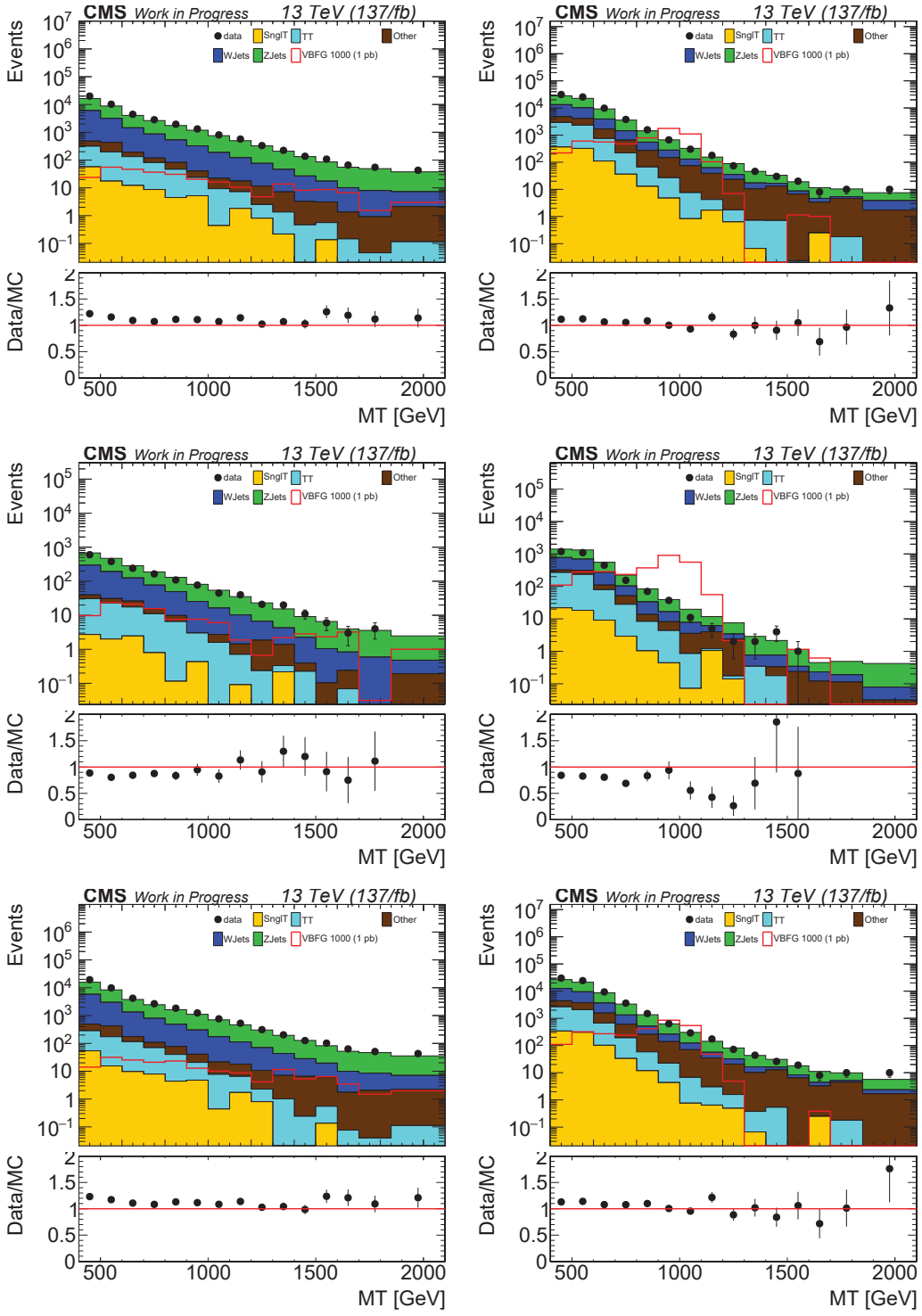

Figure 5.11. Distributions for transverse mass with SB (left) and SR (right) selection and high purity (top), VBF (middle), and VBF-fail (bottom).

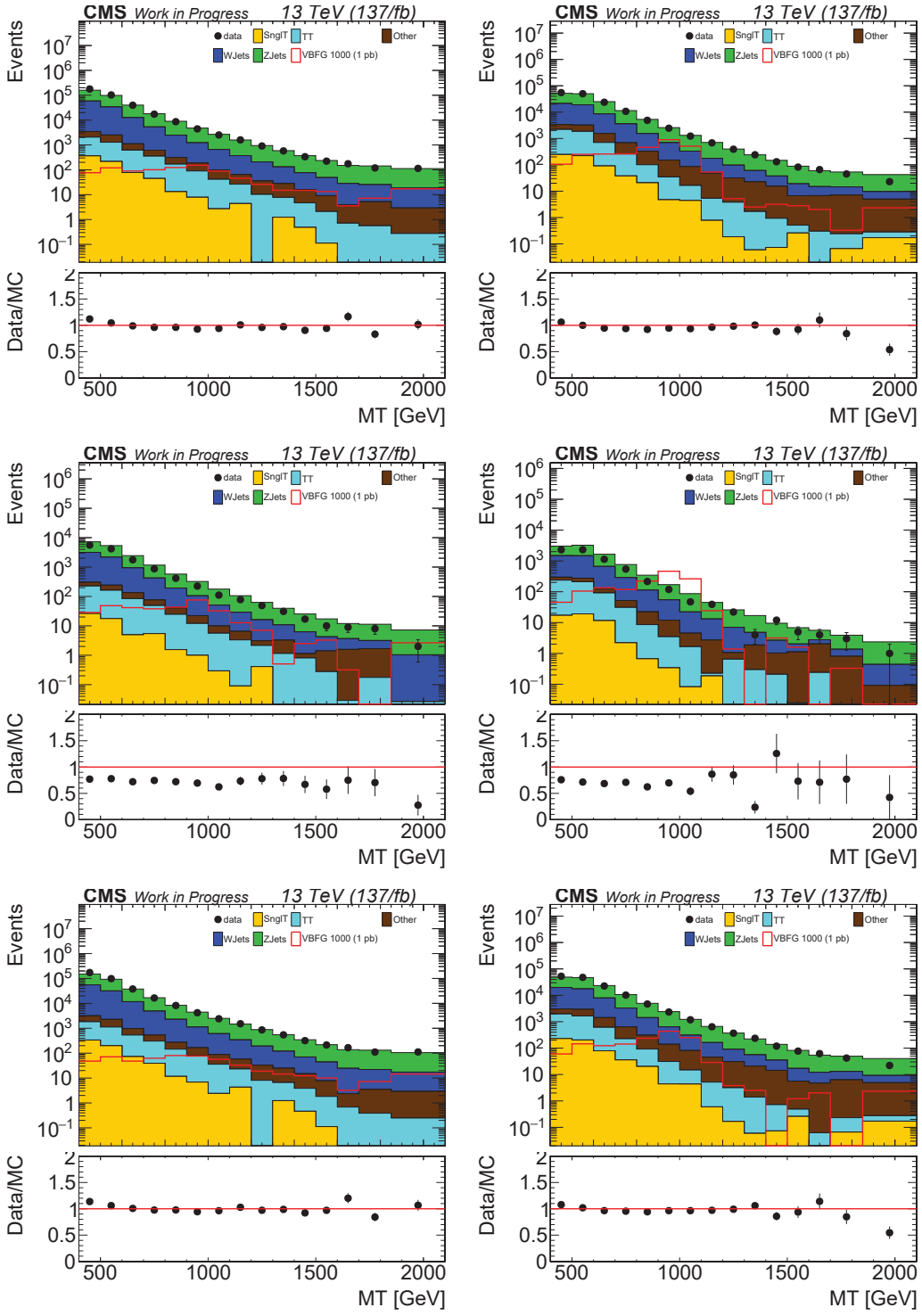

Figure 5.12. Distributions for transverse mass with SB (left) and SR (right) selection and low purity (top), VBF (middle), and VBF-fail (bottom).

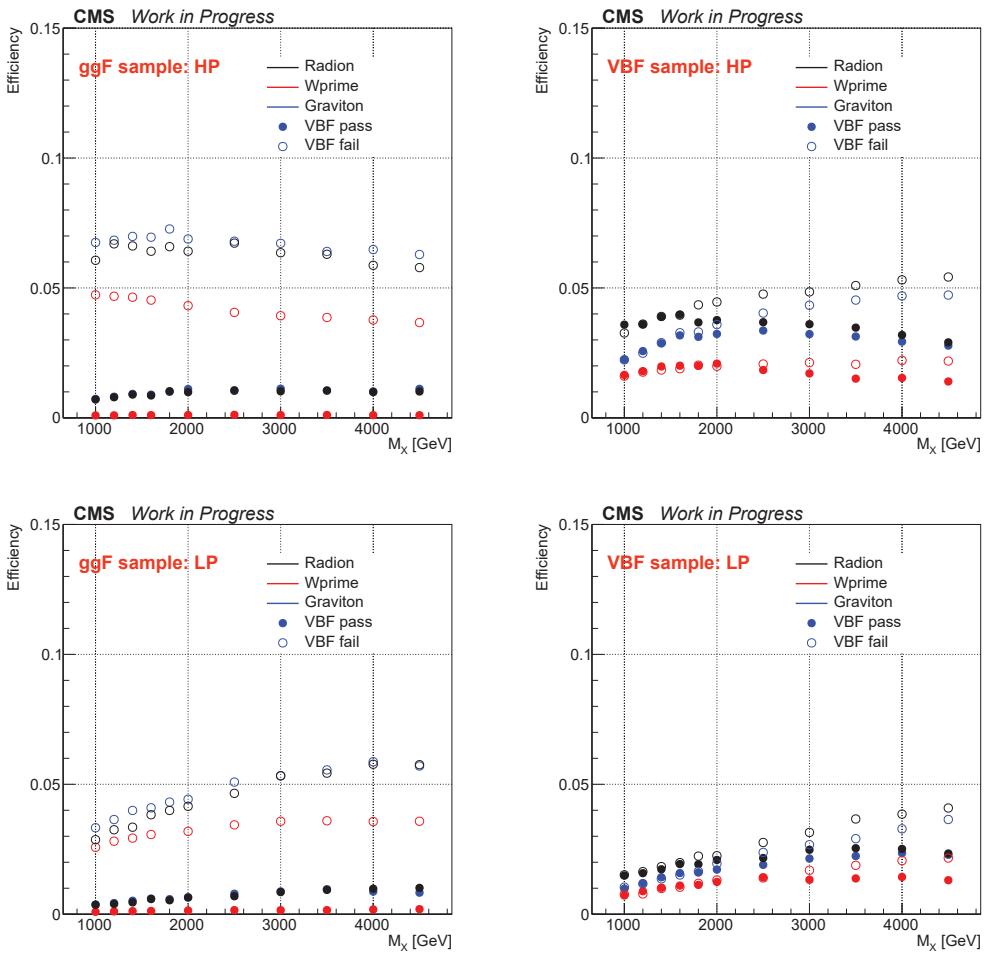

Figure 5.13. Signal acceptance for various mass points for spin 0, 1, and 2 sample in high (top) and low (bottom) purity category. Left: For ggF sample, right: For VBF sample

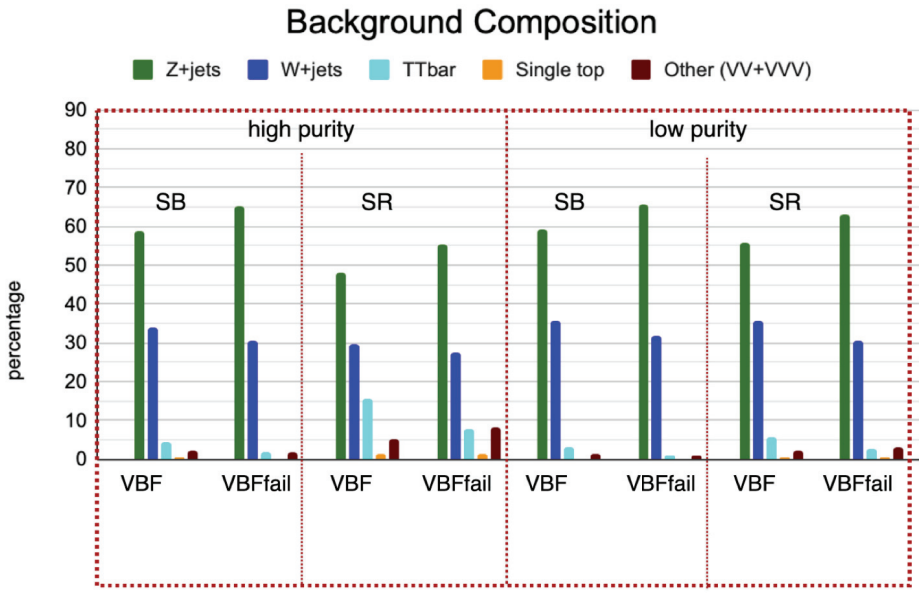

Figure 5.14. The SM background compositions in various regions/categories.

5.5 SM background estimation

As mentioned in 5.4, AK8 leading jet mass is used to distinguish the signal (SR) and control (SB) region in this analysis. A schematic of this is shown in figure 5.15. Also shown is the type of background i.e. one with resonant shape (mass peak) and the other without such peak in the m_J spectrum. Figure 5.14 shows the composition of the two background components in the various signal and control regions. The resonant backgrounds used in this analysis are top (single, and $t\bar{t}$), diboson, and other rare processes whereas the non-resonant backgrounds comprise Z($\nu\nu$)+jets and W(lν)+jets i.e. V+jets. The resonant background is sub-dominant (rare) in this analysis hence, they are taken from their signal region yields with the appropriate systematics listed in 5.6. The non-resonant or dominant backgrounds however are estimated using a data-driven method with some input from the monte-carlo.

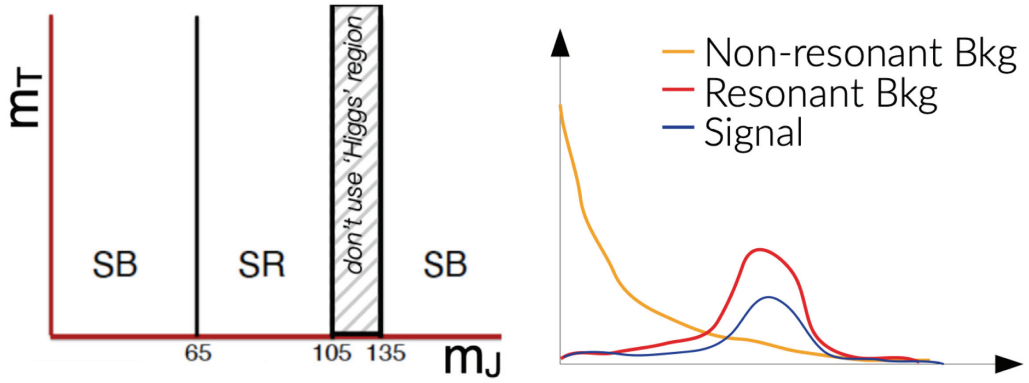

Figure 5.15. Schematics of the categorization of the signal and control region (left) and the type of backgrounds (right).

The procedure of estimating the non-resonant background in the SR is commonly called 'Alpha method' which is performed in the following way: The event yields which were derived separately for each category are shown in figure 5.16- 5.17. Different binnings were used in different regions.

- A transfer factor (α) as a function of m_T is calculated taking the ratio of the yields of V+jets backgrounds in SR to SB as shown in the equation 5.1. The distribution of alpha for various categories (high purity, low purity, VBF-pass,

and VBF-fail) are shown in figure 5.18.

$$\alpha = \left(\frac{N^{SR}}{N^{SB}}\right)^{V+jets} \tag{5.1}$$

The systematic change in the slope of the m_T spectrum due to the m_J requirement introduces a bump like shape in the α distribution. For values m_T >900 GeV, α <1.0 for VBF and non-VBF events for high purity category whereas α <1.0 in the whole range for the low purity category.

- Rare background contribution in the SB is subtracted from the Data (observation) in the SB. Then applying α to this gives the estimation of the non-resonant background in the SR region as shown in equation 5.2.

$$N_{\text{pred}}^{\text{non-res}} = \alpha \times (N_{\text{SB}}^{\text{obs}} - N_{\text{SB}}^{\text{res}}) \tag{5.2}$$

- Lastly, adding the contribution of the rare background in the SR gives the total prediction in the SR which is the second part of the equation 5.3. The prediction for various categories are shown in figure 5.25.

$$N_{\text{pred}}^{\text{total}} = N_{\text{SR}}^{\text{res}} + N_{\text{pred}}^{\text{non-res}} \tag{5.3}$$

5.5.1 Alpha method validation

The alpha method was validated in data directly by blinding the signal region and defining a pseudo-SR between $55 < m_T < 65$ GeV, and removing these events from the SB. The new α and the total prediction is calculated in the usual way using equations 5.1- 5.3. The total prediction from the alpha method is now compared with the data events in the pseudo-SR as shown in Figure 5.19. The uncertainties in the top pad are statistical only from the closure validation region whereas the hashed band in the bottom pad is the size of the total uncertainty in the true signal region.

This result validates the alpha method of background estimation in this analysis. Some tensions were observed; however, the chi-square value suggests that the

differences are not significant in all cases except in the LP VBFfail category. To address this, additional shape systematics for the non-closure is introduced in the likelihood which is represented by the slope in the ratio pad in the LP VBFfail category. Also, to gain more confidence, we have performed a few iterations of validation (shown in Figure 5.20) by loosening the following cuts:

- $\tau_{21} < 0.75$: τ_{21} cut was loosen from $\tau_{21} < 0.35$ (high purity (HP)) to 0.75 (full purity (FP)).
- Forward jets $\Delta\eta$ and m_{jj}: $\Delta\eta > 4.0$ was loosened to $\Delta\eta > 3.0$ and $m_{jj} > 500.0$ was loosened to 300.

These additional test further validates our technique for background estimation. All closure tests are consistent within the uncertainties assigned.

5.6 Systematic uncertainties

Systematic uncertainties in our predictions stem from uncertainties mainly due to limited simulation sample size and limited statistics of our data in the control region. Systematics on the shape of α arise from uncertainties that affect the shape of key kinematic distributions. Since resonant backgrounds (also called rare backgrounds) are predicted directly with simulation, both normalization and shape uncertainties are considered. Uncertainties were estimated for the individual years but later combined to 137 fb^{-1} weighted to the luminosity for each year. All the systematic uncertainties (in %) considered in this analysis are summarized in Table 5.4 - Table 5.5.

In most cases, the estimation of the systematics is mostly varying the weight with the systematics provided by the POGs and comparing the variation with respect to the nominal values. This distribution of comparing the variations gives the scale of the systematics and also if it has any shape dependence or not.

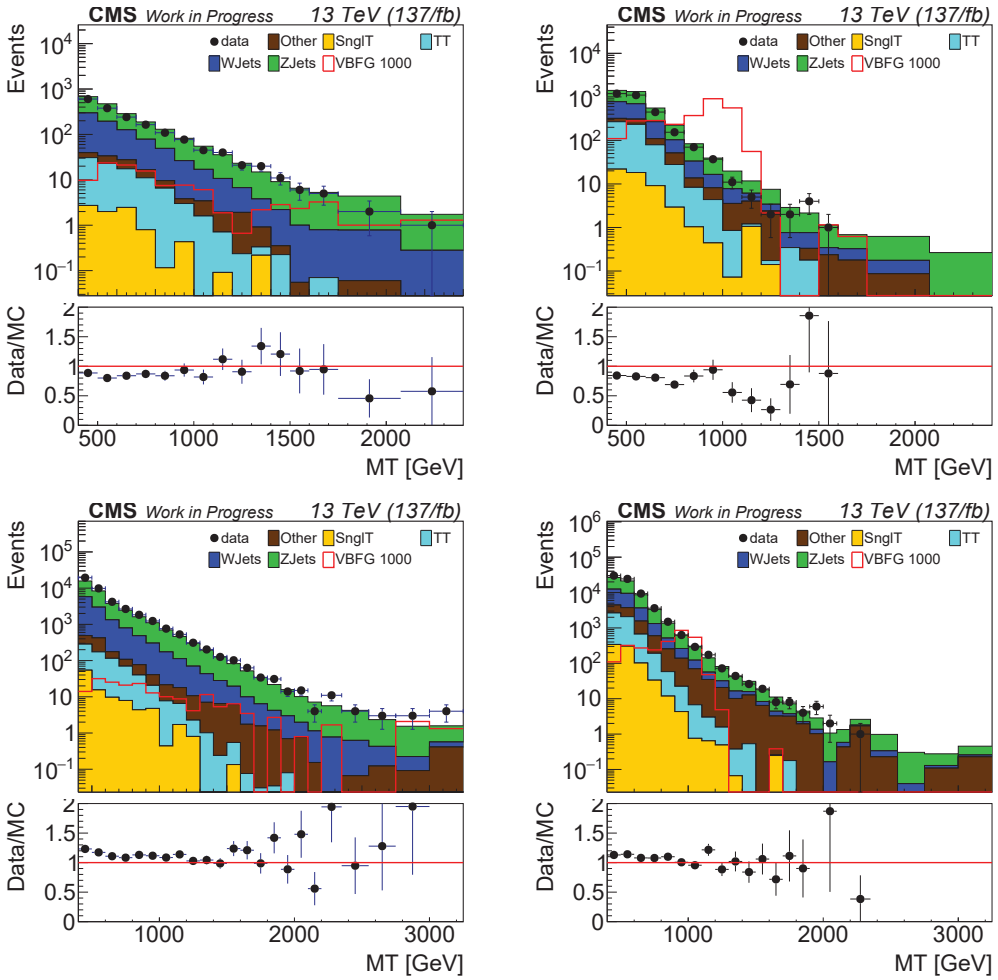

Figure 5.16. Distribution for the search variable m_T for VBF (top) and VBFfail (bottom) category. Last bin corresponds to the overflow bin. Left: High purity side band region, right: High purity signal region

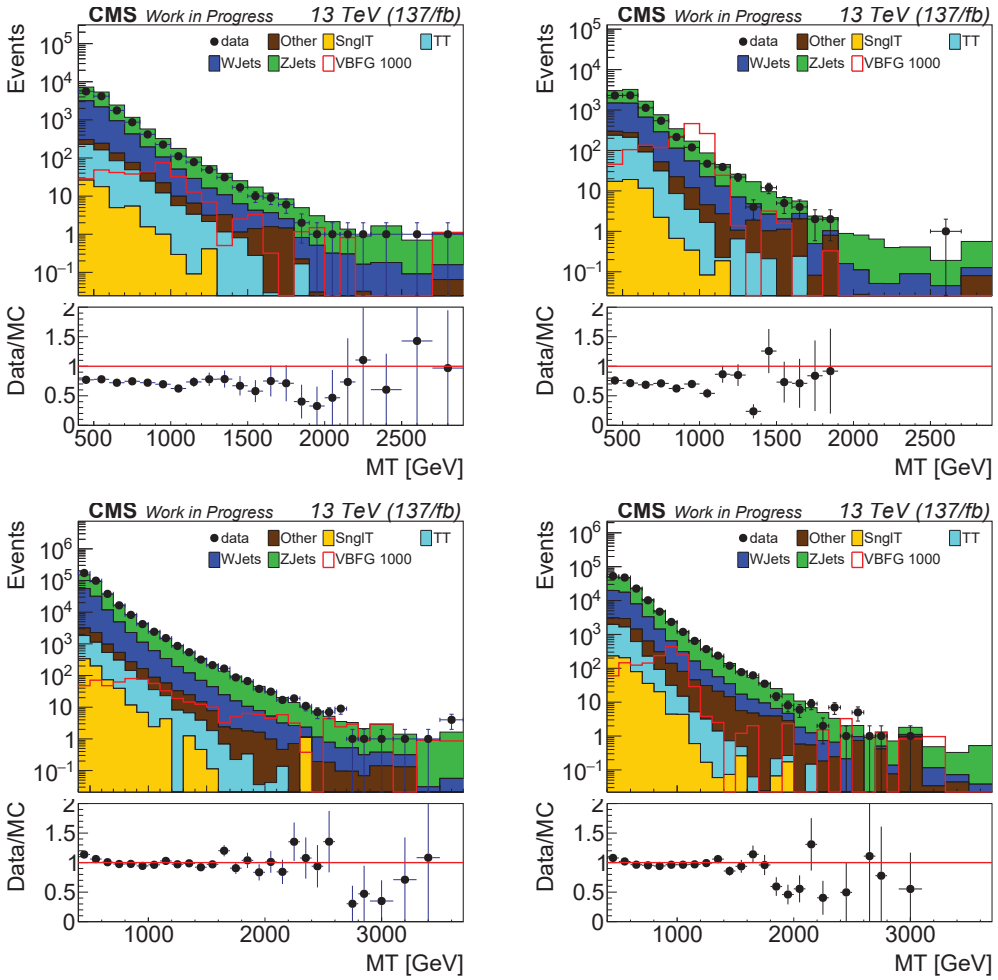

Figure 5.17. Distribution for the search variable m_T for VBF (top) and VBFfail (bottom) category. Last bin corresponds to the overflow bin. Left: Low purity side band region, right: Low purity signal region

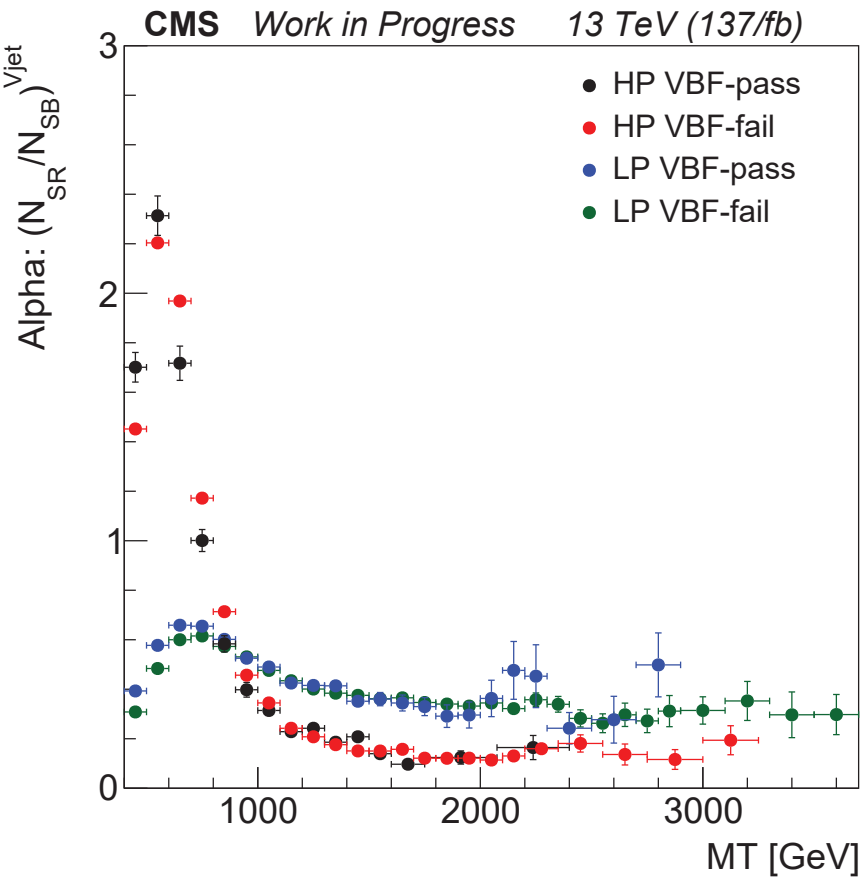

Figure 5.18. Distributions for alpha in various categories. The last bin corresponds to the overflow bin.

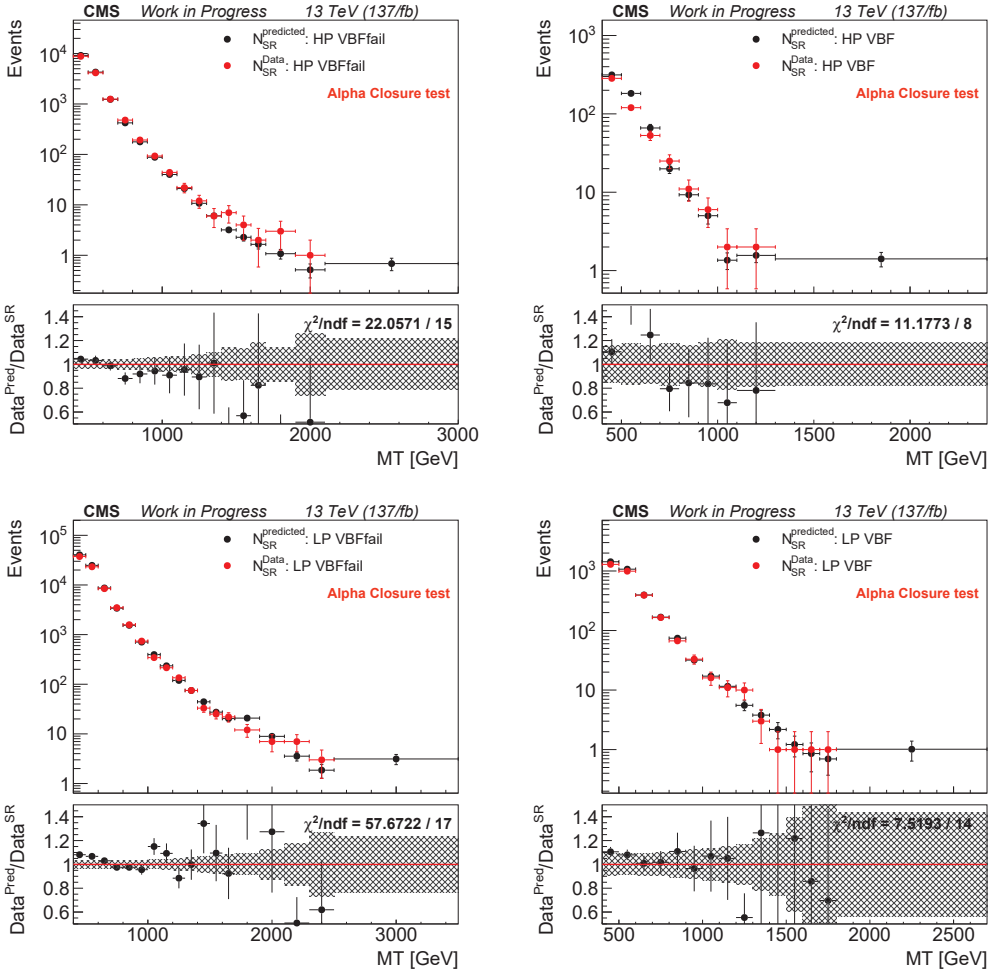

Figure 5.19. Distributions for predicted data in SR in high (top) and low (bottom) purity category. Black and red dots represent the predicted events in SR and the data in the SR (pseudo) respectively. Ratio of prediction in SR to data in SR is shown at the bottom which is ~ 1. Left: For VBF-fail event, right: For VBF-pass event. The hashed region in the ratio panel corresponds to the total uncertainty on the prediction in the true signal region.

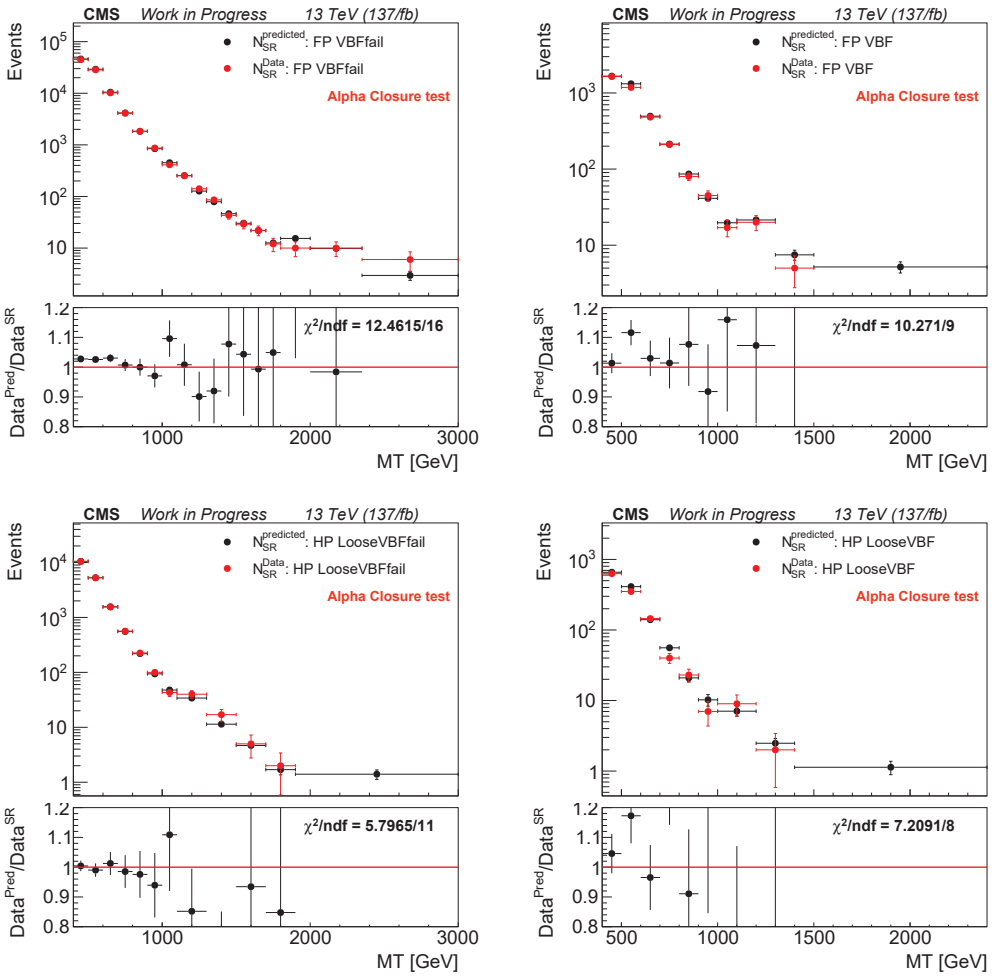

Figure 5.20. Alpha closure test after loosening few selections. From top to bottom: after loosening τ_{21} cut, VBF cuts. Left: for events that failed the VBF selection, right: for events passing VBF selection

Table 5.4. Summary of systematic uncertainties (in %) for α and various regions for resonant background.

Systematics	α_{VBF}	$\alpha_{\mathrm{VBFfail}}$	SRVBF	SBVBF	SRVBFfail	SBVBFfail
Luminosity	-	-	2.4	2.4	2.4	2.4
τ_{21} SF (HP)	-	-	7.3	7.3	7.3	7.3
τ_{21} SF (LP)			17.0	17.0	17.0	17.0
Pileup (HP)	-	-	3.9	2.0	1.0	1.7
Pileup (LP)	-	-	3.9	3.7	0.8	0.9
b jet veto (HP)	-	-	2.4	3.5	1.8	2.8
b jet veto (LP)	-	-	2.9	3.2	2.2	2.6
Prefiring (HP)	-	-	0.7	0.8	0.3	0.4
Prefiring (LP)	-	-	0.6	0.7	0.2	0.3
Unclust. Energy (HP)	-	-	2.4	1.8	1.8	1.6
Unclust. Energy (LP)	-	-	1.6	1.4	1.3	1.5
JMR (HP)	-	-	1.2	5.9	1.7	7.1
JMR (LP)	-	-	1.6	0.7	1.01	0.96
τ_{21} $\mathrm{p_T}$ extrap. (HP)	-	-	2 - 18	2 - 18	2 - 18	2 - 18
τ_{21} $\mathrm{p_T}$ extrap. (LP)	-	-	1 - 10	1 - 10	1 - 10	1 - 10
JMS Up (HP)	-	-	0.3	1.8	0.3	1.6
JMS Down (HP)	-	-	0.5	0.9	0.3	1.2
JMS Up (LP)	-	-	0.4	0.5	0.2	0.4
JMS Down (LP)	-	-	0.4	0.5	0.3	0.4
Trigger Up (HP)	-	-	1.0	0.8	1.1	0.9
Trigger Down (HP)	-	-	1.4	1.4	1.4	1.4
Trigger Up (LP)	-	-	1.0	0.9	1.0	0.9
Trigger Down (LP)	-	-	1.4	1.4	1.4	1.4
JEC	3.0	1 - 2	40 - 13	40 - 13	4.0	4.0
JER	3.0	1.5	35 - 13	35 - 13	2.0	2.0
PDF normalization	-	-	5.0	5.0	2.0	2.0
PDF shape	3.0	1.5	0.5 - 4	0.5 - 4	0.5 - 4	0.5 - 4
μ_R, μ_F scale normalization	-	-	15	15	11	12
μ_R, μ_F scale shape	1 - 2	1 - 2	1 - 10	2 - 4	3 - 8	3 - 4

Table 5.5. Summary of systematic uncertainties (in %) for various regions for signal samples.

Systematics	SRVBF	SBVBF	SRVBFfail	SBVBFfail
Luminosity	2.4	2.4	2.4	2.4
τ_{21} SF (HP)	7.3	7.3	7.3	7.3
τ_{21} SF (LP)	17.0	17.0	17.0	17.0
Pileup (HP)	0.2	0.7	1.1	1.1
Pileup (LP)	0.5	1.0	0.9	0.6
b jet veto (HP)	1.3	1.4	1.3	1.3
b jet veto (LP)	1.4	1.6	1.4	1.5
Prefiring (HP)	1.0	1.0	0.6	0.6
Prefiring (LP)	0.9	1.0	0.5	0.5
Unclust. Energy	0.1	0.1	0.1	0.1
JMR (HP)	3.2	6.9	3.3	7.5
JMR (LP)	2.8	4.0	2.4	3.4
τ_{21} p_T extrap. (HP)	2 - 18	2 - 18	2 - 18	2 - 18
τ_{21} p_T extrap. (LP)	1 - 10	1 - 10	1 - 10	1 - 10
JMS Up (HP)	0.9	2.4	0.7	2.0
JMS Down (HP)	0.7	2.6	0.7	2.4
JMS Up (LP)	0.3	1.6	0.3	1.2
JMS Down (LP)	0.2	1.9	0.2	1.5
Trigger Up (HP)	0.8	0.8	0.8	0.8
Trigger Down (HP)	1.4	1.4	1.4	1.4
Trigger Up (LP)	0.8	0.8	0.8	0.8
Trigger Down (LP)	1.4	1.5	1.6	1.5
JEC	5 - 11	4 - 14	1 - 7	1 - 5
JER	2 - 3	6 - 7	1 - 7	1 - 5

5.7 Statistical tests

In this section, the parameterization of the likelihood used for the statistical interpretations of data is presented.

Statistical interpretations of various signals are modeled with a binned likelihood. The individual bins correspond exactly to those shown in Figure 5.25. For each of the m_T regions, two observed yields are considered, the SR and the SB yields. The likelihood models each m_T independently, with small dependencies control through key systematic uncertainties that are correlated across m_T bins as discussed in Section 5.6. Each m_T bin models six contributions in order to constrain the non-resonant background to the observed SB yields and test for new physics in the SR. The six contributions are:

- The signal yields in the SR.
- The signal yields in the SB: typically small, but accounts for signal contamination.
- The resonant backgrounds in the SR.
- The resonant backgrounds in the SB: accounts for contamination of backgrounds which don't scale according to the α.
- The non-resonant backgrounds in the SR.
- The non-resonant backgrounds in the SB.

The MC based predictions for all of the above contributions are provided to Higgs-combine data cards which are used to construct a likelihood. The central value of the non-resonant background in the SR and SB is fully constrained by imposing a rate parameter to constrain the ratio between expected non-resonant backgrounds in the SR and the SB. There is one rate parameter for each m_T bin. This rate parameter has the effect that the predicted non-resonant SR event yields will typically be constrained by the observed SB event yields, as long as the SB event yields are larger than the SR event yields. Because the resonant background and signal event yields are

modeled in both the SR and the SB portions of the likelihood, these backgrounds are effectively subtracted from both SB before this scaling occurs. An example datacard can be found in Figure 5.28.

The construction of the likelihood was designed to build in the assumptions of our background estimation, namely that the ratio of non-resonant SR and SB event yields are constrained by the predicted ratio in simulation while the expected contamination of resonant backgrounds is accounted for based on predicted yields in MC.

Both shape and normalization of α, and resonant background and signal event yields are modeled in the likelihood with uncertainties and correlations as described in Section 5.6. These uncertainties are represented by nuisance parameters in our likelihood and will be constrained with data through a fit of the background-only model to data. Currently, since we have not looked at the observed event yields in our SR, all results shown are without such constraints.

To test the validity of our likelihood we have performed the following tests: Goodness-of-fit test, signal injection test using asimov datasets, signal injection tests using ensembles of generated toys.

A goodness-of-fit test is performed to quantify how well our model of the SM backgrounds agree with observations in our control regions. For this test, we exclude the signal regions, which are still blinded. We use the so-called saturated model for constructing the test statistic. The test statistic is calculated for the data and an ensemble of pseudo-datasets generated based on our model of the backgrounds. The distribution of the test statistic the ensemble of toys and the measured test statistic for the observed dataset are shown in Figure 5.21. We find that the observed dataset is statistically compatible with our model and has a p-value of 0.787.

Signal injection tests are performed in two separate ways. In one method, we inject a signal into the asimov dataset and measure the best-fit signal strength using a maximum-likelihood fit. The second test involves generating random toy datasets based on our model of the signal and backgrounds; each pseudo-dataset is then fit using a maximum likelihood fit to extract r and its uncertainties. These values are used to understand the ensemble effects of our likelihood model and whether there

Table 5.6. Signal injection test with using maximum likelihood fits to asimov datasets. The signal strength injected corresponds to three times the expected 95% CL upper limit on the production cross section for that model using the combined (VBF pass and VBF fail) category.

sample	1 TeV ($r_{injected}/r$)	2 TeV ($r_{injected}/r$)	4 TeV ($r_{injected}/r$)
VBF Radion	$1.000 \quad -0.217/+0.252$	$0.995 \quad -0.282/+0.345$	$0.993 \quad -0.327/+0.441$
VBF Wprime	$0.999 \quad -0.217/+0.249$	$0.996 \quad -0.272/+0.327$	$0.990 \quad -0.317/+0.415$
VBF Graviton	$1.001 \quad -0.220/+0.258$	$0.994 \quad -0.291/+0.361$	$0.991 \quad -0.324/+0.431$
ggF Radion	$1.001 \quad -0.206/+0.234$	$0.997 \quad -0.262/+0.320$	$0.996 \quad -0.324/+0.438$
ggF Wprime	$1.002 \quad -0.202/+0.228$	$0.999 \quad -0.265/+0.322$	$0.999 \quad -0.332/+0.446$
ggF Graviton	$1.002 \quad -0.202/+0.227$	$0.997 \quad -0.264/+0.321$	$0.996 \quad -0.328/+0.438$

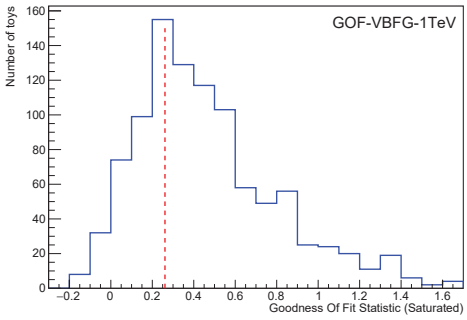

Figure 5.21. Distribution of the goodness-of-fit test statistic for an ensemble of pseudo datasets sampled from our model of the SM backgrounds and the observed test statistic of the observed control region.

are any worrisome biases. In each signal injection test, we inject a varying amount of signal, based on the sensitivity of our analysis for constraining the signal strength. Typically, we inject three times the expected 95% CL upper limit on the production cross-section. Table 5.6 shows the ratio of the injected signal strength divided by the best-fit value of r as extracted from fits to asimov datasets. Figure 5.22- 5.24 shows the distribution of the best-fit r as extracted from pseudo-datasets and the distribution of the pull. The pull is defined as $(\hat{r} - r_{inj})/\delta r$, where $\hat{r}$ is the fitted value, r_{inj} is the average signal injected into each toy, and δr is the uncertainty on $\hat{r}$. We find that test with asimov datasets show no bias in the fitted signal strength. Toys studies largely show that our modeling of the signal and background work reasonably well. There are signs that a statistically significant bias is present in the pull distributions. However, this seems to largely be due to a bias in the measured uncertainties. The distributions of the fitted signal strength show that the bias in such a measurement would only be at the level of a few percent, even in cases where the pull shows a statistically significant effect. We believe these results are sufficient validation for our use case.

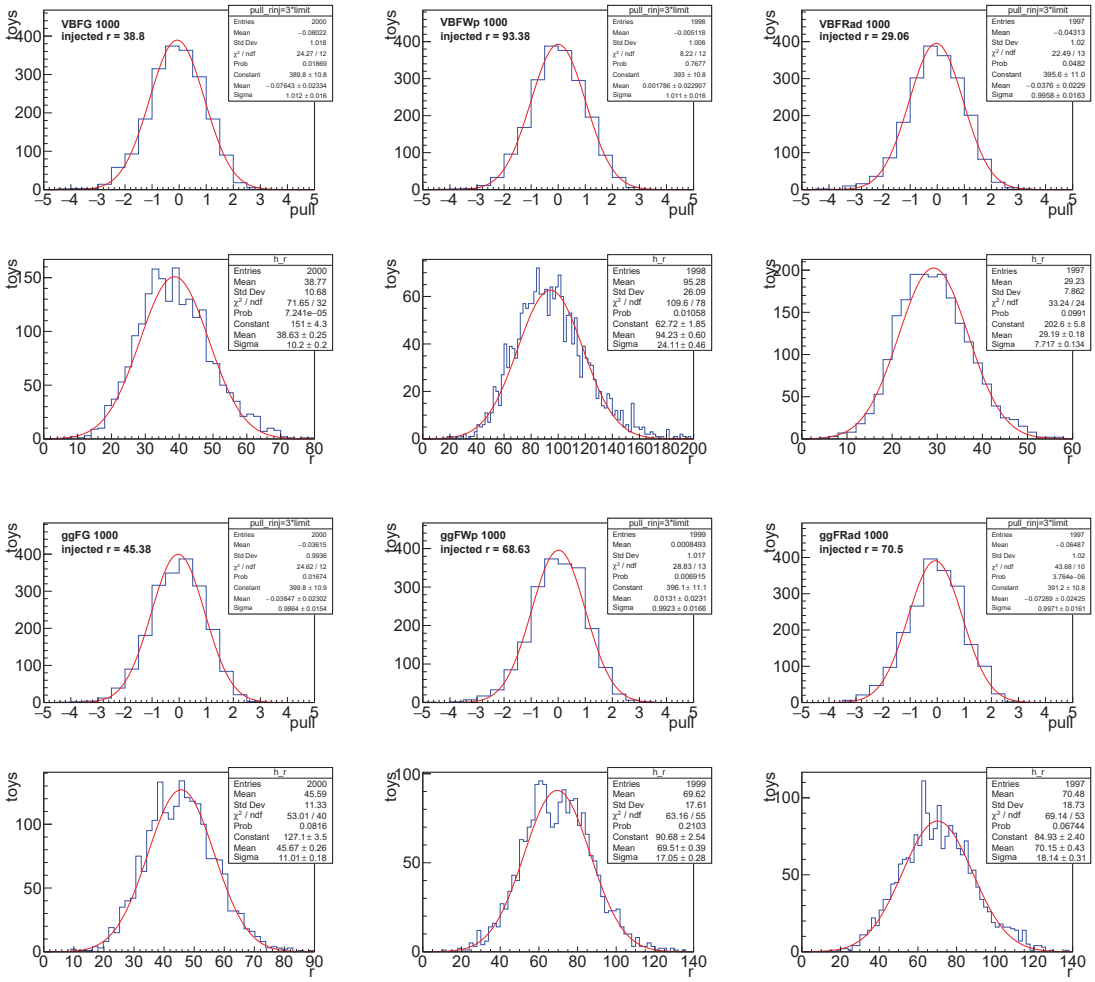

Figure 5.22. Bottom pad: Distribution of the best-fit value of r from ensemble of pseudo dataset sampled from our model of signal and background. For each model, the injected signal strength corresponds to three times the expected 95% CL upper limit on the resonance production cross section after combining both VBF and VBFfail category. Top pad: The distribution of the pull for each set of toys. Top two row are for the combined category using VBF produced sample and bottom two rows are using ggF produced 1 TeV sample.

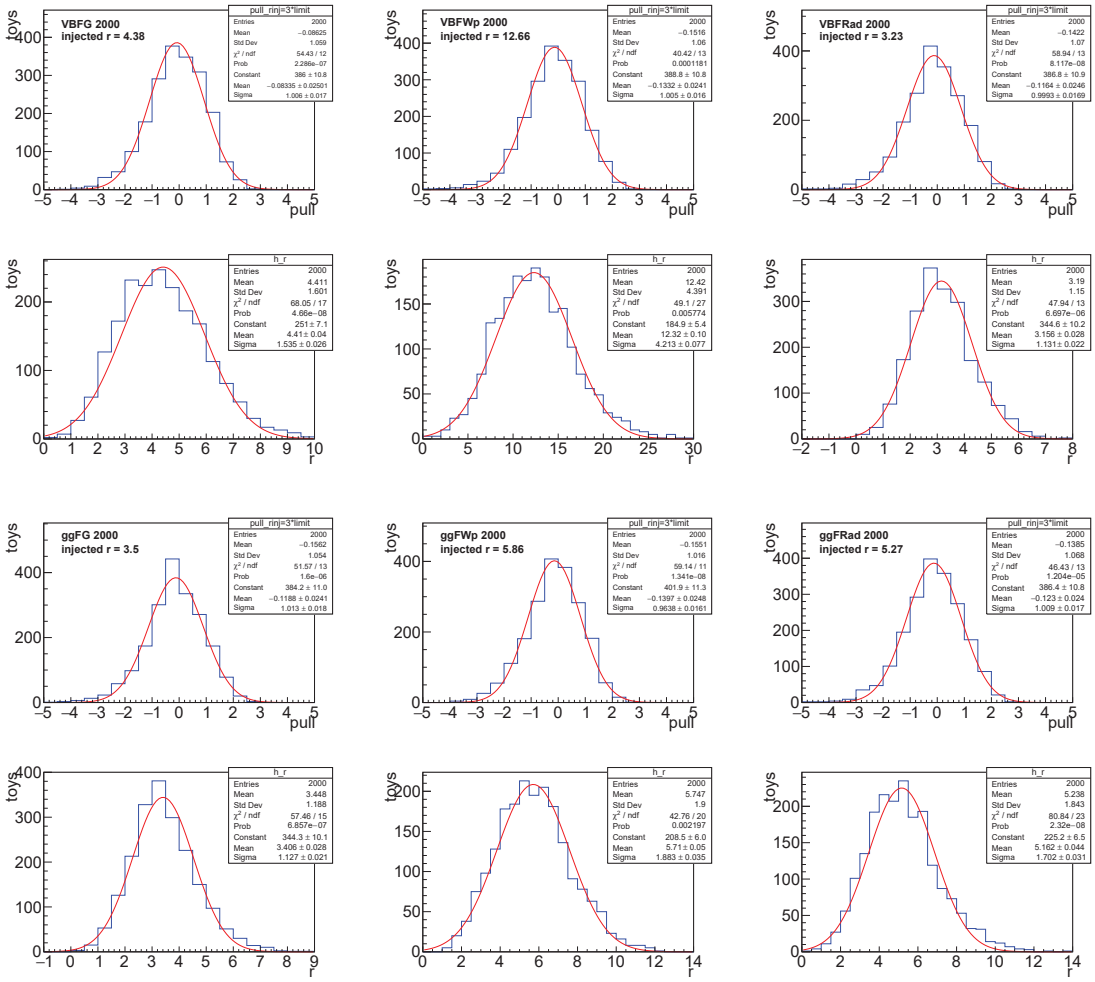

Figure 5.23. Bottom pad: Distribution of the best-fit value of r from ensemble of pseudo dataset sampled from our model of signal and background. For each model, the injected signal strength corresponds to three times the expected 95% CL upper limit on the resonance production cross section after combining both VBF and VBFfail category. Top pad: The distribution of the pull for each set of toys. Top two row are for the combined category using VBF produced sample and bottom two rows are using ggF produced 2 TeV sample.

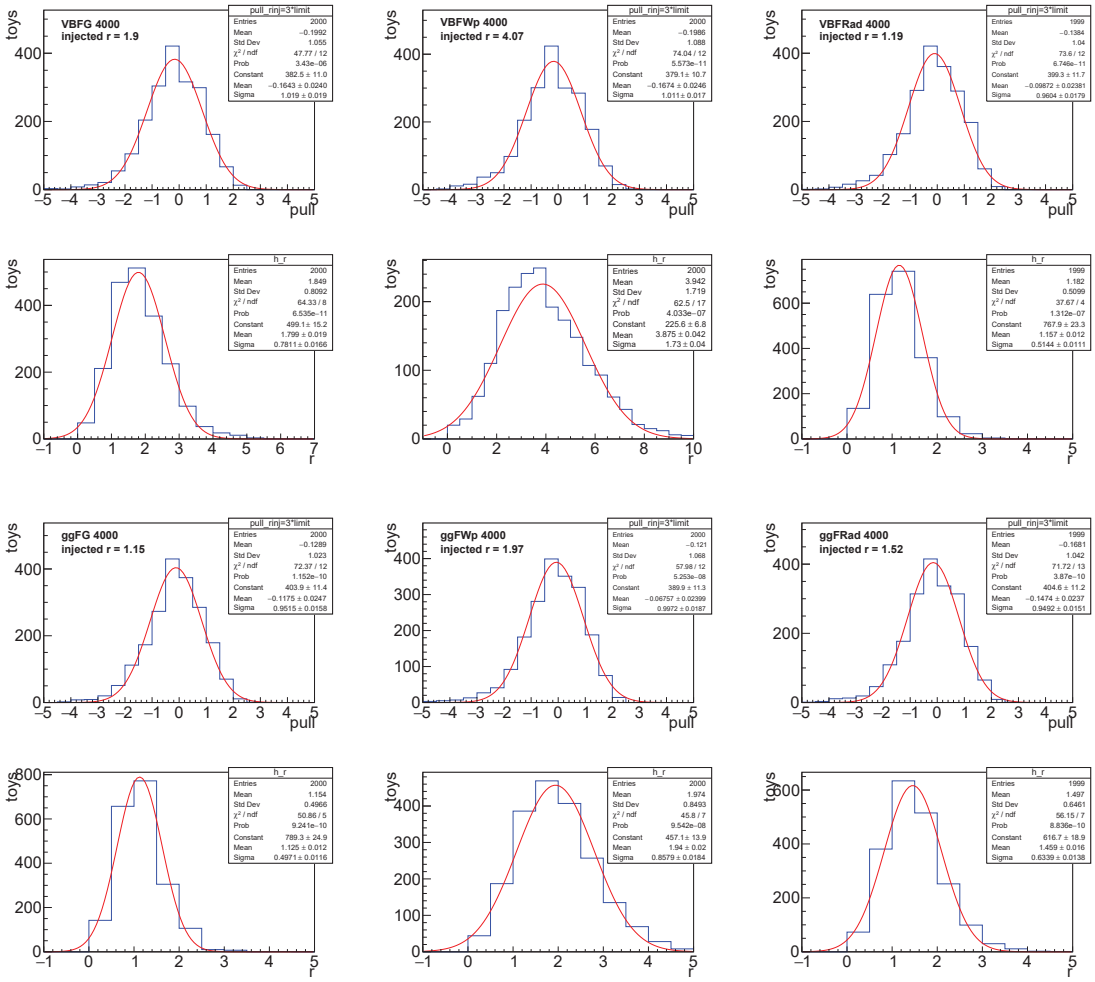

Figure 5.24. Bottom pad: Distribution of the best-fit value of r from ensemble of pseudo dataset sampled from our model of signal and background. For each model, the injected signal strength corresponds to three times the expected 95% CL upper limit on the resonance production cross section after combining both VBF and VBFfail category. Top pad: The distribution of the pull for each set of toys. Top two row are for the combined category using VBF produced sample and bottom two rows are using ggF produced 4 TeV sample.

5.8 Results

Figure 5.25 shows the predicted yields for full run2 ($137\,\mathrm{fb}^{-1}$). The hashed region represents the systematic uncertainty in the prediction. Note, these are prefit predictions; because the control region observations are explicitly modeled in our likelihood, small adjustments can be made after the background-only fit to the control region data. The pre and postfit plots are shown in figures 5.26- 5.27.

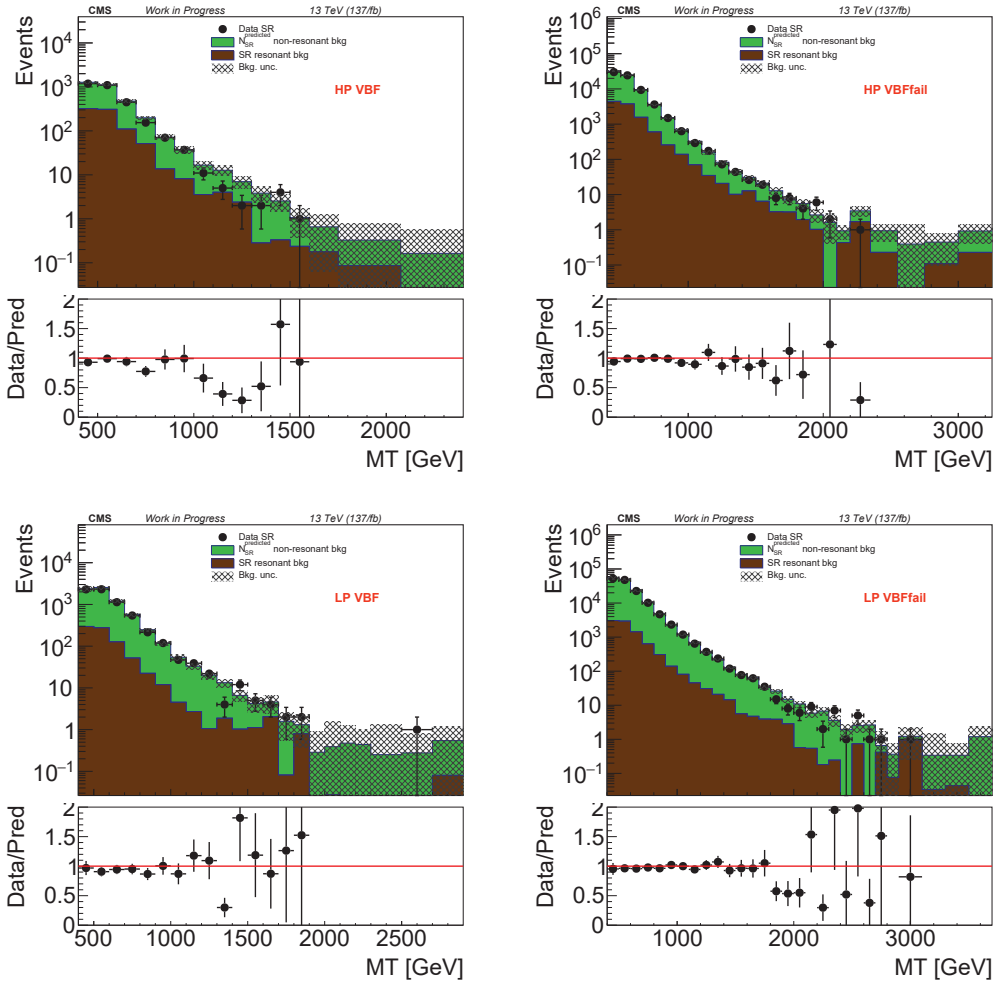

Figure 5.25. Distributions for predicted yields in high purity (top) and low purity (bottom) category. Last bin corresponds to the overflow bin. Left: For VBF event, right: For non-VBF event

Limits are set on the product of the resonance production cross-section and the Z(jj)Z($\nu\nu$) branching ratio. The branching ratio of the resonance decaying to a pair of Z bosons is assumed to be 100%. The test statistic is $q_\mu = -2\ln \mathcal{L}_\mu/\mathcal{L}_{\max}$ is used. $\mathcal{L}_{\max}$ is the maximum of the likelihood while allowing all parameters to vary. $\mathcal{L}_\mu$ is the maximum of the likelihood while fixing μ, the signal strength parameter, and allowing all other parameters to vary. Limits are based on the asymptotic form of the test statistic based on the CL_s criterion described in Refs. [55].

Figure 5.29 shows the expected 95% CL upper limits for the combined (VBF & ggF) category where we see that the spin 0 (Radion) of mass up to 3.0 TeV, spin 1 (Wprime) of mass up to 4.0 TeV and spin 2 (Graviton) of mass up to 1.4 TeV are excluded for the models considered in this dissertation.

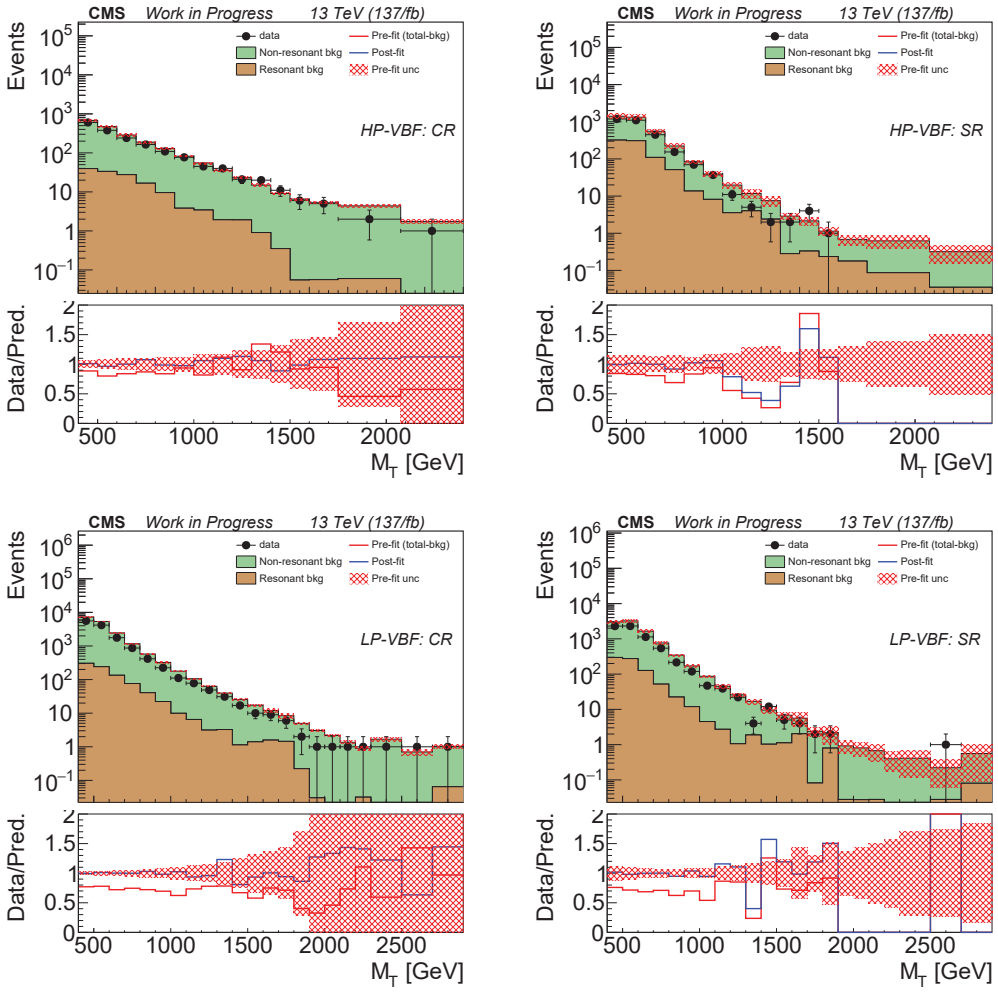

Figure 5.26. Pre and post-fit distributions in high purity (top) and low purity (bottom) category for VBF-pass events. Left: For CR events, right: For SR events

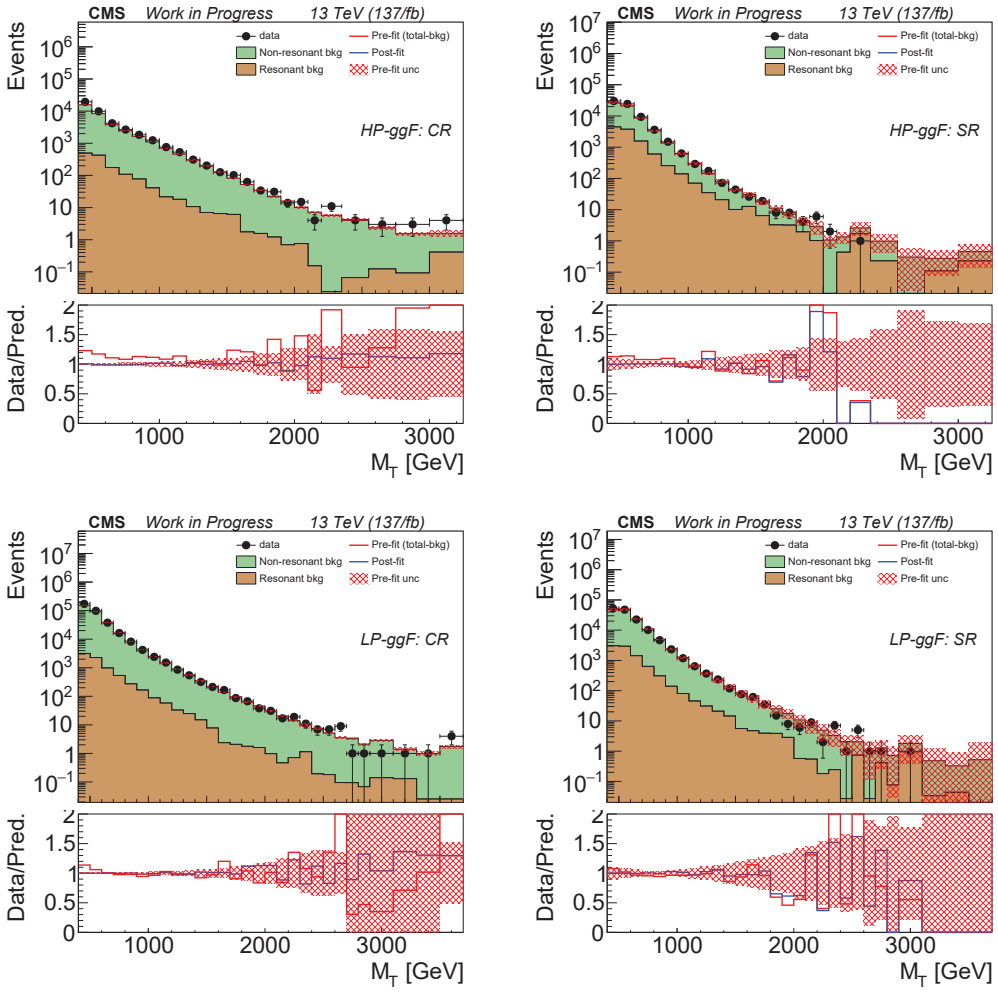

Figure 5.27. Pre and post-fit distributions in high purity (top) and low purity (bottom) category for VBF-fail events. Left: For CR events, right: For SR events

```
imax 2 number of bins
jmax 2 number of processes minus 1
kmax 29 number of nuisance parameters
----------------------------------------------------------------------------------------------------------------------------------
bin          ch1_S7HV       ch1_C7HV
observation  16.6297        45
----------------------------------------------------------------------------------------------------------------------------------
bin                                     ch1_S7HV       ch1_S7HV       ch1_S7HV       ch1_C7HV       ch1_C7HV       ch1_C7HV
process                                 sig            rare           bkg            sig            rare           bkg
process                                 0              1              2              0              1              2
rate                                    0.5584         3.5657         16.2074        0.0061         3.4252         51.5785
----------------------------------------------------------------------------------------------------------------------------------
BkgSB_stat_HPVBF_7      lnN             -              -              -              -              -              1.037
BkgSR_stat_HPVBF_7      lnN             -              -              1.0754         -              -              -
JEC                     lnN             0.889/1.07     1.4            -              0.836/1.11     1.4            -
JECdom_VBF              lnN             -              -              1.03           -              -              -
JER                     lnN             1.026          1.35           -              1.0415         1.35           -
JERdom_VBF              lnN             -              -              1.03           -              -              -
JMR                     lnN             1.0322         1.0117         -              0.9312         0.9406         -
JMS                     lnN             0.9932/1.0086  0.9949/1.0026  -              1.0242/0.9736  1.0179/0.9912  -
Non-closure             lnN             -              -              0.96169545     -              -              -
PDFdom_VBF              lnN             -              -              1.027          -              -              -
PDFnormRare_VBF_CR_HP   lnN             -              -              -              -              1.05           -
PDFnormRare_VBF_SR_HP   lnN             -              1.05           -              -              -              -
PDFshapeRare_VBF_CR_HP   lnN            -              -              -              -              1.04           -
PDFshapeRare_VBF_SR_HP   lnN            -              1.04           -              -              -              -
Pileup                  lnN             1.0024         1.0389         -              1.0068         1.0198         -
Prefiring               lnN             1.0101         1.0065         -              1.0104         1.0081         -
RareSB_stat_HPVBF_7     lnN             -              -              -              -              1.2473         -
RareSR_stat_HPVBF_7     lnN             -              -              1.3281         -              -              -
SclDom                  lnN             -              -              0.98           -              -              -
SclNormRare             lnN             -              1.15           -              -              1.15           -
SclShapeRare            lnN             -              0.9            -              -              0.96           -
SigSB_stat_HPVBF_7      lnN             -              -              -              1.3968         -              -
SigSR_stat_HPVBF_7      lnN             1.0425         -              -              -              -              -
Trigger                 lnN             1.0136/0.9923  1.0102/0.9862  -              1.0137/0.9921  1.0084/0.9863  -
Unclusturedenergy       lnN             1.001          1.0244         -              1.001          1.0176         -
Vtag-pT-extrap          lnN             1.0816/0.9246  1.086/0.921    -              1.0816/0.9246  1.086/0.921    -
Vtag_tau21_sf           lnN             1.0726/0.9274  1.0726/0.9274  -              1.0726/0.9274  1.0726/0.9274  -
bveto                   lnN             1.0131         1.0244         -              1.0141         1.0351         -
lumi                    lnN             1.02439        1.02439        -              1.02439        1.02439        -
rateparam_7_HPVBF  rateParam ch1_S7HV bkg 1 [1e-5,10]
rateparam_7_HPVBF  rateParam ch1_C7HV bkg 1 [1e-5,10]
```

Figure 5.28. Datacard for a single bin (value of 1000) for a 1 TeV VBF G sample.

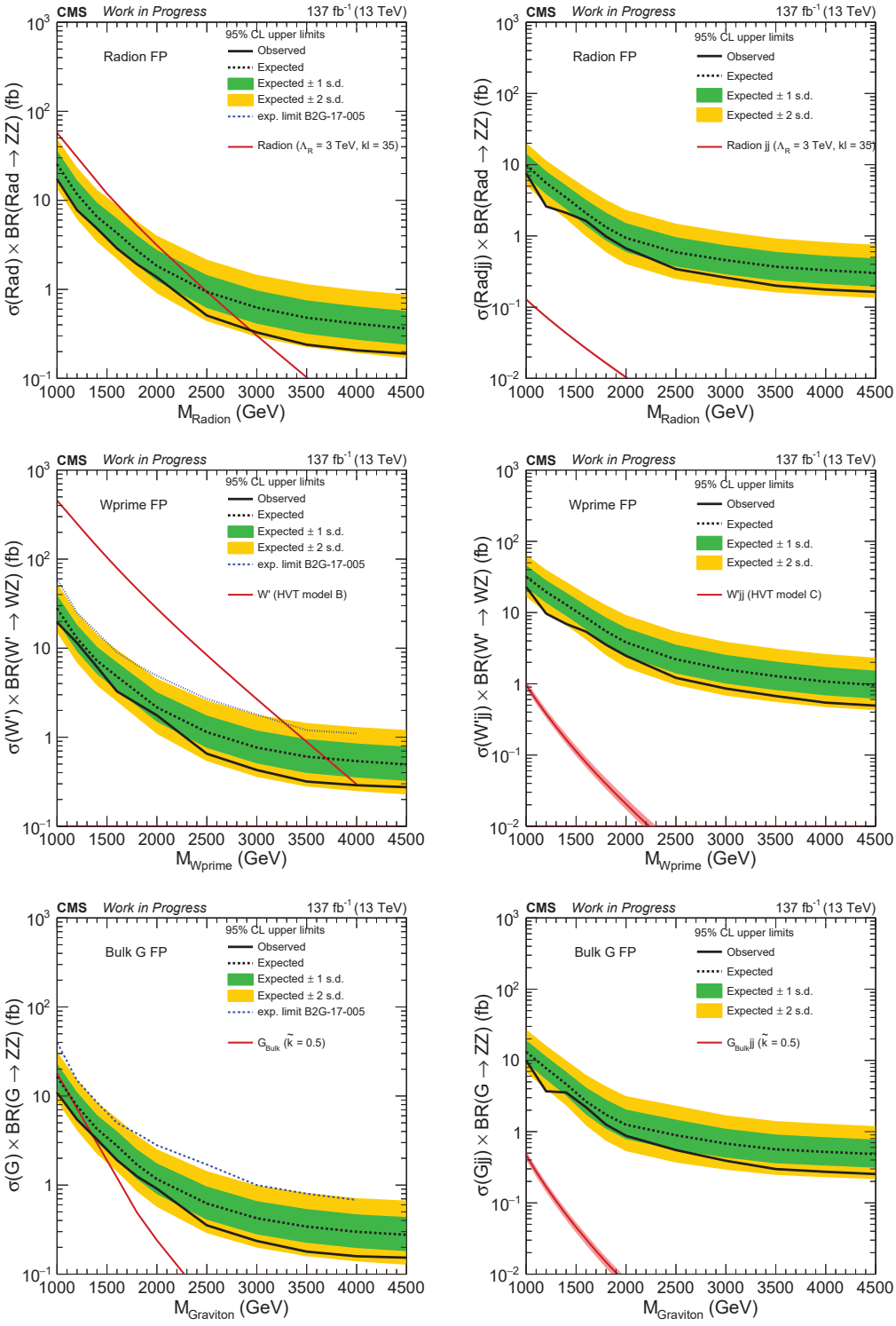

Figure 5.29. Expected 95% CL upper limit on $\sigma \times BR(X \rightarrow WZ/ZZ)$ for spin 0, 1, and 2 (top to bottom) after combining the VBF-pass, VBF-fail, high , and low purity category using the ggF samples (left) and VBF samples (right).

Chapter 6

Development of Silicon Module Assembly Techniques for the CMS High Granularity Calorimeter

6.1 Introduction

The physics program at the LHC with the top priority to discover the Higgs boson started with the first proton-proton collisions in 2009 at $\sqrt{s} = 900$ GeV [30]. The LHC commissioning schedule is shown in figure 6.1 [17]. During the Run1 (till 2012), LHC delivered 30 fb^{-1} of data and the most significant result was the discovery of the Higgs boson. After achieving overwhelming success in Run1, LHC continues running in Run2 even at higher $\sqrt{s}$ (13 TeV) and delivers the data at an unprecedented rate (see section 3.1) with the aim to produce the beyond the standard model signal such as extra dimensions, dark matter candidates, or supersymmetry. In Run2, LHC delivered 190 fb^{-1} which is about six times larger than in Run1. Despite the magnificent performance of the accelerator itself, LHC has not been able to deliver any other new discovery or a hint of BSM. This means physicists need to dig deeper and need large volumes of data in order to be able to observe rare phenomena. This is why the high luminosity (HL) LHC is planned to fully exploit the capability of the LHC which is expected to deliver the 3,000 fb^{-1} of data. The HL-LHC is expected to level the instantaneous luminosity at 5×10^{34} $\text{cm}^{-2}\text{s}^{-1}$ and the mean number of collisions per bunch crossing (pileup) of 140 with the potential of 50% higher luminosity. This is simply amazing from the LHC side; however, this poses an enormous challenge for radiation tolerance and event pileup on detectors, mainly in the forward region. The current endcaps of CMS ECAL ($PbWO_4$) and HCAL (plastic scintillator) were designed for an integrated luminosity of 500 fb^{-1}. The performance degradation of these endcaps beyond this luminosity presents an unacceptable loss of physics potential. Hence, these endcaps need to be replaced and CMS is replacing these with the high granularity calorimeter (HGCAL). In regard to the physics outcome, good jet identification and measurement is crucial for HL-LHC, and part of the plan is to trigger on the narrow VBF jets, merged jets due to the boost. The HL-LHC physics reach includes the physics processes involving VBF process, boosted topology and this

is exactly what this dissertation covers. Hence, the results for the physics processes presented in this dissertation will be relevant to the HL-LHC and the HGCAL.

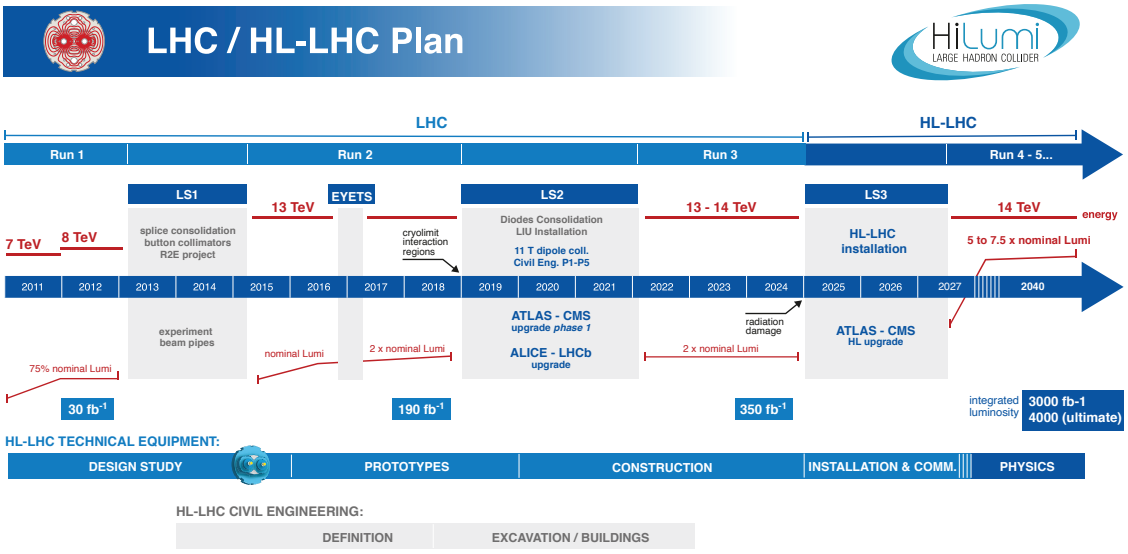

Figure 6.1. LHC commissioning schedule.

The radiation level foreseen during the HL-LHC run is about ten times higher than the present CMS design. The simulations study as seen in figure 6.2 shows the highest dose and fluence of around 2 MGy and 10^{16} n_{eq}/cm^2 respectively (where n_{eq}/cm^2 denotes the number of 1 MeV equivalent neutrons per square cm). It is learned from the silicon tracker upgrade R&D that the silicon sensors can withstand such radiation levels (retain adequate charge collection efficiency when cooled to -30^0 C). Hence, silicon sensors were chosen for the active material in the high radiation area in HGCAL design, see [30] for details.

6.2 Structure of the CMS HGCAL

The CMS HGCAL covers $1.5 < |\eta| < 3.0$ and comprise of two active materials: silicon (Si) in the high radiation region i.e. closer to the interaction point and plastic scintillator (Sc) in the low radiation region as seen in figure 6.2. There are 6M Si chan-

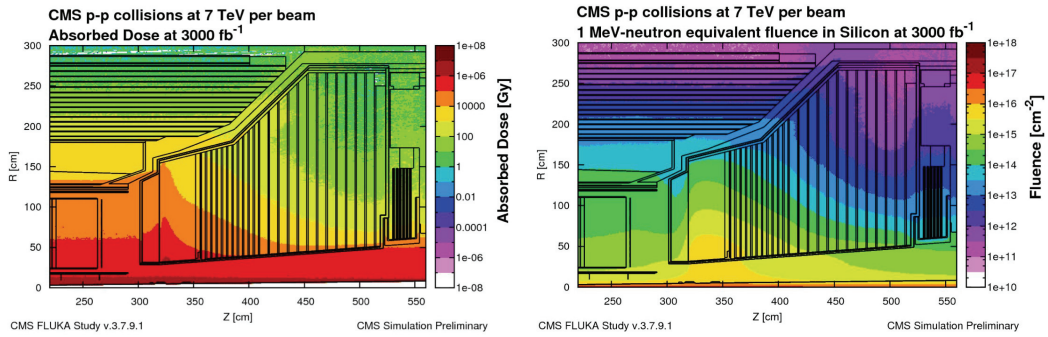

Figure 6.2. Radiation dose (left) and fluence (right) accumulated in HGCAL at the end of HL-LHC.

nels with a cell size of 0.5 or 1.1 cm^2 in about 27,000 modules. HGCAL is a sampling calorimeter with two components; electromagnetic (CE-E) and hadronic (CE-H). The electromagnetic part has Si as an active material, Cu/CuW/Pb absorbers, 28 sampling layers, a total thickness of 34 cm and the depth represented by the radiation and interaction length of about 26 X_0 and $1.7\lambda_D$ respectively. The hadronic part contains Si and Sc as the active material, steel absorber, 24 sampling layers, and the total depth of about $9.0\lambda_I$. The depletion region thickness for the Si sensors is 300, 200, and 120 μm in the ascending order of the fluence. To reduce noise due to high radiation, the Si sensors have to be operated at -30^0C. Furthermore, SiPMs which register the light from Sc also has to be operated at the same low temperature to keep the radiation-induced noise low.

The structure of a module is shown in figure 6.4 which consists of a 1-mm thick baseplate, gold layered Kapton sheet, silicon sensor, and a printed circuit board (PCB) or hexaboard. The baseplate provides the mechanical support to the Si sensor and the precise reference hole helps in assembly and mounting to the cassette. The design baseplate materials are CuW for CE-E and PCB for CE-H. The Kapton itself provides electrical insulation to the sensor backplane from the baseplate which is held at ground. A thin gold coated layer on top of the Kapton sheet provides the HV bias connection to the sensor back-plane through a conductive epoxy. The hexaboard hosts the HGCROC chip for the on-board digitization of the signals from the sensor

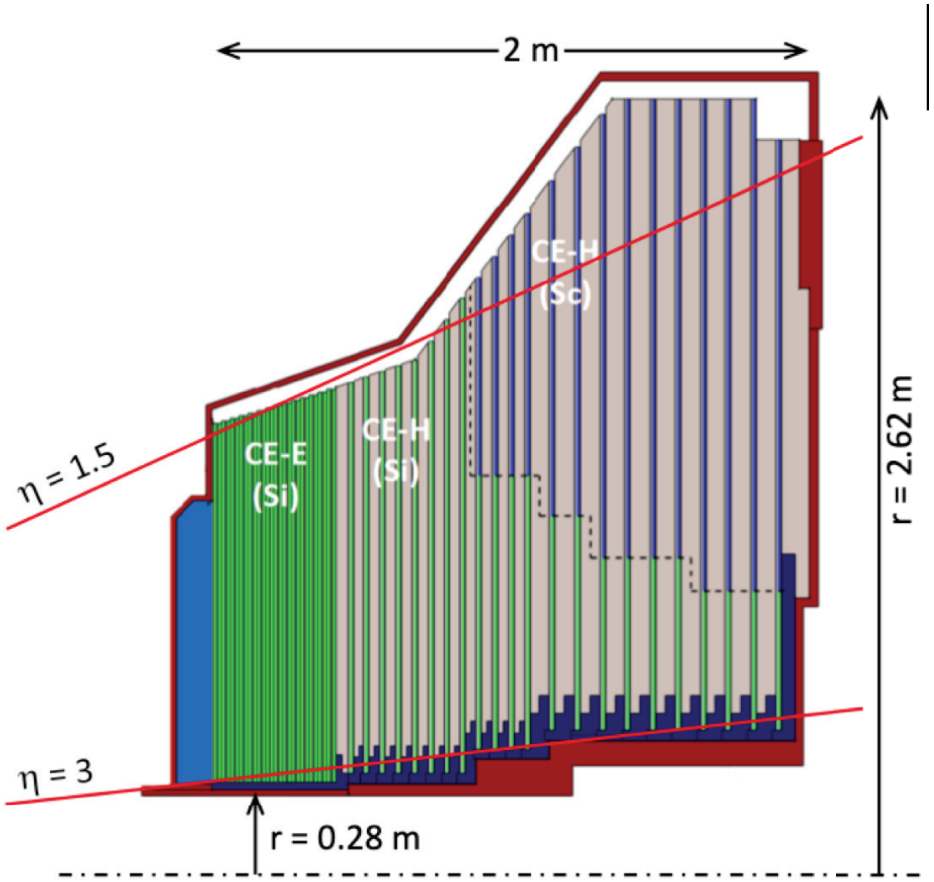

Figure 6.3. Schematic view of the CMS HGCAL.

pad. Both Si sensor and the hexabord are hexagonal (see figure [**?**]) with a little cutout at each corner which provides the reach to the positioning and the mounting holes in the baseplate at the bottom.

6.3 Mockup program for Silicon modules and cassette

The mockup program as a part of USCMS HGCAL modules and cassette project was started at Texas Tech University (TTU) in 2017. The main purpose of the mockup program was to optimize the materials and construction techniques and tools to build the Si-based modules and to perform the thermal and mechanical test of the prototype for the 8" Si modules for CE-H. TTU shares the responsibility of making ∼5,000 Si modules which represents the half of the total US contribution for

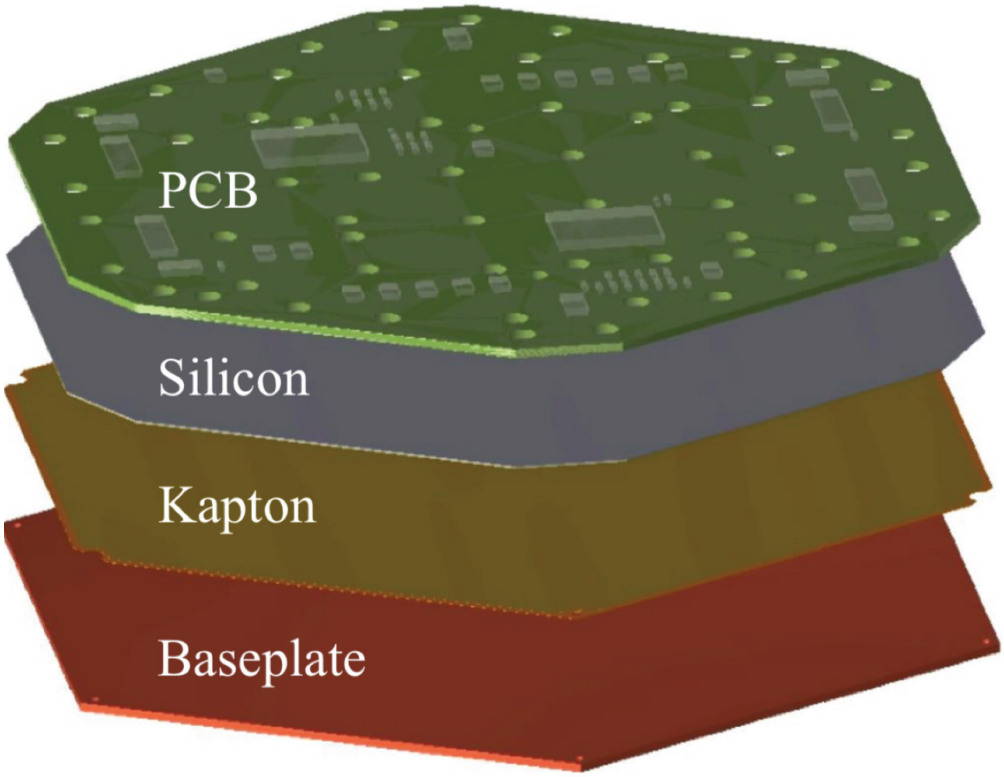

Figure 6.4. CMS HGCAL Silicon module structure.

the standard 8" modules. Mockup program considered the various materials such as brass, stainless steel, carbon fiber, CuW, PCB (Copper coated FR4) like materials for the baseplate, and modules were built with each of these baseplate materials. Silicon sensors used in mockup were aluminum coated and were cut from 8" wafers of 750 & 320 μm thick. Lastly, the PCB built for the mockup hosts few heaters and RTDs (resistance temperature detector) which were designed to apply heat loads and measure the temperature of the Si sensors. A two-component epoxy used to glue one layer to the other was 'Araldite 2011' [1] which is thermally conductive but not electrically. For electrical conduction as discussed previously to be applied on top of the gold-coated Kapton, silver epoxy such as 'EPO-TEK H20' [13] was used.

In addition to those aforementioned individual components cut to the specifications, the module assembly procedure requires controlled epoxy dispensing, assembly of two components, and curing of the epoxy. The 'Ultimus V High Precision Dis-

penser' [22] was used to dispense the glue from a syringe and to drive the syringe to the different location of desire a programmable router gantry, 'Probotix CNC' [4] was used. The gantry was controlled with the "G-code" [9] output by the 'Cut2DPro' [5] software (commonly used in a machine shop). The gluing requirement was such that each layer should be 75-100 μm thick with little or no air bubbles. This is more complicated for PCB to Si gluing as the glue should not be in contact with the electrical parts and more importantly, glue should not ooze out to the many little holes needed for the wire bonding.

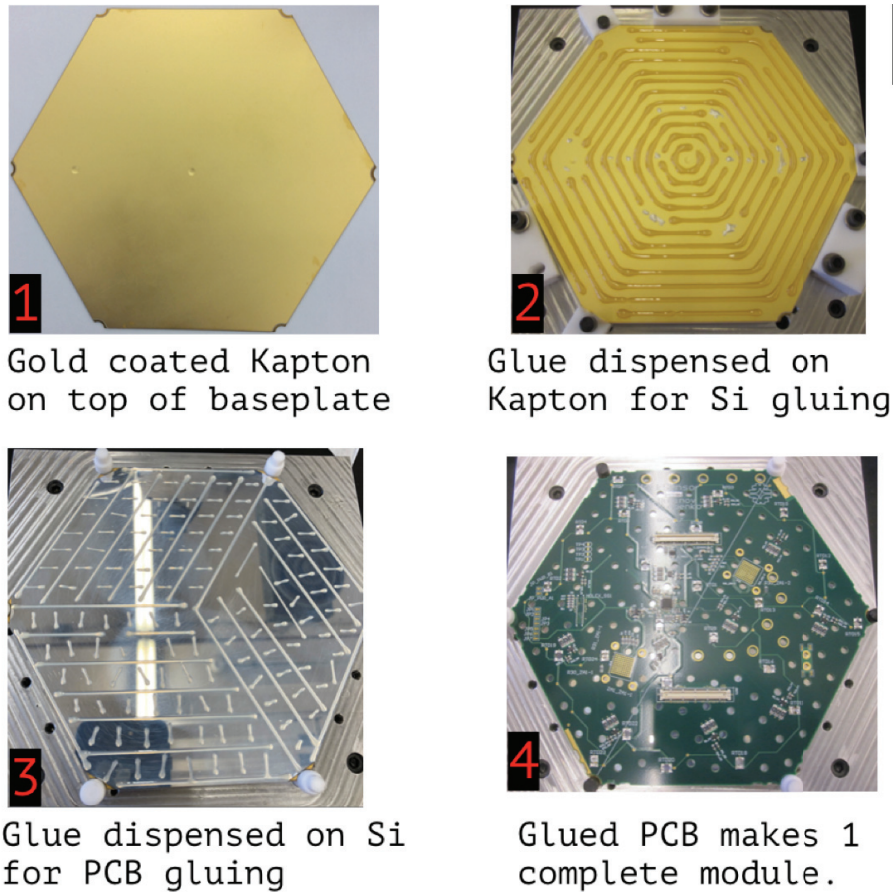

Figure 6.5. Various assembly stages for a Silicon module.

The module assembly procedure was performed in sequence i.e. first the glue was dispensed on the surface of the baseplate to glue the gold-coated Kapton sheet. Then those parts were stored until the epoxy gets cured which usually takes about

7-10 hours at room temperature. In order to have a uniform distribution of the glue, a load with a flat surface is applied on the top while curing. The next steps were repeating the same procedure but now gluing Si on top of the gold-coated Kapton sheet, then followed by gluing the PCB on top of the Si sensor. After curing, this gives a complete mechanical module (wire bonding was done at a later stage). These sequences along with the glue patterns for each stage are shown in figure 6.5. TTU produced about 50 mockup modules which were used for thermal and mechanical tests as well as to build the first HGCAL cassette prototype.

The test of the modules was mostly focused on the thermal and mechanical performance of the silicon sensors as well as the materials used for the baseplate and PCB. Since the HGCAL is expected to operate at -30^o C for many years, so the prototypes were tested by thermally cycling from -30^o C to $+30^o$ C. For this, a programmable thermal chamber (Espec [10]) was used. This chamber allows us to precisely set the temperature and humidity inside the chamber where specimens are placed. Inside the chamber, purging was accomplished with the dry air. Three modules connected with a motherboard which reads the information of the modules using the raspberry pi are placed inside the chamber. This setup is shown in figure 6.6 The whole system is kept insulated and while performing the thermal cycling temperature readings of the Si sensors from the modules were taken. The precision of the measurement was 0.1^o C, hence there was no need for calibration. This precision was achieved using the 4-wire RTDs to measure the temperature of the Si sensors. The first round of the thermal cycling was performed on the modules with the brass baseplate and we observed significant warping of the baseplate as we drop the temperature below -10^o C. As it reached to -30^o C, the bending was so significant that the PCB got delaminated at the cost of cracking the Si sensor. This case is shown in figure 6.7. The coefficient of the thermal expansion (CTE) of brass is much larger (17×10^{-6} 1/K) than Silicon (3×10^{-6} 1/K), so the Si doesn't contract much but the brass does. Perhaps the glue strength between the PCB and Si was not strong enough to overcome the downward bending of the baseplate. Hence, the brass bends cracking Si. With more investigation, it was observed that the PCB delamination occurs only on the edges with little or no glue. After ensuring sufficient glue was applied (mostly at the edges), no more crack was observed. These tests were critical to decide the

baseplate material. The current choice of PCB material for baseplate for the (CE-H) was inspired by this test result. The modules passing these tests were used to build a cassette at the Silicon Detector facility (SiDet), Fermilab.

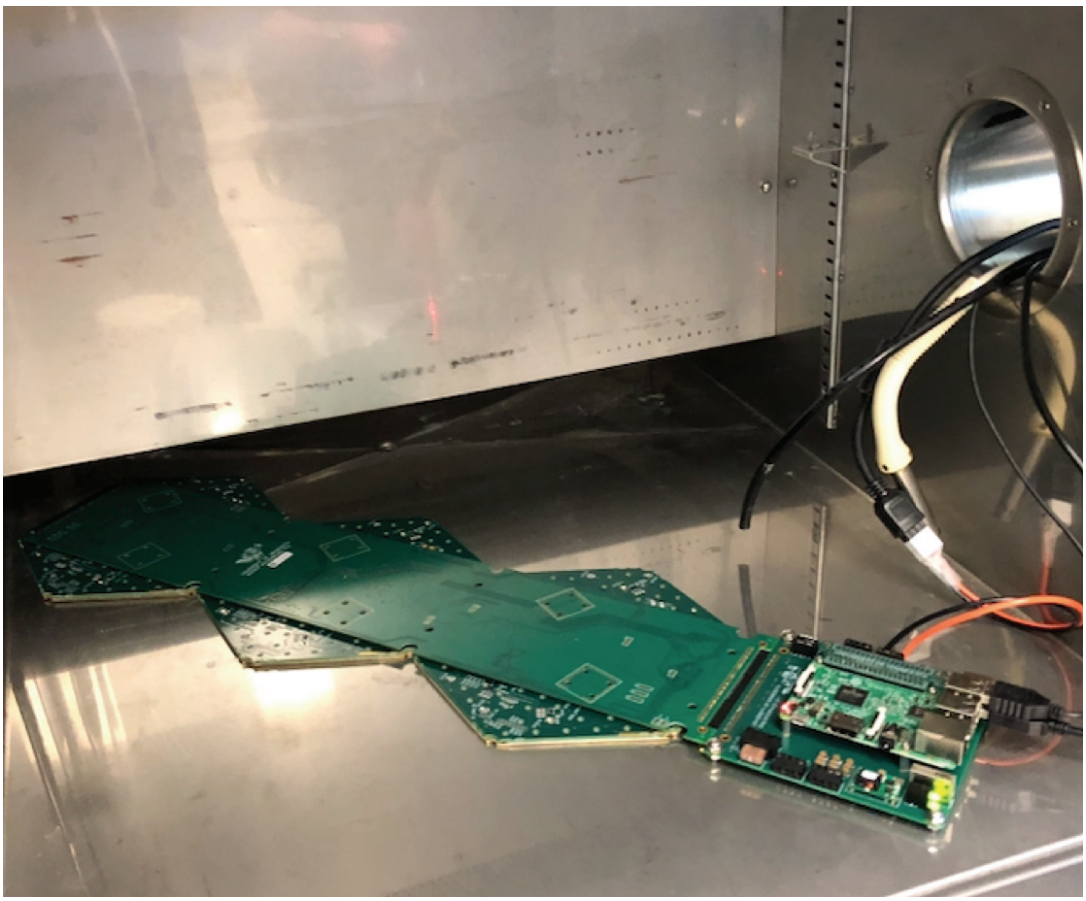

Figure 6.6. Silicon modules connected to a motherboard placed inside a thermal chamber for thermal test.

The modules are grouped into 30^o or 60^o wedges called cassettes. Cassettes are inserted between the absorber layers to form full disks of the detectors in the CE-H whereas, for CE-E, they are assembled into the full disks. A cassette as seen in figure 6.8 is also a stack structure of copper cooling plate at the bottom, modules populated on the cooling plate, motherboards are mounted on rows of modules, and everything covered by a cover plate which is similar to the cooling plate and serves a mechanically and electrically protective layer. This sequence of stacking the various

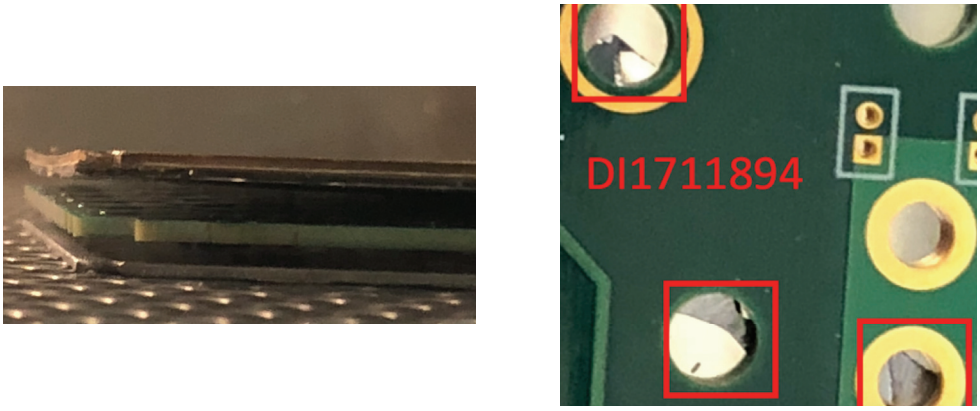

Figure 6.7. Delamination of the PCB with warping of the baseplate (left) resulting the crack in Si sensor (right)

components is shown in figure 6.9 which were placed in a cold box to perform the thermal and mechanical test of the Si sensors in a cassette. The two-phase CO_2 was used as a cooling agent [93] which were circulated through the cooling plate via small tubing.

The lesson learned from the single module testing was that the baseplate warps at low temperatures. So, one of the first tests performed for the cassette is how much those modules sitting on the top of the cooling plate in warps. For this, as shown in figure 6.10, the coordinate measurement machine (CMM) was used which measured the height of the center with respect to the average of six corners ($\Delta Z_{\text{center - 6 corners}}$). The measurement value of this variable along with the result from the finite element analysis (FEA) [11, 23] simulation is presented in figure 6.11. The positive value of this offset means that the baseplate was bending in a way that the center of the module losing contact with the cooling plate. This situation is not desired as the thermal contact of the module with the cooling plate is compromised. The desired scenario is where the center of the module presses into the cooling plate with the edges bending up. This is acceptable as the edges would be pressed down by the screws at the corners. This result rules out the possibility of using the brass as the baseplate material whereas the CuW, carbon fiber (CF), and PCB all are acceptable and the deflection measurement matches very well with the simulation. Simulation of the CF doesn't match the measurement this is because the CF used was a commercial

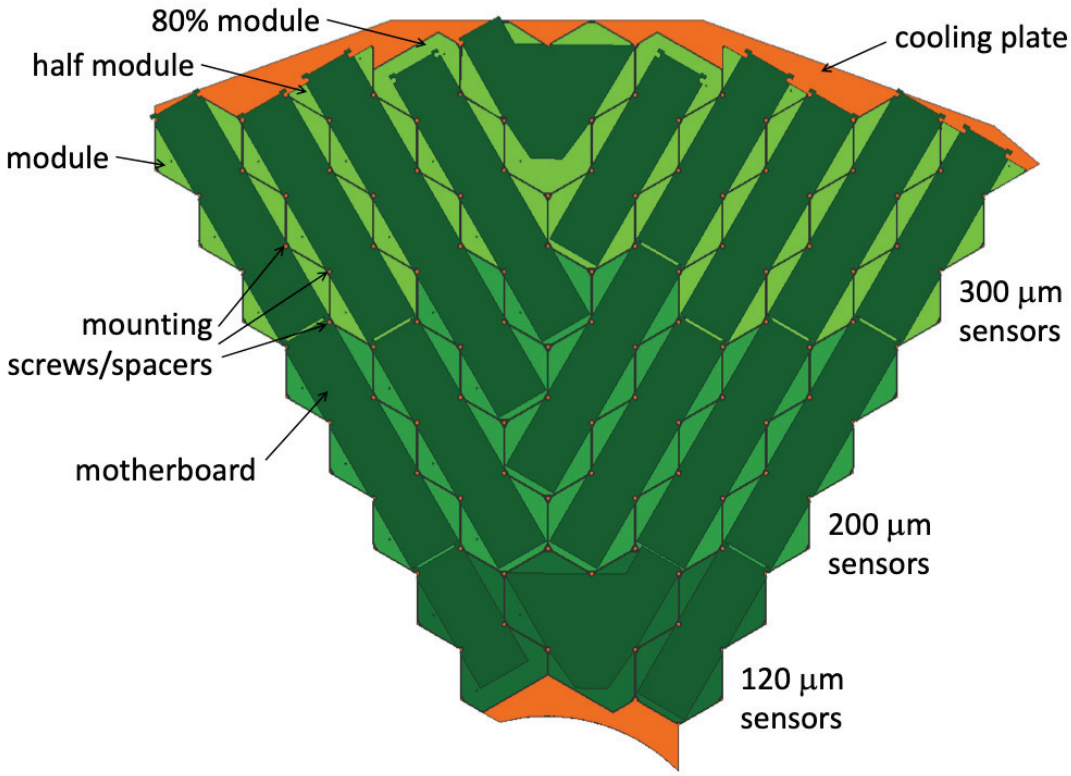

Figure 6.8. HGCAL cassette structure.

product and the detailed specifications of which were not precisely known.

The final test is to measure the temperature of the Si sensor in a cassette while the module is fully powered. For this test, the temperature of the Si sensors was readout by RTDs (8 RTDs per module). The measured value and the schematics of the population of the modules in the cassette are shown in figure 6.12. The heat load supplied was 270 Watts and the CO_2 temperature at the outlet of the cooling plate (tube) was -35^o C. The highest temperature of the Si sensor was measured to be -31^o C and -30^o C for the modules built with CuW and PCB baseplate respectively.

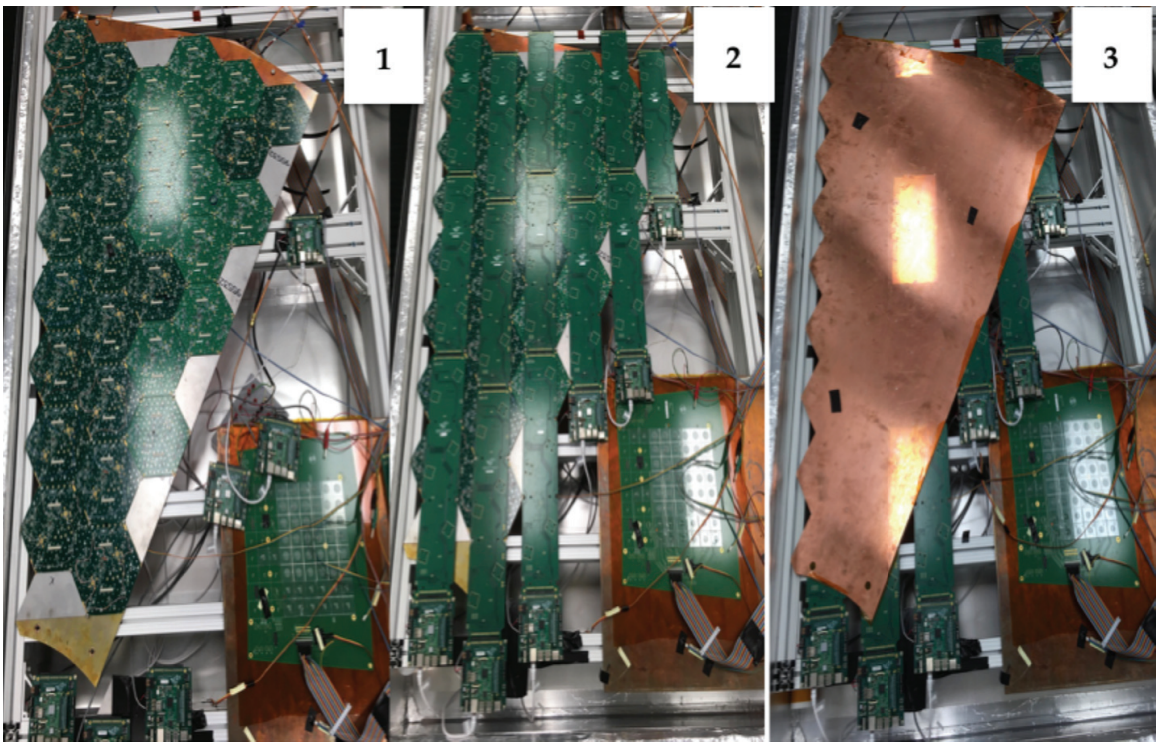

Figure 6.9. HGCAL cassette assembly in a cold box. Modules populated on a cooling plate (1), motherboard connected to the module (2), cover plate on top making a complete cassette (3).

6.4 Summary

The HGCAL mockup program for standard 8" silicon modules and cassette for CE-H was successfully completed. The first milestone for thermal and mechanical study for modules and cassettes has been successfully achieved. An extensive set of detailed simulations and tests with full-scale realistic mock-ups were performed to optimize the tools, techniques, design, and to arrive at a fully engineered solution. Aftermath, a more advanced robotic gantry, wire bonding machine, OGP machine has been added at the Advanced Particle Detector (APD) lab at TTU in preparation for the mass production of the real modules.

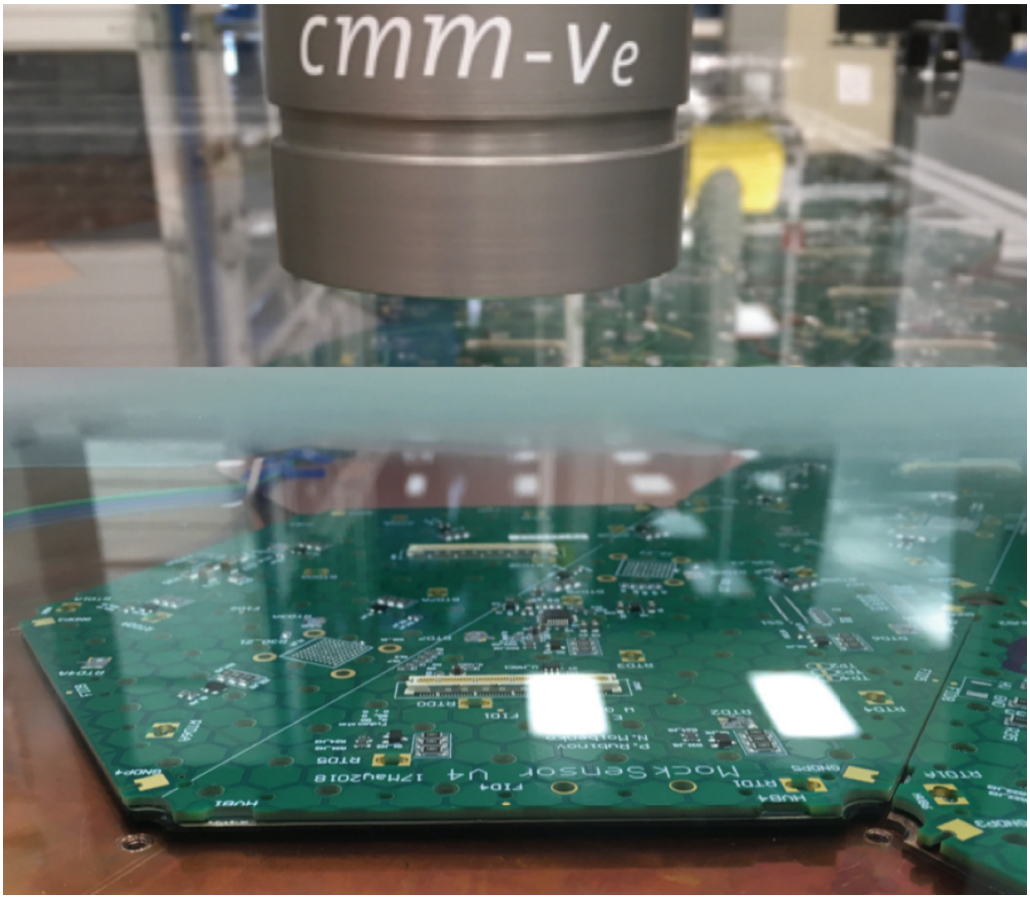

Figure 6.10. Set up to measure the flatness of the modules at -30^{o} C in cassette using CMM.

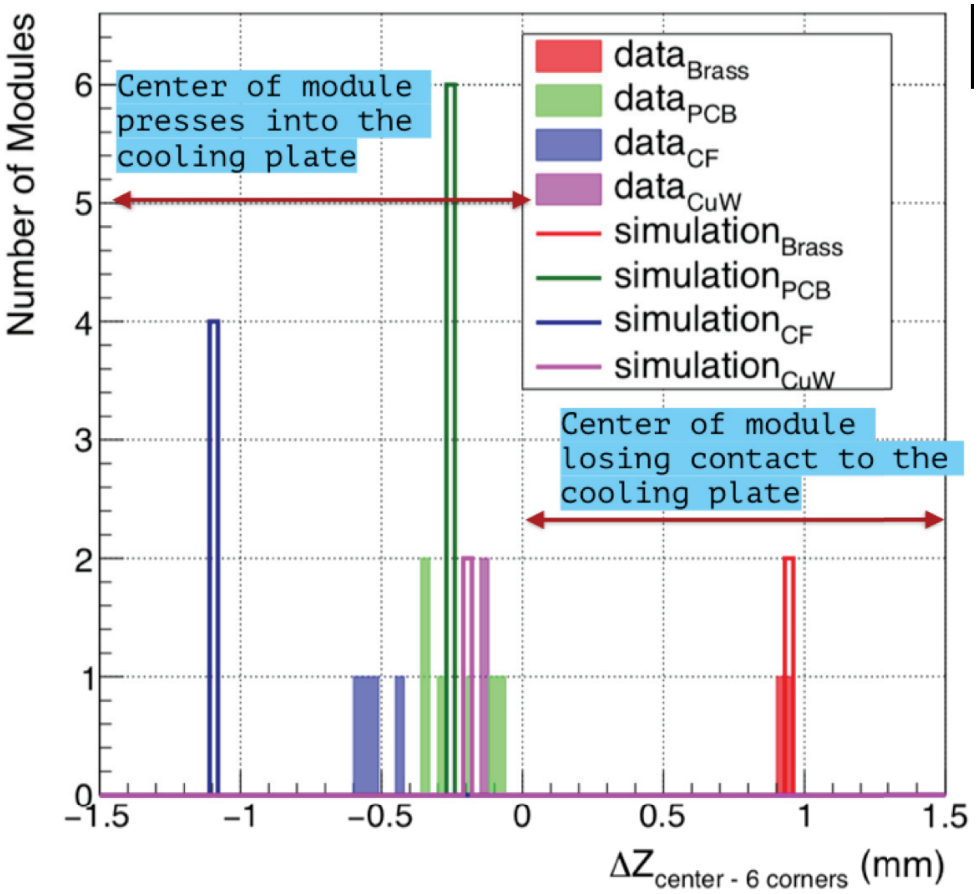

Figure 6.11. Flatness measuremnt of the modules at -30^o C and comparison to the simulation.

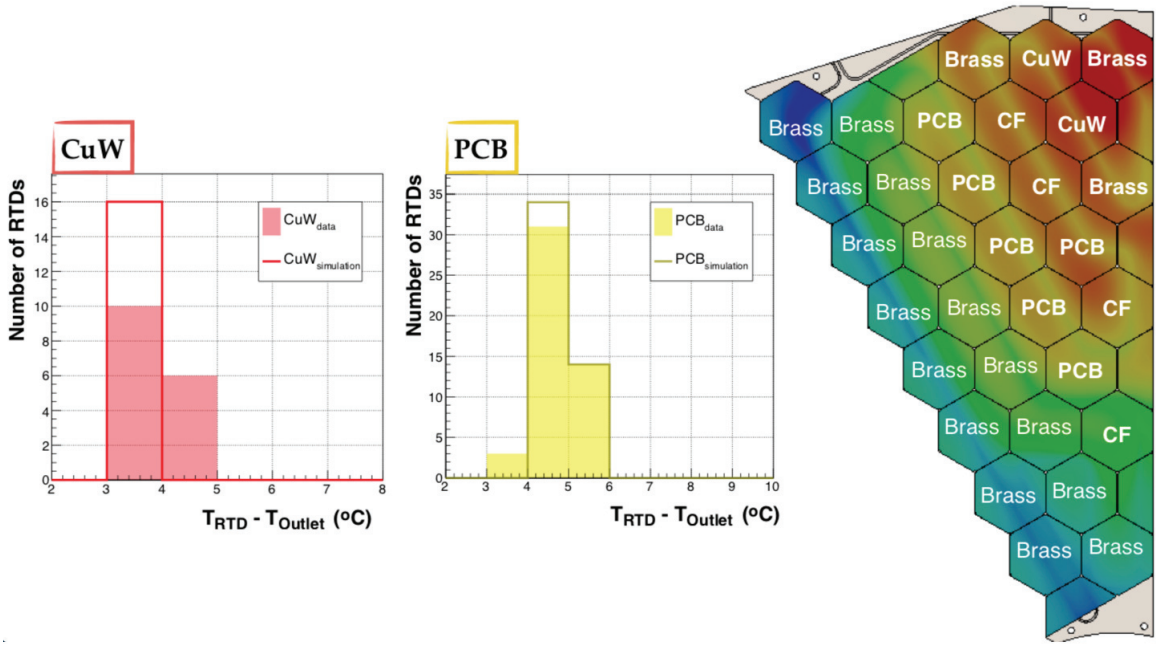

Figure 6.12. Measured thermal performance of the Si sensors in cassette for modules with CuW (left) and PCB (middle) baseplate.

Figure 6.13. HGCAL collaboration members with the first mockup cassette at SiDet at Fermilab.

Chapter 7

Conclusion

A search for new bosonic states which decay to either a pair of Z bosons or a Z-boson and a W-boson is presented. The final state used requires one high momentum large-radius jet which is tagged and has mass consistent with either a Z boson or W boson and large missing transverse momentum. Events are also categorized based on the presence of high momentum jets in the forward region of the detector to distinguish gluon-gluon fusion and vector boson fusion production mechanisms. The dominant SM backgrounds are estimated using an extrapolation method from the jet mass sideband distributions. No evidence of a new state is found and 95% CL upper limits are set on various signal models. For ggF-produced resonances, we expected to exclude Radions up to 3.0 TeV, W's up to 4.0 TeV, and Bulk Gravitons up to 1.4 TeV. For VBF-produced resonances, we are not yet sensitive to the models considered because the production cross-section is smaller than the current experimental reach.

The jet substructure technique (N-subjettiness) and forward jet tagging to identify the boosted hadronic W/Z and the forward jets respectively were studied. One of the key aspects of this dissertation is that it explores the dominance of the polarization effect in the VBF production mode for non-scalar resonances which arises from spin correlations between initial state vector boson and final state vector bosons. This feature is missing in ggF production mode. These searches in the VBF production mode in this particular channel are new in the CMS experiment i.e. no previous results exist from the CMS experiment. Furthermore, although it is not discussed extensively in the dissertation; however, the same phase space explored in this dissertation also covers the new resonance decaying to a hadronic W or a Z-boson and an invisibly decaying Higgs boson channel. The public result corresponding to this perspective has not yet been available from the CMS experiment.

A brief overview of the HL-LHC and the HGCAL upgrade is also presented. The assembly techniques for the silicon modules and cassettes and the various tests in regard to the thermal and mechanical performance of the silicon sensors are extensively discussed. The first prototypes of the silicon modules were built and passed all

the rigorous thermal and mechanical tests. In addition to the increased amount of data in HL-LHC, the physics analysis presented in this dissertation will be benefitted from the CMS HGCAL.

References

[1] ARALDITE® 2011 :: Huntsman Corporation (HUN). https://www.huntsman.com/products/araldite2000/araldite-2011. (Accessed on 10/2/2020).

[2] CMS | CERN. https://home.cern/science/experiments/cms. (Accessed on 10/01/2020).

[3] CMS detector design | CMS Experiment. http://cms.web.cern.ch/news/cms-detector-design. (Accessed on 10/1/2020).

[4] CNC Router | American Made | PROBOTIX CNC ROUTERS. https://www.probotix.com/CNC-ROUTERS. (Accessed on 10/2/2020).

[5] Cut2D Pro Product Page | Vectric. https://www.vectric.com/products/cut2d-pro. (Accessed on 10/2/2020).

[6] Dark Energy, Dark Matter. https://science.nasa.gov/astrophysics/focus-areas/what-is-dark-energy. (Accessed on 10/2/2020).

[7] Dark matter. https://home.cern/science/physics/dark-matter. (Accessed on 10/2/2020).

[8] Detecting muons | cms experiment. https://cms.cern/detector/detecting-muons. (Accessed on 10/1/2020).

[9] Easy CNC Mill G-Code and M-Code Reference List [Examples & Tutorials]. https://www.cnccookbook.com/g-code-m-code-reference-list-cnc-mills/. (Accessed on 10/2/2020).

[10] ESPEC North America. https://espec.com/na/. (Accessed on 10/2/2020).

[11] Finite Element Analysis Software | Autodesk. https://www.autodesk.com/solutions/finite-element-analysis. (Accessed on 10/2/2020).

[12] Hadron Calorimeter | CMS Experiment. http://cms.web.cern.ch/news/hadron-calorimeter. (Accessed on 10/1/2020).

[13] Home - epoxy technology inc. https://www.epotek.com/site/. (Accessed on 10/2/2020).

[14] How an accelerator works | CERN. https://home.cern/science/accelerators/how-accelerator-works. (Accessed on 10/1/2020).

[15] How Particle Accelerators Work | Department of Energy. https://www.energy.gov/articles/how-particle-accelerators-work. (Accessed on 10/1/2020).

[16] LumiPublicResults < CMSPublic < TWiki. https://twiki.cern.ch/twiki/bin/view/CMSPublic/LumiPublicResults#Multi_year_plots. (Accessed on 10/1/2020).

[17] Project Schedule | HL-LHC Industry. https://project-hl-lhc-industry.web.cern.ch/content/project-schedule. (Accessed on 10/1/2020).

[18] Quantum diaries. https://www.quantumdiaries.org/tag/root/. (Accessed on 10/1/2020).

[19] Silicon strips | cms experiment. https://cms.cern/detector/identifying-tracks/silicon-strips. (Accessed on 10/1/2020).

[20] The Standard Model Infographic. https://cds.cern.ch/journal/CERNBulletin/2012/35/News%20Articles/1473657. (Accessed on 10/2/2020).

[21] Tracker detector | CMS Experiment. http://cms.web.cern.ch/news/tracker-detector. (Accessed on 10/1/2020).

[22] Ultimus™ V High Precision Dispenser: Precision Dispensing | Nordson EFD. https://www.nordson.com/en/divisions/efd/products/fluid-dispensing-systems/ultimus-v-high-precision-dispenser. (Accessed on 10/2/2020).

[23] What Is FEA | Finite Element Analysis? SimScale Documentation. https://www.simscale.com/docs/simwiki/fea-finite-element-analysis/what-is-fea-finite-element-analysis/. (Accessed on 10/2/2020).

[24] *ATLAS: technical proposal for a general-purpose pp experiment at the Large Hadron Collider at CERN*. LHC Tech. Proposal. CERN, Geneva, 1994.

[25] *Technical proposal*. LHC Tech. Proposal. CERN, Geneva, 1994. Cover title : CMS, the Compact Muon Solenoid : technical proposal.

[26] *ALICE: Technical proposal for a Large Ion collider Experiment at the CERN LHC*. LHC Tech. Proposal. CERN, Geneva, 1995.

[27] *The CMS hadron calorimeter project: Technical Design Report*. Technical Design Report CMS. CERN, Geneva, 1997. The following files are from *http* : *//uscms.fnal.gov/pub/hcal_tdr* and may not be the version as printed, please check the printed version to be sure.

[28] *LHCb : Technical Proposal*. Tech. Proposal. CERN, Geneva, 1998.

[29] Cryogenics: Low temperatures, high performance . Aug 2012.

[30] The Phase-2 Upgrade of the CMS Endcap Calorimeter. Technical Report CERN-LHCC-2017-023. CMS-TDR-019, CERN, Geneva, Nov 2017.

[31] G. Aad, T. Abajyan, B. Abbott, J. Abdallah, S. Abdel Khalek, A.A. Abdelalim, O. Abdinov, R. Aben, B. Abi, M. Abolins, and et al. Observation of a new particle in the search for the Standard Model Higgs boson with the ATLAS detector at the LHC. *Physics Letters B*, 716(1):1–29, Sep 2012.

[32] Kaustubh Agashe, Hooman Davoudiasl, Gilad Perez, and Amarjit Soni. Warped Gravitons at the LHC and Beyond. *Phys. Rev.*, D76:036006, 2007.

[33] Guido Altarelli, Barbara Melé, and M Ruiz-Altaba. Searching for new heavy vector bosons in p$\overline{p}$ colliders. *Z. Phys. C*, 45(CERN-TH-5323-89):109–121. 46 p, Mar 1989.

[34] J. Alwall, R. Frederix, S. Frixione, V. Hirschi, F. Maltoni, O. Mattelaer, H.-S. Shao, T. Stelzer, P. Torrielli, and M. Zaro. The automated computation of tree-level and next-to-leading order differential cross sections, and their matching to parton shower simulations. *Journal of High Energy Physics*, 2014(7), Jul 2014.

[35] Nima Arkani-Hamed, Andrew G Cohen, Emanuel Katz, and Ann E Nelson. The littlest higgs. *Journal of High Energy Physics*, 2002(07):034–034, Jul 2002.

[36] G L Bayatian et al. *CMS Physics: Technical Design Report Volume 1: Detector Performance and Software*. Technical Design Report CMS. CERN, Geneva, 2006. There is an error on cover due to a technical problem for some items.

[37] Brando Bellazzini, Csaba Csáki, and Javi Serra. Composite higgses. *The European Physical Journal C*, 74(5), May 2014.

[38] Michael Benedikt, Paul Collier, V Mertens, John Poole, and Karlheinz Schindl. *LHC Design Report*. CERN Yellow Reports: Monographs. CERN, Geneva, 2004.

[39] Daniele Bertolini, Philip Harris, Matthew Low, and Nhan Tran. Pileup per particle identification. *Journal of High Energy Physics*, 2014(10):1–22, 2014.

[40] Fady Bishara and Fady Adibsamy Bishara. Theory overview: Dark Matter. 8th Edition of the Large Hadron Collider Physics Conference. May 2020.

[41] Sara Bolognesi, Yanyan Gao, Andrei V. Gritsan, Kirill Melnikov, Markus Schulze, Nhan V. Tran, and Andrew Whitbeck. On the spin and parity of a single-produced resonance at the LHC. *Phys. Rev.*, D86:095031, 2012.

[42] BRIL Group. Bril work suite. http://cms-service-lumi.web.cern.ch/cms-service-lumi/brilwsdoc.html, 2017.

[43] Matteo Cacciari, Gavin P. Salam, and Gregory Soyez. The anti-k_T jet clustering algorithm. *JHEP*, 04:063, 2008.

[44] S. Chatrchyan et al. The CMS experiment at the CERN LHC. *JINST*, 3:S08004. 361 p, 2008.

[45] S. Chatrchyan et al. Performance of CMS muon reconstruction in pp collision events at $\sqrt{s} = 7$ TeV. *JINST*, 7(CMS-MUO-10-004. CMS-MUO-10-004. CERN-PH-EP-2012-173):P10002. 81 p, Jun 2012. Comments: Submitted to the Journal of Instrumentation.

[46] S. Chatrchyan, V. Khachatryan, A.M. Sirunyan, A. Tumasyan, W. Adam, E. Aguilo, T. Bergauer, M. Dragicevic, J. Erö, C. Fabjan, and et al. Observation of a new boson at a mass of 125 GeV with the CMS experiment at the LHC. *Physics Letters B*, 716(1):30–61, Sep 2012.

[47] CMS Collaboration. Particle–flow event reconstruction in CMS and performance for jets, taus, and E_T^{miss}. CMS Physics Analysis Summary CMS-PAS-PFT-09-001, CERN, 2009.

[48] CMS E/gamma POG. Cut based electron id for run 2 legacy. https://twiki.cern.ch/twiki/bin/view/CMS/CutBasedElectronIdentificationRun2, 2018.

[49] CMS JetMET POG. Met filter recommendations for run 2. 2016. https://twiki.cern.ch/twiki/bin/viewauth/CMS/MissingETOptionalFiltersRun2.

[50] CMS JetMET POG. Recommended jet energy corrections and uncertainties for data and mc. 2018. https://twiki.cern.ch/twiki/bin/view/CMS/JECDataMC#2017_Data.

[51] CMS JetMET POG. Jet energy resolution. https://twiki.cern.ch/twiki/bin/view/CMS/JetResolution, 2020.

[52] CMS JetMET POG. W/z-tagging of jets. https://twiki.cern.ch/twiki/bin/viewauth/CMS/JetWtagging#Systematic_uncertainties, 2020.

[53] CMS Muon POG. Reference muon id, isolation and trigger efficiencies for 2016 legacy re-reco data. https://twiki.cern.ch/twiki/bin/view/CMS/MuonReferenceEffs2016LegacyRereco, 2018.

[54] CMS Muon POG. Reference muon id, isolation and trigger efficiencies for 2017 data. https://twiki.cern.ch/twiki/bin/view/CMS/MuonReferenceEffs2017, 2018.

[55] Glen Cowan, Kyle Cranmer, Eilam Gross, and Ofer Vitells. Asymptotic formulae for likelihood-based tests of new physics. *Eur. Phys. J.*, C71:1554, 2011. [Erratum: Eur. Phys. J.C73,2501(2013)].

[56] F Englert and R Brout. Broken symmetry and the masses of gauge vector mesons. *Phys. Rev. Lett.*, 13:321–323, 1964.

[57] Lyndon R Evans and Philip Bryant. LHC Machine. *JINST*, 3:S08001. 164 p, 2008. This report is an abridged version of the LHC Design Report (CERN-2004-003).

[58] D Froidevaux and P Sphicas. General-purpose detectors for the Large Hadron Collider. *Annu. Rev. Nucl. Part. Sci.*, 56:375–440, 2006.

[59] Sheldon L. Glashow. Partial-symmetries of weak interactions. *Nuclear Physics*, 22(4):579 – 588, 1961.

[60] Walter D. Goldberger and Mark B. Wise. Modulus stabilization with bulk fields. *Physical Review Letters*, 83(24):4922–4925, Dec 1999.

[61] Davide Greco and Da Liu. Hunting composite vector resonances at the lhc: naturalness facing data. *Journal of High Energy Physics*, 2014(12), Dec 2014.

[62] David J Griffiths. *Introduction to Elementary Particles*. Wiley-VCH, 2008.

[63] Harel, A. and Schieferdecker, P. Jet identification. https://twiki.cern.ch/twiki/bin/view/CMS/JetID, 2018.

[64] Peter W. Higgs. Broken Symmetries and the Masses of Gauge Bosons. *Phys. Rev. Lett.*, 13:508–509, Oct 1964.

[65] V Karimäki et al. *The CMS tracker system project: Technical Design Report*. Technical Design Report CMS. CERN, Geneva, 1997.

[66] V. Khachatryan, A. M. Sirunyan, A. Tumasyan, W. Adam, T. Bergauer, M. Dragicevic, J. Erö, C. Fabjan, M. Friedl, and et al. Identification techniques for highly boosted w bosons that decay into hadrons. *Journal of High Energy Physics*, 2014(12), Dec 2014.

[67] Vardan Khachatryan et al. Performance of photon reconstruction and identification with the CMS detector in proton-proton collisions at $\sqrt{s} = 8$ TeV. *JINST*, 10:P08010, 2015.

[68] Vardan Khachatryan et al. The CMS trigger system. *JINST*, 12:P01020, 2017.

[69] Kamal Lamichhane. Search for 750 GeV Resonance in MonoZ channel at CMS Experiment. Master's thesis, Texas Tech University, Lubbock, TX, 2016.

[70] Andrew J. Larkoski, Simone Marzani, Gregory Soyez, and Jesse Thaler. Soft Drop. *JHEP*, 1405:146, 2014.

[71] J. M. Lindert, S. Pozzorini, R. Boughezal, J. M. Campbell, A. Denner, S. Dittmaier, A. Gehrmann-De Ridder, T. Gehrmann, N. Glover, A. Huss, and et al. Precise predictions for V + jets dark matter backgrounds. *The European Physical Journal C*, 77(12), Dec 2017.

[72] Mariangela Lisanti. Lectures on Dark Matter Physics, 2016.

[73] Chris Mann. The Bottle to Bang, 2008.

[74] Esma Mobs. The CERN accelerator complex - 2019. Complexe des accélérateurs du CERN - 2019. Jul 2019. General Photo.

[75] Alexandra Oliveira. Gravity particles from Warped Extra Dimensions, predictions for LHC. 2014.

[76] Duccio Pappadopulo, Andrea Thamm, Riccardo Torre, and Andrea Wulzer. Heavy vector triplets: bridging theory and data. *Journal of High Energy Physics*, 2014(9), Sep 2014.

[77] Particle Data Group, M. Tanabashi, et al. Review of particle physics. *Phys. Rev. D*, 98:030001, 2018.

[78] Antonio Pich. The standard model of electroweak interactions, 2007.

[79] Lisa Randall and Raman Sundrum. Large mass hierarchy from a small extra dimension. *Physical Review Letters*, 83(17):3370–3373, Oct 1999.

[80] Keith Rehermann and Brock Tweedie. Efficient identification of boosted semileptonic top quarks at the LHC. *JHEP*, 03:059, 2011.

[81] Rohan Bhandari, Adam Dishaw, Ryan Heller, Ana Ovcharova, Jeffrey Richman, Manuel Franco Sevilla, David Stuart, Chris West, Jae Hyeok Yoo. Search for supersymmetry in pp collisions at $\sqrt{s} = 13$ tev in the single-lepton final state using the sum of masses of large radius jets. *CMS Analysis Note*, AN-15-139, 2015.

[82] L Rossi. Superconducting Cable and Magnets for the Large Hadron Collider. (LHC-Project-Report-694. CERN-LHC-Project-Report-694):9 p, Mar 2004.

[83] A. Salam and J.C. Ward. Electromagnetic and weak interactions. *Physics Letters*, 13(2):168 – 171, 1964.

[84] Martin Schmaltz and David Tucker-Smith. Little higgs theories. *Annual Review of Nuclear and Particle Science*, 55(1):229–270, Dec 2005.

[85] A. M. Sirunyan et al. Particle-flow reconstruction and global event description with the CMS detector. *JINST*, 12:P10003, 2017.

[86] A. M. Sirunyan et al. Identification of heavy-flavour jets with the CMS detector in pp collisions at 13 TeV. *JINST*, 13:P05011, 2018.

[87] A M Sirunyan et al. Performance of the CMS muon detector and muon reconstruction with proton-proton collisions at $\sqrt{s} = 13$ TeV. *JINST*, 13:P06015, 2018.

[88] Albert M Sirunyan et al. Performance of missing transverse momentum reconstruction in proton-proton collisions at $\sqrt{s} = 13$ TeV using the CMS detector. *JINST*, 14(07):P07004, 2019.

[89] Torbjörn Sjöstrand, Stephen Mrenna, and Peter Skands. A brief introduction to pythia 8.1. *Computer Physics Communications*, 178(11):852–867, Jun 2008.

[90] Jesse Thaler and Ken Van Tilburg. Identifying Boosted Objects with N-subjettiness. *JHEP*, 03:015, 2011.

[91] The Monojet Group. Run 2 monojet / mono-V analysis. *CMS Analysis Note*, AN-20-042, 2020.

[92] Mark Thompson. *Modern Particle Physics*. Cambridge University Press, 2013.

[93] Verlaat and A. V. Lysebetten and M. V. Beuzekom. CO2 cooling for HEP experiments. 2008.

[94] Steven Weinberg. A Model of Leptons. *Phys. Rev. Lett.*, 19:1264–1266, Nov 1967.

[95] Steven Weinberg. *The Quantum Theory of Fields*. Cambridge University Press, 2010.